

LARGE EDDY SIMULATION OF WALL-BOUNDED TURBULENT FLOWS AT HIGH REYNOLDS NUMBERS

A Thesis Submitted to the
College of Graduate and Postdoctoral Studies
in Partial Fulfillment of the Requirements
for the Degree of Doctor of Philosophy
in the Department of Mechanical Engineering
University of Saskatchewan
Saskatoon

By

Hadi Hosseinzade Halquesari

Permission to Use

In presenting this dissertation in partial fulfillment of the requirements for a Postgraduate degree from the University of Saskatchewan, I agree that the Libraries of this University may make it freely available for inspection. I further agree that permission for copying of this dissertation in any manner, in whole or in part, for scholarly purposes may be granted by Professor Donald J. Bergstrom who supervised my dissertation work or, in his absence, by the Head of the Department or the Dean of the College in which my thesis work was done. It is understood that any copying or publication or use of this dissertation or parts thereof for financial gain shall not be allowed without my written permission. It is also understood that due recognition shall be given to me and to the University of Saskatchewan in any scholarly use which may be made of any material in my dissertation.

Requests for permission to copy or to make other uses of materials in this dissertation in whole or part should be addressed to:

Head of the Department of Mechanical Engineering
57 Campus Drive
University of Saskatchewan
Saskatoon, Saskatchewan S7N 5A9 Canada

OR

Dean
College of Graduate and Postdoctoral Studies
University of Saskatchewan
116 Thorvaldson Building, 110 Science Place
Saskatoon, Saskatchewan S7N 5C9 Canada

Abstract

In the simulation of turbulent flows, resolving flow motions near a solid surface requires a high resolution that is computationally expensive. The present research investigates reducing the computational cost of simulating wall-bounded flows through a technique, called wall-modeling, that introduces the effects of the near-wall flow dynamics as a wall shear stress to the outer layer. Turbulent wall-bounded flows were studied using large eddy simulation at moderate to high Reynolds numbers to evaluate the performance of the wall-modeling.

The results of wall-modeled turbulent channel flow at $Re_\tau = 2000$ were in good agreement with the experimental data. However, a log-layer mismatch was observed in the mean velocity profile below the matching point due to the inconsistency between the local grid resolution and that required by the subgrid scale model. Moving the matching point further from the wall mitigated the mismatch. The effects of time averaging and temporal filtering schemes on the performance of the wall model were also investigated. It was found that smaller time periods for time averaging result in a wall model that is more responsive to the flow structures in the outer layer. The results indicated that the temporal filtering scheme is strongly dependent on the location of the matching point.

Next, the wall-modeling was implemented in the simulation of a turbulent boundary layer. Inflow generation methods were reviewed, and a recycling rescaling method was employed to generate realistic turbulence at the inlet boundary. Zero pressure gradient turbulent boundary layers over a wide range of Reynolds numbers up to $Re_\theta = 25\,523$ were studied in terms of the mean velocity profile, Reynolds stress, and skin-friction coefficient. It was found that a wall-modeled turbulent boundary layer can be resolved using a much lower grid resolution in the wall layer.

Finally, the wall stress model was implemented to introduce the effects of wall roughness into the wall-modeling via the eddy viscosity. The proposed wall model was examined for transitionally and fully rough channel flows and successful results were achieved. For high-Reynolds number wall-bounded flows, wall-modeling can effectively couple a large eddy simulation to the wall via the wall shear stress without the need to fully resolve the inner region.

Acknowledgments

There were moments in my program that I was devastated by professional and personal difficulties. I won't forget my supervisor's support to go through those moments. I would love to express my sincere gratitude to Professor Donald J. Bergstrom for not only sharing his in-depth knowledge about fluid mechanics but also providing inspiration over the past years.

I would also thank my committee members: Professor David Sumner, Professor James D. Bugg, and Professor Alexey Shevyakov for their valuable advice and suggestions on my dissertation. I extend my thanks to all my friends and colleagues in the CFD Laboratory to make my PhD program enjoyable, and special thanks to Shawn Reinink for his technical and spiritual support. I also gratefully acknowledge funding supports as scholarships from the University of Saskatchewan and a research grant from the Natural Sciences and Engineering Research Council (NSERC) of Canada.

This work would also be incomplete without consistent and unconditional support from my family. Without their love, I would never have made it this far.

TO MY FAMILY:

Sirus

Lohri

Mahdi

Contents

Permission to Use	i
Abstract	ii
Acknowledgment	iii
List of Tables	viii
List of Figures	ix
Nomenclature	xiv
Abbreviations	xix
1 Introduction	1
1.1 Motivation	1
1.2 Large Eddy Simulation	3
1.3 High-Reynolds Number Wall-bounded Flows	4
1.4 Objectives and Scope	6
1.5 Expected Contributions	7
1.6 Outline of Dissertation	7
2 Background to Wall-modeling and Inflow Generation Methods	9
2.1 Wall-modeling	9
2.1.1 Hybrid RANS/LES Wall Model	11
2.1.2 Wall Stress Model	12
2.1.3 Wall Function Model	13
2.1.4 Dynamic Non-equilibrium Wall Model	14
2.1.5 Other Wall Models	17
2.2 Inflow Generation Methods	20
2.2.1 Transition-inducing Methods	21

2.2.2	Library-based Methods	22
2.2.3	Synthetic Methods	23
2.2.4	Recycling Methods	25
3	Numerical Methodology in Wall-modeled Large Eddy Simulation	30
3.1	Governing Equations	30
3.1.1	Pressure-correction Method	31
3.1.2	Numerical Solver and Convergence Criteria	32
3.2	Discretization of the First Cell in the LES Domain	34
3.3	Wall Layer Modeling	35
3.3.1	Discrete Form of the Thin Boundary Layer Equations	36
3.3.2	Dynamic Eddy Viscosity	38
3.3.3	Time Averaging and Temporal Filtering	39
4	Large Eddy Simulation of Channel Flows at Moderate and High Reynolds Numbers	41
4.1	Numerical Method	42
4.2	Wall-resolved LES Channel Flow at $Re_\tau = 395$	43
4.3	Wall-modeled LES Channel Flow at $Re_\tau = 395$	46
4.4	Effects of Reynolds Number in Wall-modeling	49
4.5	Time Averaging and Temporal Filtering in WMLES Turbulent Channel Flows	52
4.5.1	WMLES Channel Flow at $Re_\tau = 2000$	52
4.5.2	Eddy Viscosity in the Wall Layer	55
4.5.3	Temporal Filtering and Time Averaging Schemes	57
4.5.4	Wall Layer Response to Input Velocity	61
4.5.5	Grid Distribution and Matching Point	64
4.6	Conclusions	66
5	Numerical Approach to Inflow Generation for Turbulent Boundary Layers	68
5.1	LWS Method	68
5.1.1	Rescaling the Mean Velocity	69
5.1.2	Rescaling the Fluctuating Velocity	70
5.1.3	Inflow Velocity Component	71
5.2	Heaviside Function	72
5.3	Boundary Conditions	73
5.3.1	Top Boundary Treatment	74
5.3.2	Adjustment of Outflow	76
5.4	Summary	76

6	Large Eddy Simulation of Zero Pressure Gradient Turbulent Boundary Layers	78
6.1	Computational Set-up	79
6.2	Wall-resolved Boundary Layer at $Re_\theta = 2710$	81
6.3	Sensitivity to Grid Resolution	86
6.4	Wall-modeled LES of Turbulent Boundary Layers at $Re_\theta = 2037 - 25\,523$. .	87
6.5	Study of a High-Reynolds Number Wall-modeled Turbulent Boundary Layer at $Re_\theta = 24\,500$	91
6.6	Conclusions	96
7	Wall Stress Model with the Effects of Surface Roughness	98
7.1	Introduction to Roughness	98
7.2	Background to Wall Roughness Modeling	100
7.2.1	Equivalent Sand Grain Roughness	100
7.2.2	Discrete Element Method	103
7.3	Roughness in Wall-modeling	105
7.3.1	Virtual Wall Model	106
7.3.2	Immersed Boundary Method	107
7.3.3	Other Models	107
7.4	Methodology for Introducing Surface Roughness to Dynamic Non-equilibrium Wall Stress Model	108
7.5	Numerical Method	111
7.6	Wall-modeled Turbulent Flow in a Symmetric Rough Channel	112
7.7	Wall-modeled Turbulent Flow in Asymmetric Rough Channel	115
7.8	Conclusions	119
8	Conclusions, Contributions, and Recommendations	121
8.1	Conclusions	121
8.2	Major Contributions	122
8.3	Future Work	124
	Appendix	126
A	Subgrid Scale Models	126
A.1	Smagorinsky Model	126
A.2	Dynamic Smagorinsky Model	127
A.3	Dynamic Nonlinear Subgrid Scale Model	128

List of Tables

2.1	Different zero-equation eddy viscosity models.	16
4.1	Grid and temporal resolution of turbulent channel flows at different Reynolds numbers.	43
4.2	The standard deviation between the mean velocities obtained from the WM-LES channel flow and the DNS results presented in Fig. 4.9; all values are in percent.	50
5.1	Top boundary conditions in turbulent boundary layers.	75
6.1	Computational specifications for flat plate turbulent boundary layer simulations.	80
7.1	Specifications of wall-modeled turbulent channel flows with rough walls at different Reynolds numbers.	112
7.2	Summary results for symmetric and asymmetric rough channel flows using the wall-modeling.	116

List of Figures

2.1	Categories of wall models for high-Reynolds number turbulent flows.	11
2.2	Transferring data at the matching point between the wall layer and LES. . .	12
2.3	Categories of inflow generation methods.	22
2.4	Library-based inflow generation method using an auxiliary simulation in a turbulent boundary layer.	24
2.5	A schematic of recycling rescaling inflow generation.	26
3.1	A sketch of the control volume used in the pressure-correction method. . . .	31
3.2	First cell off the wall in LES.	34
3.3	A schematic of a three-dimensional embedded mesh in the first cell of the LES domain.	35
3.4	A schematic of the control volume used in the wall-modeling.	37
4.1	A schematic of flow domain used in the simulation of turbulent channel flows.	42
4.2	(a) The mean velocity profile and (b) <i>rms</i> of velocity fluctuations (bottom to top: $v'^+_{\text{rms}}, w'^+_{\text{rms}}, u'^+_{\text{rms}}$) in a wall-resolved channel flow at $\text{Re}_\tau = 395$ using the DSM and DNM.	44
4.3	The rate of dissipation of turbulence kinetic energy ε in a vertical plane per- pendicular to the flow stream, the DSM at the top and the DNM on the bottom.	45
4.4	Profile of the resolved and SGS dissipation in the wall-resolved channel flow.	45
4.5	Interaction between the wall layer and LES domain in a side view of the channel flow; (a) the extent of the wall layer on the vertical symmetry plane showing streamwise velocity contours, and (b) a schematic of wall-modeling grid embedded in the LES domain.	46
4.6	Mean velocity profiles in the WMLES channel flow at $\text{Re}_\tau = 395$ in different coordinates.	47
4.7	Velocity fluctuations and Reynolds shear stress for the WMLES channel flow at $\text{Re}_\tau = 395$: (a) <i>rms</i> of velocity fluctuations, bottom to top: $v'^+_{\text{rms}}, w'^+_{\text{rms}}, u'^+_{\text{rms}}$, symbols; WMLES, solid line; WRLES (b) shear stress.	48

4.8	The mean velocity profiles for a wall-modeled channel flow at $Re_\tau = 395$ using different locations for the matching point.	49
4.9	The prediction of the mean velocity profile at $Re_\tau = 395, 550, 950$, and 2000 in a WMLES channel flow.	50
4.10	Velocity fluctuations at $Re_\tau = 550$ and 950 in the WMLES channel flows; from bottom to top: $v'^+_{rms}, w'^+_{rms}, u'^+_{rms}$	51
4.11	Mean velocity profiles at $Re_\tau = 2000$ with $T_W = 1.0, T_F = 1.0$	53
4.12	Velocity fluctuations and Reynolds shear stress profiles at $Re_\tau = 2000$ with $T_W = 1.0, T_F = 1.0$ (w'^+_{rms} and u'^+_{rms} profiles are shifted by $+0.5$ and $+1.0$, respectively)	54
4.13	Resolved velocity fluctuations and Reynolds shear stress across the wall layer.	55
4.14	Eddy viscosity across the wall layer.	56
4.15	Temporal filtering versus no-filtering with $T_W = 1.0$ and $T_F = 1.0$	57
4.16	The effects of various filtering and averaging time periods: (a) Scenario A with the matching point at the first node, and (b) Scenario B with the matching point at the fifth node.	58
4.17	Tracking the streamwise velocity at the matching point (5^{th} node) for the instantaneous and temporal-filtered LES and time-averaged wall layer with the dimensionless filtering time period $T_F = 1.0$	60
4.18	Tracking the streamwise velocity similar to Fig. 4.17 with $T_F = 0.1$	61
4.19	Response of wall-modeling to LES field for dimensionless averaging time periods of (a) $T_W = 1.0$, and (b) $T_W = 0.1$	62
4.20	Wall shear stress fluctuations for various T_F and T_W values for the WMLES channel flow at $Re_\tau = 2000$	63
4.21	Comparison of wall shear stress fluctuations of WMLES (at $Re_\tau = 2000$ and $Re_\tau = 395$ with $T_F = 1.0$ and $T_W = 0.1$) with WRLES at $Re_\tau = 395$ with/without temporal filtering with $T_F = 1.0$	64
4.22	Comparison of four scenarios with $T_F = 1.0$ and $T_W = 0.1$ using the temporal filtering (TF) and non-temporal filtering (NTF) schemes. The profiles in the lower region pertain to Scenario A and D, where the matching point is located at the first node. The upper region presents the results for Scenario B and C with the matching point located at the 5^{th} and 3^{rd} nodes, respectively.	65
5.1	Weighting function across the boundary layer.	71
5.2	Heaviside function.	73
5.3	Boundary conditions in the turbulent boundary layer.	74
5.4	Schematic of control volumes at the exit plane.	77

6.1	Time series of streamwise velocity in the wall layer at $y/\delta = 0.035$ ($y^+ \approx 31$) and in the freestream region at $y/\delta = 2.0$	81
6.2	Mean velocity profiles for the wall-resolved boundary layer at $Re_\theta = 2710$ in (a) inner coordinates, and (b) defect formulation (WRLES: solid line, $(U_\infty - U)/u_\tau$; WRLES: dashed line, $(U_\infty - U)\delta/U_\infty\delta^*$; Degraaff and Eaton (2000): \triangle , $(U_\infty - U)/u_\tau$; Degraaff and Eaton (2000): \bullet , $(U_\infty - U)\delta/U_\infty\delta^*$).	82
6.3	Velocity fluctuations and Reynolds shear stress in the wall-resolved TBL at $Re_\theta = 2710$; symbols: experiment by Degraaff and Eaton (2000) at $Re_\theta = 2900$	83
6.4	Characteristics of the mean velocity for the wall-resolved boundary layer at moderate Reynolds numbers.	84
6.5	Variation of the power-law exponent λ (solid line) in comparison with the empirical value (-0.125, dashed line) in a spatially developing ZPGTBL.	85
6.6	Instantaneous velocity contours on a control vertical plane in a WRLES boundary layer using a coarse grid with (a) streamwise unphysical oscillations, (b) oscillations at the outflow region, and (c) time variation of streamwise velocity near the edge of the boundary layer.	86
6.7	Mean velocity profiles of TBLs using inner coordinates, WMLES: solid lines, at $Re_\theta = 2620, 8400, 13\,100$, and $24\,500$ from bottom to top; experiments: symbols; log law [$\kappa = 0.39$ and $B = 5.0$ for the two bottom profiles and $\kappa = 0.384$ and $B = 4.17$ for the two top profiles (Nagib and Chauhan, 2008)]: dashed line. Dotted lines show the location of the corresponding matching point. The profiles are shifted with increments of five units for clarity.	88
6.8	Mean velocity profiles in deficit coordinates for wall-modeled turbulent boundary layers. experiments: symbols (Degraaff and Eaton, 2000).	89
6.9	The skin-friction coefficient as a function of Reynolds number based on momentum thickness for high-Reynolds number turbulent boundary layers using wall-modeling.	90
6.10	Mean velocity profiles in (a) inner coordinates and (b) outer coordinates for WMLES at $Re_\theta = 24\,500$, black solid line; log law ($\kappa = 0.384, B = 4.17$), dashed line; Park and Moin (2014) at $Re_\theta = 31\,000$, blue solid line; Kawai and Larsson (2013) at $Re_\theta = 50\,000$, red solid line; Degraaff and Eaton (2000) at $Re_\theta = 31\,000$, \circ ; Vallikivi et al. (2015) at $Re_\theta = 26\,900$, \square ; Souverein et al. (2010) at $Re_\theta = 50\,000$, \triangle	92

6.11	Velocity fluctuations and Reynolds shear stress in the wall-modeled TBL at $Re_\theta = 24\,500$: (a) streamwise velocity fluctuation in outer coordinates, (b) streamwise velocity fluctuation in inner coordinates, (c) wall-normal velocity fluctuation, and (d) Reynolds shear stress across the boundary layer. For details of experimental data (symbols) refer to Fig. 6.10.	93
6.12	Total shear stress: solid line (experiment: \bullet), Reynolds shear stress: dashed line (experiment: \circ), and viscous shear stress: dotted-dashed line (experiment: \square) across the boundary layer compared to the experimental data of Degraaff and Eaton (2000).	94
6.13	Turbulence kinetic energy production in the WMLES TBL at $Re_\theta = 24\,500$	95
6.14	Flow characteristics across the wall layer in the WMLES TBL at $Re_\theta = 24\,500$	96
7.1	Modified damping functions in Eqs. 7.5 and 7.26 for wall roughness with $R^+ = 70$	109
7.2	Schematic of total shear stress in wall-bounded turbulent flows used to estimate the wall shear stress by a linear extrapolation.	111
7.3	Mean velocity profile of the wall-modeled channel flow with roughness on both walls at $Re_{\tau_r} = 615$ with $k_s^+ = 62$; smooth WMLES at $Re_{\tau_r} = 655$, dashed line; Krogstad et al. (2005) at $Re_{\tau_r} = 600$ with $k_s^+ = 63$, \square ; Krogstad et al. (2005) at $Re_{\tau_s} = 670$, \triangle ; log law for the smooth test case, $\kappa = 0.4$ and $B = 5.0$; the location of the matching point is shown with a dotted line.	113
7.4	Velocity fluctuations and Reynolds shear stress in a channel flow at $Re_{\tau_r} = 615$ with $k_s^+ = 62$. Symbols: experiments by Krogstad et al. (2005), solid lines: WMLES. The profiles of w'^+_{rms} and u'^+_{rms} are shifted up by 0.5 and 1.0 for clarity, respectively.	114
7.5	Mean velocity profile of the rough channel flow at $Re_{\tau_r} = 2080$ with $k_s^+ = 62$; smooth WMLES at $Re_{\tau_s} = 1970$, dashed line; Suga et al. (2006) at $Re_{\tau_r} = 2580$ with $k_s^+ = 63$, \circ ; Hoyas and Jiménez (2006) at $Re_{\tau_s} = 2000$ with smooth walls, thin solid line; matching point, dotted line.	114
7.6	Mean velocity profile of asymmetric channel flows for (a) case C1 at $Re_{\tau_r} = 640$ with $k_s^+ = 62$, and (b) case D1 at $Re_{\tau_r} = 1160$ with $k_s^+ = 112$; the location of the matching point is shown with a dotted line.	116
7.7	Distribution of mean velocity profile in asymmetric rough channel at $Re_{\tau_r} = 640$ with $k_s^+ = 62$ for case C1 and $Re_{\tau_r} = 1160$ with $k_s^+ = 112$ for case D1. The profiles for case D1 are shifted a half unit upwards. The location of the matching point is shown with a dotted line.	117

7.8	Velocity fluctuations and Reynolds shear stress in channel flows for (a) case C1 at $Re_{\tau_r} = 640$ with $k_s^+ = 62$ and (b) case D1 at $Re_{\tau_r} = 1160$ with $k_s^+ = 112$. Symbols: experiments by Burattini et al. (2008), solid lines: WMLES. The profiles of w_{rms}^+ and u_{rms}^+ are shifted upward by 0.5 and 1.0, respectively. . .	118
7.9	The rate of production \mathcal{P} normalized by $\delta/u_{\tau_r}^3$ for (a) case C1 at $Re_{\tau_r} = 640$ with $k_s^+ = 62$, and (b) case D1 at $Re_{\tau_r} = 1160$ with $k_s^+ = 112$	118
7.10	Turbulence kinetic energy in asymmetric rough channel flows for test cases C1 and D1.	119

Nomenclature

English

a_i	Coefficient in discretized equations in the i -direction
a_{Lx}, a_{Lz}	Roughness area density in the streamwise and spanwise directions, respectively
A_i	Face area
A_P	Projected area of a single roughness element
A_y	Wall-parallel surface area
A^+	Constant parameter in the damping function (Eq. 2.9)
b, b_o	Source term in discretized equations
b_p	Source term in wall-modeling (Eq. 3.20)
B	Constant parameter in the log law correlation
C_D	Drag coefficient
C_f	Skin-friction coefficient
C_S	Smagorinsky coefficient
$C\Delta_w$	Slip length (Eq. 2.16)
d	Resolvable height of roughness (Eq. 7.18)
dt	Computational time step
\mathcal{D}	Van Driest damping function
$f_1, f_2, f_3, f_4, f_5, f_6$	Universal functions
\mathcal{F}	Modified damping function for rough surfaces
$G(x, r)$	Filtering function
h_i	Height of a particular roughness element
h_{wm}	Height of wall layer, $h_{wm}^+ = h_{wm}u_\tau/\nu$
H	Shape factor/Heaviside function
k	Turbulence kinetic energy
k_s^+	Equivalent roughness height, $k_s^+ = k_s u_\tau/\nu$
\mathcal{K}	Geometrical function of y (Eq. 2.10)

l_i	Slip length
ℓ_m	Mixing length scale
l_o	Length scale of the energetic eddy
l_p	Length scale regularization parameter
l_s	Smagorinsky length scale
L	The maximum height of the roughness
L_x, L_y, L_z	Length of computational domain in the streamwise, wall-normal, and spanwise directions, respectively
\dot{m}	Mass flux
n_x, n_y, n_z	Number of grid points in the streamwise, wall-normal, and spanwise directions, respectively
N_m	Location of matching point
p	Pressure of fluid
P	Mean pressure
p'	Pressure correction
\mathcal{P}	Turbulence kinetic energy production, $-\langle u'v' \rangle dU/dy$
\mathcal{P}^+	Normalized turbulence kinetic energy production, $\mathcal{P}^+ = \mathcal{P}\nu/u_\tau^4$
r	Residual in pressure-correction
R	Sum of residuals in pressure-correction
R_{ij}	Reynolds stresses
Re	Reynolds number
Re_x	Reynolds number based on the distance from the leading edge, $Re_x = U_\infty x/\nu$
Re_δ	Reynolds number based on the boundary layer thickness, $Re_\delta = U_\infty \delta/\nu$
Re_{δ^*}	Reynolds number based on the displacement thickness, $Re_{\delta^*} = U_\infty \delta^*/\nu$
Re_θ	Reynolds number based on the momentum thickness, $Re_\theta = U_\infty \theta/\nu$
Re_τ	Reynolds number based on the friction velocity, $Re_\tau = u_\tau \delta/\nu$
Re_{τ_r}	Reynolds number based on the friction velocity over a rough wall, $Re_{\tau_r} = u_{\tau_r} \delta/\nu$
Re_{τ_s}	Reynolds number based on the friction velocity over a smooth wall, $Re_{\tau_s} = u_{\tau_s} \delta/\nu$
R^+	Constant parameter in Eq. 7.7
$ S $	Characteristic rate of strain
S_{ij}	Strain rate tensor
t	Simulation time advancement
t_v	Viscous time scale, ν/u_τ^2

T	Dimensionless simulation time advancement normalized by convective time scale, $T = t/t_v$
T_{av}	Characteristic averaging time scale
T_{F}	Non-dimensional temporal filtering period, $T_{\text{F}} = T_{\text{fl}}/(h_{\text{wm}}/\kappa u_{\tau})$
T_{fl}	Characteristic filtering time scale
T_{ij}^*	Residual stress tensor at the test-grid level
T_{W}	Non-dimensional time averaging period, $T_{\text{W}} = T_{\text{av}}/(\delta/u_c)$
u, v, w	Velocity component in the streamwise, wall-normal, and spanwise directions, respectively
$u(x, t)$	Instantaneous velocity
$u'(x, t)$	Velocity fluctuation/subgrid scale velocity
u_1	Streamwise velocity
u_2	Wall-normal velocity
u_c	Mean velocity at the center of a channel
u_e	Face velocity at the east
u_n	Wall-normal velocity
u_{η}	Kolmogorov's velocity scale
u_{τ}, u_{τ_s}	Friction velocity over smooth surfaces
u_{τ_r}	Friction velocity over rough surfaces
$\overline{u'v'}^+$	Non-dimensional Reynolds shear stress
u^+	Non-dimensional streamwise velocity component, u/u_{τ}
\tilde{u}_i^*	Intermediate velocity in the fractional step method
$u_{\text{rms}}^+, v_{\text{rms}}^+, w_{\text{rms}}^+$	Non-dimensional root mean square of velocity fluctuations in the streamwise, wall-normal, and spanwise directions, respectively
U_c	Convective velocity at the outflow boundary
\overline{U}_f	Face streamwise velocity in Eq. 3.17
U_i	Mean velocity spatially averaged over the z -direction
U_{∞}	Freestream velocity
v_i	Slip velocity
\overline{V}_f	Face wall-normal velocity in Eq. 3.17
W	Weighting function
x, y, z	Cartesian coordinate
y_m	Height of the first node
y_u	Location of the maximum streamwise velocity in the asymmetric rough channel flows
y^+	Dimensionless wall-normal distance in wall coordinates, yu_{τ}/ν

y_1^+ Height of the first node near the wall in wall coordinates

Greek

α_i	Roughness factor, Eq. 7.14
γ	Scaling factor, Eq. 5.5
δ	Half of the channel height/boundary layer thickness
δ_{ij}	Kronecker delta
δ_v	Viscous length scale, $\delta_v = \nu/u_\tau$
δ^*	Displacement thickness
δt	Time step of simulation, $\delta t^+ = \delta t/t_v$
$\delta x, \delta y$	Grid spacing in wall-modeling in the streamwise and wall-normal directions, respectively
δx_e	Grid spacing at the east face in wall-modeling
Δ	Filter width
ΔU^+	Dimensionless mean velocity shift over rough surfaces, $\Delta U^+ = \Delta U/u_\tau$
Δt	Computational time step
$\Delta x, \Delta y, \Delta z$	Grid spacing in the streamwise, wall-normal, and spanwise directions, respectively
Δx_e	Grid spacing at the east face
Δx_i^+	Non-dimensional grid spacing, $\Delta x_i u_\tau/\nu$
Δy_c^+	Non-dimensional grid spacing in the wall-normal direction at the center of the channel
Δy_{\max}^+	Non-dimensional grid spacing in the wall-normal direction at the top of the turbulent boundary layer's computational domain
ϵ	Parameter used in Eq. 5.18
ε	Viscous dissipation
ε_r	Resolved dissipation
ε_{SGS}	Subgrid scale dissipation
ζ	Outer coordinate in boundary layers
η	Kolmogorov's length scale
θ	Momentum thickness
κ	Von Karman constant
κ_{wm}	Modified von Karman constant in wall-modeling (Eq. 3.26)
λ	Power-law exponent in Eq. 6.1

μ	Dynamic molecular viscosity
ν	Kinematic molecular viscosity
ν_n, ν_s	Molecular viscosity at the north and south faces, respectively
ν_{SGS}	Subgrid scale viscosity
ν_t	Eddy viscosity
$\nu_{t,\text{wm}}$	Modified eddy viscosity for rough surfaces
$\nu_{t,\text{wm}}^+$	Normalized modified eddy viscosity in the wall layer
ρ	Density of fluid
τ, τ_{tot}	Total shear stress
τ_{ij}^r	Anisotropic residual stress tensor
τ_{ij}^*	Residual stress tensor
τ_w	Wall shear stress, $\tau_w = \mu \frac{du}{dy}$
$\tau_{w,xy}$	Wall shear stress in the streamwise direction
$\tau_{w,zy}$	Wall shear stress in the spanwise direction
τ_η	Kolmogorov's time scale
ϕ	Variable parameter
Ω_{ij}	Rotation rate tensor

Superscripts

$\tilde{\phi}$	Filtered parameter
$\tilde{\tilde{\phi}}$	Filtered parameter at the test-grid level
$\langle \phi \rangle$	Time-averaged parameter
$\overline{\phi}$	Time-averaged parameter over a specific time period
$\hat{\phi}$	Temporal-filtered parameter

Abbreviations

ADI	Alternating Direction Implicit
APG	Adverse Pressure Gradient
CFD	Computational Fluid Dynamics
CFL	Courant-Friedrichs-Lewy
DES	Detached Eddy Simulation
DNM	Dynamic Nonlinear Model
DNS	Direct Numerical Simulation
DSM	Dynamic Smagorinsky Model
IBM	Immersed Boundary Method
LES	Large Eddy Simulation
LRN	Low Reynolds Number
LSE	Linear Stochastic Estimation
LWS	Lund-Wu-Squires
NSE	Navier-Stokes Equation
NTF	Non-temporal-filtered
NZPGTBL	Non-zero Pressure Gradient Turbulent Boundary Layer
ODE	Ordinary Differential Equation
PDE	Partial Differential Equation
POD	Proper Orthogonal Decomposition
rms	Root Mean Square
RANS	Reynolds-Averaged Navier-Stokes
SAS	Scale Adaptive Simulation
SGS	Subgrid Scale
TBL	Turbulent Boundary Layer
TBLE	Thin Boundary Layer Equation
TDMA	Tri-diagonal Matrix Algorithm
TF	Temporal-filtered
TNTI	Turbulent/Non-Turbulent Interface

URANS	Unsteady Reynolds-Averaged Navier-Stokes
VANS	Volume-Averaged Navier-Stokes
VLES	Very Large Eddy Simulation
WMLES	Wall-modeled Large Eddy Simulation
WRLES	Wall-resolved Large Eddy Simulation
ZPG	Zero Pressure Gradient
ZPGTBL	Zero Pressure Gradient Turbulent Boundary Layer

Chapter 1

Introduction

1.1 Motivation

Turbulence is the most significant and complicated phenomenon in the physics of fluids. Turbulence is observed in most natural flows and engineering applications such as the flow of water in rivers or the boundary layer growing on the wing of an aircraft. However, it is still difficult to precisely define turbulence, and instead it is described based on its characteristics. Turbulence is random and the flow field in turbulent flows varies significantly and irregularly in both time and space. Turbulence is three-dimensional and rotational, and it contains numerous vortical structures that appear at different length scales. Turbulent flows are also diffusive, and the rapid transport of momentum between different length scales is a feature of turbulence. Reynolds (1883) injected dye in a long pipe to demonstrate this feature. Dissipation is another characteristic of turbulent flows. Turbulence needs a continuous supply of energy since some kinetic energy is transformed into internal energy by velocity fluctuations working against viscous shear stresses. These characteristics make turbulent flow a cutting-edge research topic for engineers and mathematicians in fluids science.

The fast and reliable simulation of turbulent flow is essential in a spectrum of engineering applications ranging from aviation to power generation in wind farms. To achieve a solution for turbulent flows, the governing equations should first be specified. The well-known Navier-Stokes equations (NSE) mathematically govern a turbulent flow and represents conservation of momentum. Neglecting the body forces, the NSEs for incompressible flows are presented

as follows:

$$\frac{\partial u}{\partial t} + u \cdot \nabla u = \frac{\nabla p}{\rho} + \nu \nabla^2 u, \quad (1.1)$$

where u is the fluid velocity vector, t presents time coordinates, p is the fluid pressure, ρ is the density of fluid, ν is the kinematic viscosity, and ∇ is the gradient differential operator. However, the presence of a nonlinear convective term makes the solution of the NSE challenging even with the aid of powerful computers and advanced numerical schemes. Analytical solutions have been developed for the Navier-Stokes equations where the nonlinear terms can be neglected. For the general case, numerical solutions can be implemented for different flow problems. However, the computational cost associated with the numerical solution can be a significant challenge.

Various approaches have been developed to predict the behavior of turbulent flow in the context of computational fluid dynamics (CFD). Direct numerical simulation (DNS) is the simplest approach, which resolves all turbulent scales down to the Kolmogorov length scale where the kinetic energy is dissipated into heat by viscous forces. For a sufficiently fine grid, DNS needs no modeling, and hence is the most accurate approach. However, the computational cost of DNS can be prohibitive. An alternative approach is based on the time-averaged flow statistics. The mean values of the velocity and pressure fields provide adequate information for the majority of engineering applications. The governing Reynolds-Averaged Navier-Stokes (RANS) equations allow a lower grid and temporal resolution in solving the flow. RANS is much faster than DNS, but turbulence modeling becomes the challenge since there is no universal turbulence model. A third option is large eddy simulation (LES), where the large-scale motions are filtered and resolved, and the smaller subgrid scales are modeled. LES provides an unsteady solution similar to DNS, but it comes with lower computational costs. This feature makes LES a powerful tool for predicting instantaneous flow fields in research applications.

In many engineering and academic flow problems, there is an interaction between the flow and a wall or solid surface, which results in the formation of a boundary layer. The presence of solid walls introduces constraints that are absent in free shear layers. The viscosity of the fluid imposes a no-slip condition at a wall. The viscous constraint at the wall is associated with a viscosity-dominated length scale that is much smaller than the boundary layer thickness. The viscous length scale governs the dynamics of the flow in a narrow region near the wall. The grid resolution required to capture the small flow structures in the wall region reduces to the viscous length scale and becomes comparable to the grid resolution of a DNS. Hence, LES becomes much costlier in flows with a wall region. This dissertation focuses on effective

strategies for LES to simulate wall-bounded flows at high Reynolds numbers and consider the effects of near-wall flow dynamics without fully resolving them. This research is carried out at a fundamental level in terms of physics. However, the outcomes represent a significant contribution to the simulation of high-Reynolds number wall-bounded flows.

1.2 Large Eddy Simulation

Large eddy simulation was originated by Smagorinsky (1963) when he proposed a new approach for meteorological and atmospheric boundary layer applications. He suggested that there is no need to resolve all length scales down to the Kolmogorov length scale. The larger scales of motion contain most of the energy and anisotropy; however, most of the computational effort in DNS is dedicated to the small and dissipative motions (Pope, 2000). Hence, LES explicitly resolves the dynamics of large-scale unsteady turbulent motions and models the effects of smaller scales. This feature makes LES more computationally efficient than DNS and a more accurate method than Reynolds-averaged approaches, especially when unsteady flow structures are present.

The velocity $u(x, t)$ in LES is decomposed into a filtered component $\tilde{u}(x, t)$ and a subgrid scale (SGS) term $u'(x, t)$ through a predefined filtering operation, where x represents the location in the flow. The filtered velocity field is solved using the filtered NSE to resolve the large-scale eddies, and the SGS motions are introduced to the governing equations via a residual stress tensor. Using a low-pass filtering operation, a relatively coarse grid suffices to resolve the filtered velocity field $\tilde{u}(x, t)$. The filtering operation is expressed by

$$\tilde{u}(x, t) = \int G(r, x) u(x - r, t) dr, \quad (1.2)$$

where $G(x, r)$ is the filtering function, and r defines the coordinate in which the velocity field is filtered (Leonard, 1975). The most commonly used filter in LES is a Gaussian function. After applying the filtering operation to the velocity field, the velocity decomposition is defined as follows:

$$u(x, t) = \tilde{u}(x, t) + u'(x, t), \quad (1.3)$$

where $u'(x, t)$ is the residual velocity. The decomposition in Eq. 1.3 is analogous to the Reynolds decomposition but $\tilde{u}(x, t)$ is a random field, and the mean of the residual component is not zero:

$$\overline{u'}(x, t) \neq 0. \quad (1.4)$$

Applying the spatial-filtering operation to continuity and the NSE results in the following governing equations:

$$\tilde{u}_{i,i} = 0 \quad (1.5)$$

$$\dot{\tilde{u}}_i + (\widetilde{u_i u_j})_{,j} = -\frac{p_{,i}}{\rho} + \nu \tilde{u}_{i,jj} - \tau_{ij,j}^*, \quad (1.6)$$

where τ_{ij}^* is the SGS stress tensor. The LES approach is described in Appendix A in more detail.

1.3 High-Reynolds Number Wall-bounded Flows

Turbulence is composed of eddies of different sizes with specific velocity and length scales. The largest eddies are generated by instabilities at higher Reynolds numbers. They undergo a breakup process and transfer their kinetic energy to smaller eddies through a cascade of energy from large to small scales. This process continues until the Reynolds number is sufficiently small that molecular viscosity is able to dissipate the transferred energy as heat. The size of the important motions to be resolved by LES depends on the Reynolds number and boundary conditions. According to Kolmogorov's similarity hypothesis, the molecular viscosity ν and dissipation rate ε determine a universal length scale, which governs the statistics of small-scale motions at sufficiently high Reynolds numbers (Pope, 2000). Given ν and ε , the Kolmogorov length scale, velocity scale, and time scale are defined as follows:

$$\begin{aligned} \eta &\equiv (\nu^3/\varepsilon)^{1/4}, \\ u_\eta &\equiv (\nu\varepsilon)^{1/4}, \text{ and} \\ \tau_\eta &\equiv (\nu/\varepsilon)^{1/2}. \end{aligned} \quad (1.7)$$

Using the scaling $\varepsilon \sim u_0^3/l_0$, where u_0 and l_0 are the velocity and size of the energetic eddies, and the definition of the Kolmogorov length scale, the ratio of the smallest to the energetic length scale as a function of Reynolds number is given by

$$\eta/l_0 \sim \text{Re}_x^{-3/4}, \quad (1.8)$$

where $\text{Re}_x = U_\infty x/\nu$. The parameter x is the distance from the leading edge, and U_∞ shows the freestream velocity. It is evident that for increasing Reynolds number, the ratio η/l_0 decreases, which leads to a wider range of eddies to be resolved. This implies that for turbulent flow a higher grid resolution is required when the Reynolds number increases.

In addition to the general effect of Reynolds number just discussed, the energy-containing eddies decrease in size and become comparable to the viscous length scale δ_v near the wall. The grid resolution used in LES is too coarse to capture small-scale motions in the near-wall region. Chapman (1979) demonstrated that the number of grid points to resolve a wall-bounded flow depends on the Reynolds number ($N_{\text{total}} \propto \text{Re}_x^{2.4}$). At higher Reynolds numbers, this requires unaffordable resolution and is comparable to that of DNS, which leads to the alternative strategy of wall modeling. Wall modeling allows the use of a coarse grid near the wall, where there are important small-scale flow dynamics. The effects of these small-scale flow motions must be expressed in an averaged framework (Piomelli and Balaras, 2002). Since the flow motions in the wall layer experience several life cycles during a single time step in the outer layer, the instantaneous governing equations are unable to resolve them.

Depending on whether an equilibrium (where the advection and pressure gradient effects can be neglected) or non-equilibrium flow is assumed in the near-wall region, a simple algebraic function or a simplified form of the RANS equations is implemented to model the wall layer (Larsson et al., 2016). The wall model transmits the correct wall shear stress to the outer layer. Chapman (1979) estimated that the number of grid points required to resolve a wall-modeled flow is significantly reduced ($N_{\text{total}} \propto \text{Re}_x^{0.4}$). Although wall models mitigate the computational costs, they often result in poor prediction of the skin friction (Lee et al., 2013; Yang et al., 2017). One challenge for the wall modeling is to couple the LES and RANS regions, where an instantaneous field (LES) feeds the wall layer (RANS) at the top boundary. The wall layer experiences high-frequency fluctuations at the top, whereas it varies smoothly in time. This is manifest as a mismatch of mean velocity profiles in the overlap region. So-called dynamic wall models have been developed to accommodate the unsteadiness at the top boundary and alleviate the mismatch.

In the simulation of a turbulent boundary layer (TBL), starting from the leading edge is impractical due to its high computational cost. A short section in the turbulent region can be selected to study a TBL. However, defining realistic turbulence at the inlet represents an additional challenge in terms of boundary conditions. A turbulent channel flow employs periodic boundary conditions to introduce the flow information at the inlet, which allows a shorter flow domain. Using periodic boundary conditions for a boundary layer is problematic due to the spatial development. A rescaling method is an alternative strategy that allows the simulation of a high-Reynolds number TBL on a compact flow domain. The inflow is generated using the flow information inside a flow domain based on the self-similarity hypothesis.

1.4 Objectives and Scope

Large eddy simulation of unsteady wall-bounded turbulent flows at high Reynolds numbers is the principal objective of this dissertation. Two flow geometries are chosen for this purpose, which are a pressure-driven turbulent channel flow and a zero pressure gradient turbulent boundary layer. An in-house LES code is used to solve these flows for different Reynolds numbers. The turbulent channel flow is initially employed due to its simple boundary conditions to investigate the performance of wall modeling. Then, the TBL is considered where the wall modeling is integrated with the rescaling technique. The specific objectives of this study are outlined as follows:

1. **Develop a dynamic wall layer model in a fully developed turbulent channel flow:** A dynamic non-equilibrium wall model is developed for a turbulent channel flow at a high Reynolds number. An innovative technique is proposed to mitigate the log-layer mismatch in wall-modeling. This would target an improved algorithm/strategy for exchanging the velocity fields between the wall layer and the LES. Filtering the velocity as input to the wall layer based on the location of the interface is investigated. Also, time averaging the flow solution in the wall layer affects the prediction of the wall shear stress, and a quantitative analysis is conducted to achieve an appropriate time period for averaging the wall layer.
2. **Implement rescaling in a developing TBL together with a wall layer model:** In a TBL, the rescaling method provides a computationally efficient approach for performing a simulation on a compact flow domain. The effective implementation of strategies that address both the near-wall region and the inflow in a developing flow is the crucial aspect of a wall-modeled TBL.
3. **Demonstrate the potential of wall modeling to incorporate the effects of wall roughness, especially at high Reynolds numbers:** The effects of wall roughness are studied in the context of wall-modeling of high Reynolds number turbulent channel flows. The effects of wall roughness are modeled by applying a modification to Prandtl's mixing length hypothesis. An alternative strategy is proposed to estimate the wall shear stress at the wall since the wall is covered with roughness elements. The proposed wall model is implemented for rough channel flows at high Reynolds numbers.

1.5 Expected Contributions

This thesis will present an efficient methodology for resolving a high-Reynolds number TBL. Most of the computational tasks in the simulation of a wall-bounded flow are dedicated to resolving the flow field in the near-wall region, where essential turbulent structures appear. Modeling the wall layer circumvents this issue by introducing the flow dynamics as a wall shear stress to the outer layer. Wall layer modeling is accompanied by the challenge of coupling the outer layer to the wall. Strategies to mitigate the log-layer mismatch will be addressed in the context of wall-modeling. Simulation of a zero pressure gradient TBL is used to study the effect of a higher Reynolds number. Recycling and rescaling will be used to implement a compact computational domain for the simulation of high-Reynolds number TBLs. Roughness is an important feature of many wall-bounded flows. However, roughness elements occur in the near-wall region where the flow field is modeled instead of being resolved. This research attempts to incorporate the effects of wall roughness when modeling the wall layer. Roughness elements are replaced by an equivalent roughness height since the outer layer does not interact with the individual roughness elements. However, modeling the effects of roughness is essential for numerical simulation of high Reynolds number flows.

1.6 Outline of Dissertation

A comprehensive review of the pertinent literature is presented in Chapter 2. First, different wall models from hybrid models to wall stress models are discussed. Then, the methodology for generating inflow turbulence in the simulation of turbulent boundary layers is discussed. Chapters 3 and 4 study wall modeled turbulent channel flows at high Reynolds numbers. The numerical methodology for wall-modeled simulations is initially described. The governing equations in LES and the discretization of the first layer of control volumes near the wall are explored. Full details of a dynamic non-equilibrium wall stress model are presented including time averaging and temporal filtering schemes. Then, the wall-modeled LES (WMLES) is investigated for a range of moderate to high Reynolds number turbulent channel flows. The performance of wall-modeling at high Reynolds numbers is substantiated, and the effects of time averaging and temporal filtering are investigated. The contents of this chapter were published in Hosseinzade and Bergstrom (2021).

Large eddy simulation of TBLs is the next objective of this dissertation. It commences with an introduction to a numerical approach for generating realistic turbulence at the inlet of a

computational domain for TBLs in Chapter 5. The boundary conditions are also formulated for the top of the domain and the outlet boundary. Chapter 6 examines the performance of rescaling inflow generation for a moderate Reynolds number TBL. Different flow characteristics such as the skin-friction coefficient and shape factor are examined and compared with experimental data. The sensitivity of the computational domain to grid resolution at the outlet boundary is tested for low resolution computational domains. Finally, wall-modeling is employed to explore the performance of the inflow generation method at higher Reynolds number TBLs.

A new wall stress model is proposed in Chapter 7, which introduces the effects of wall roughness. A literature review on pertinent roughness models is presented, and the numerical methodology to include the effects of wall roughness in the dynamic non-equilibrium wall model is explored. Guided by the available experimental data, the proposed wall model is implemented in symmetric and asymmetric rough channel flows at different Reynolds numbers. This chapter examines the mean velocity profiles, Reynolds stresses, and turbulence kinetic energy production. Finally, Chapter 8 presents the conclusions and contributions of this research and outlines potential future work.

Chapter 2

Background to Wall-modeling and Inflow Generation Methods

There are two main challenges in the simulation of wall-bounded turbulent flows using LES. First, it is required to properly include the effects of the energetic small-scale flow motions near the wall. Wall-modeling is a useful method for including wall effects in LES. Hence, the first part of this chapter attempts to provide a comprehensive background in wall-modeling methods, especially at high Reynolds numbers. The second challenge relates to the need for defining physically realistic flow conditions at boundaries in the simulation of TBLs. Hence, the second part of this chapter is dedicated to boundary conditions in generating realistic turbulence at the inlet boundary. A review of well-known inflow generation methods is presented for turbulent boundary layers. Finally, the methods implemented in this thesis are introduced.

2.1 Wall-modeling

Despite of the advantages of LES in resolving the large turbulent flow structures, it suffers from the excessive computational cost of resolving the flow in the near-wall region, which is characterized by extremely small length scales. The viscous length scale is typically used to scale the spatially filtered flow structures close to a solid surface, which contain much of the energy in a turbulent flow. On the other hand, the viscous length scale is inversely proportion to the Reynolds number (Pope, 2000). A coarse grid in the wall region will contain many small eddies. Instead of resolving these small motions, a wall model will consider time-

averaged effects (Piomelli and Balaras, 2002). The time step determined by the outer flow is sufficiently large that the small eddies experience several life cycles during each time step. For a sufficient number of near-wall eddies, one could consider the time-averaged statistics of the flow dynamics and their effects on the outer layer. For wall-modeling, the LES needs to implement a coarse grid in the wall layer on the order of $\Delta x^+, \Delta z^+ > 500$ in the wall parallel directions and $y^+ > 50$ in the wall-normal direction.

Deardorff (1970) proposed the idea of wall-modeling for the first time, and later Schumann (1975) developed an innovative approach. Schumann (1975) introduced the wall shear stress as an approximate wall boundary condition in the simulation of a turbulent channel flow. He suggested relating the local wall shear stress to the local instantaneous velocity. If the plane-averaged streamwise velocity (u) at the first grid point is considered to be in the logarithmic law region, then the instantaneous wall shear stress in the streamwise direction ($\tau_{w,xy}$) varies around the mean value as given below:

$$\tau_{w,xy} = \frac{\langle \tau_w \rangle}{\langle \tilde{u}(x, Y, z) \rangle} \tilde{u}(x, Y, z), \quad (2.1)$$

where $\langle \cdot \rangle$ indicates the mean value, x and z represent the location in the wall-parallel plane, and Y is the distance of the first node from the wall. Assuming a linearly varying spanwise velocity (w) and a constant viscosity the local spanwise wall shear stress is determined as follows:

$$\tau_{w,zy} = \mu \frac{\tilde{w}(x, Y, z)}{Y}. \quad (2.2)$$

The wall-normal velocity v is zero at the wall. Later, Piomelli et al. (1989) proposed that the local wall shear stress should relate to the instantaneous velocity at a distance Δ_s downstream of the specified location to consider the inclination of elongated vortical structures;

$$\begin{aligned} \tau_{w,xy} &= \frac{\langle \tau_w \rangle}{\langle \tilde{u}(x, Y, z) \rangle} \tilde{u}(x + \Delta_s, Y, z), \\ \tau_{w,zy} &= \frac{\langle \tau_w \rangle}{\langle \tilde{u}(x, Y, z) \rangle} \tilde{w}(x + \Delta_s, Y, z), \end{aligned} \quad (2.3)$$

where Δ_s is approximated by the empirical correlation $\Delta_s = Y \cot \alpha$ (α is 8° for $30 < Y^+ < 50$ and 13° for larger values of Y^+). These changes improved the results through a closer agreement with the experimental data for a plane channel flow. This simple algebraic correlation suffices to transmit the effects of the wall to the outer flow where there is no pressure gradient. In high-Reynolds number and separated flows, the effects of pressure gradient and advection are significant and should be considered in the wall region. Hence,

the full boundary layer partial differential equations were proposed to resolve the wall layer and estimate the wall shear stress (Balaras et al., 1996). Different wall models have been proposed which can be categorized in two main groups as shown in Fig. 2.1. The Hybrid RANS/LES approaches are constructed based on two distinct layers, whereas the wall layer is modeled as an embedded layer in the wall stress models. The following sections elaborate on the most popular approaches to wall-modeling.

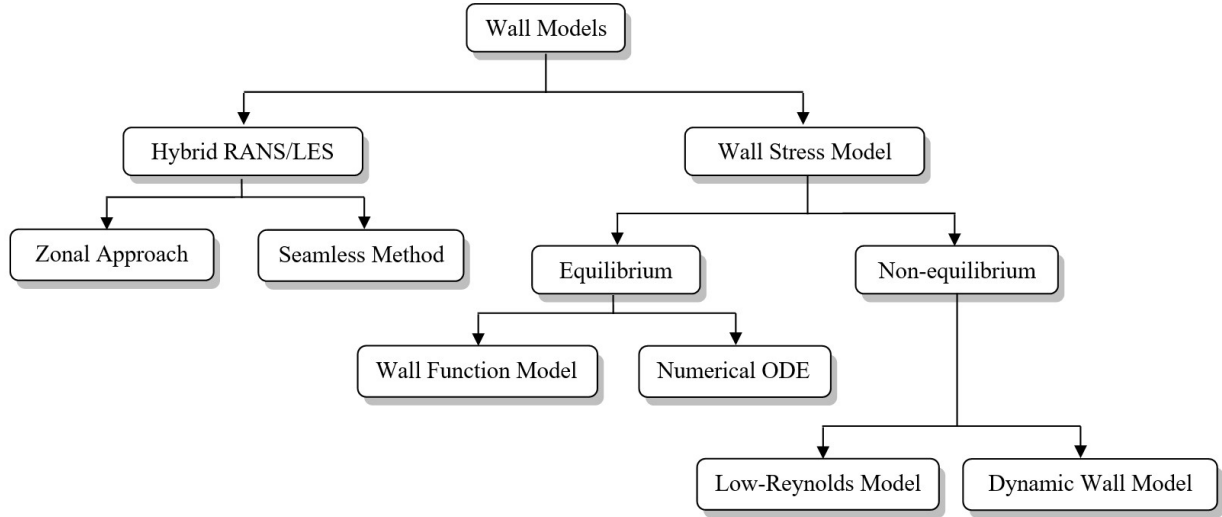


Figure 2.1: Categories of wall models for high-Reynolds number turbulent flows.

2.1.1 Hybrid RANS/LES Wall Model

The hybrid RANS/LES approaches can be classified into two different groups (Larsson et al., 2016; Chaouat, 2017). The first group, referred to as the zonal method, relies on two different models, i.e. a RANS turbulence model and an SGS model. Each of them is implemented in a specific domain to model the turbulent fluctuations. A sharp or dynamic interface transmits the information from the RANS to LES domain. The zonal methods are not limited to RANS/LES, and different approaches can be implemented in each domain such as in the very large eddy simulation (VLES) of Speziale (1998) or the scale adaptive simulation (SAS) of Menter and Egorov (2005). The second group is the seamless method in which the location of the interface is dependent on the flow field solution and/or the grid. The governing equations in the seamless methods transition between RANS and LES behaviors according to updated criteria during the computation. The most well-known seamless method is the detached eddy simulation (DES) used as a wall model by Nikitin et al. (2000).

Interestingly, both the zonal and seamless hybrid RANS/LES methods over-predict the mean velocity profile around the interface in comparison with experimental data. A review of hybrid methods and their performance for separated flows was provided by Heinz (2020), which identified some promising models for this category of the wall-modeling. Although several hybrid methods have been proposed, the main drawback is the fundamental inconsistency of the RANS and LES equations due to their temporal framework (the instantaneous solution obtained from LES in contrast to the time-averaged solution from RANS). The unsteady LES approach produces fluctuations whereas the RANS is incompatible with such fluctuations. Hence, an artificial buffer layer and unrealistic physical structures are expected in hybrid methods. The numerical errors associated with the unrealistic interface might contaminate the flow solution in the LES domain away from the matching layer. Recently, a consistent match between the RANS and LES equations has been developed by enforcing an additional source term to provide proper boundary conditions at the interface (Xiao et al., 2017). Nonetheless, the computational cost associated with this modification is comparable with the cost of LES. In another solution, a blending function was introduced to the interface that smoothly changes the mixing length scale from the turbulence model in RANS to the SGS model in LES (Shur et al., 2008). It is not yet clear whether this method is robust at different grid resolutions or for different numerical methods.

2.1.2 Wall Stress Model

Wall stress models are considered as the second group of wall-modeling approaches. In contrast to the hybrid methods, the wall shear stress is introduced to the LES as a new boundary condition as shown in Fig. 2.2. j indicates the number of the control volume starting from the wall, and u_n is the wall-normal velocity. The wall-modeling grid is embedded

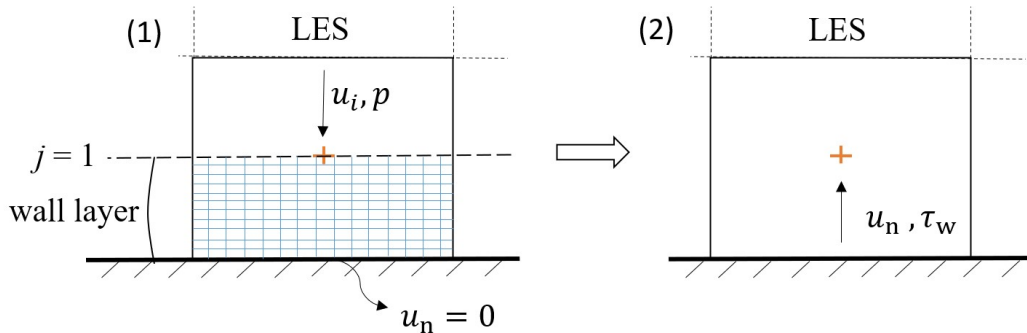


Figure 2.2: Transferring data at the matching point between the wall layer and LES.

inside the LES domain, and flow information is introduced as the top boundary conditions to the wall layer. As shown in Fig. 2.1, there are different approaches in the wall stress models; however, the two most popular models are discussed in the following sections, i.e. the wall function model and the dynamic non-equilibrium wall model. For a more detailed review of other wall-modeling methods refer to Piomelli and Balaras (2002), Larsson et al. (2016), and Bose and Park (2018).

2.1.3 Wall Function Model

Wall functions have been developed to produce a low-cost method to estimate the resistance of the wall region to the momentum transport above (Craft et al., 2004). Empirically derived velocity profiles are used to construct the wall functions. Wall functions are restricted to simple flows where the turbulence production and dissipation are in balance. The wall function is classified as a wall stress model in Fig. 2.1, since it provides a value of the wall shear stress to the LES domain. In an alternative method, the friction velocity is replaced by the turbulence kinetic energy ($k = \frac{1}{2}\langle u'_i u'_i \rangle$, where u'_i is the velocity fluctuations) to scale the velocity at the first node (Launder and Spalding, 1974). The performance of wall functions can be improved by applying this modification, especially in non-equilibrium flows.

Most of wall functions scale the velocity using an assumed logarithmic velocity distribution in the wall region of the form

$$\frac{\langle u \rangle}{u_\tau} = \frac{1}{\kappa} \ln \left(\frac{y u_\tau}{\nu} \right) + B, \quad (2.4)$$

where $\langle u \rangle$ is the mean streamwise velocity in the outer layer, κ is the von Karman constant, y is the distance from the wall, u_τ is the friction velocity, and B is a constant. The logarithmic law can also be used conditionally for local instantaneous velocities if the size of the grid cell (filtered volume) is large enough to contain a significant number of inner layer eddies (Piomelli and Balaras, 2002). The instantaneous log-law is strongly dependent on the size of the grid cell and valid when the horizontal grid scale is greater than 1800 in wall units (Nakayama et al., 2004). Eq. 2.4 is similarly implemented to calculate the instantaneous velocity u instead of $\langle u \rangle$. The instantaneous log-law is widely used in meteorology to model the wall layers, while also including some improvements. In a recent study by Bae et al. (2018), the wall function was developed for boundary conditions with transpiration or slip boundary conditions. Their model implements the slip boundary condition as follows to estimate the velocity at the wall:

$$u_i|_{\text{w}} = l_i \frac{\partial u_i}{\partial y} \bigg|_{\text{w}} + v_i, \quad (2.5)$$

where the subscript i indicates the Cartesian direction, “w” indicates the quantity at the wall, v_i is the slip velocity, and l_i is the slip length. Given Eq. 2.5 for the boundary condition, the wall shear stress at the wall is defined by introducing the tangential SGS stress tensor τ_{12}^{SGS} and the slip boundary condition $u_1 u_2|_{\text{w}}$ as follows:

$$\frac{\langle \tau_{\text{w}} \rangle}{\rho} = \nu \left\langle \frac{\partial u_1}{\partial y} \Big|_{\text{w}} \right\rangle - \langle u_1 u_2|_{\text{w}} \rangle - \langle \tau_{12}^{\text{SGS}} \rangle, \quad (2.6)$$

The results indicate that the new wall function can compensate for the deficit or excess of mean momentum at the wall and improve the underestimation of the wall shear stress which is a common problem in wall-modeling.

2.1.4 Dynamic Non-equilibrium Wall Model

The wall-modeling in the wall stress model can be categorized into equilibrium and non-equilibrium models. In equilibrium models, it is assumed that the convection is balanced by the pressure gradient, and the partial differential equation (PDE) converts into an ordinary differential equation (ODE). Hence, the momentum equation can be integrated in the wall-normal direction to estimate the wall shear stress since the viscous forces become dominant in the wall layer (Wang and Moin, 2002). However, most turbulent flows include a pressure gradient and/or significant convection that violates the assumptions of an equilibrium wall model. Balaras et al. (1996) retained all terms of the momentum equation to resolve the wall layer, i.e. the full boundary layer PDEs. This model, the so-called non-equilibrium wall model, can capture some non-equilibrium effects in a turbulent flow. Therefore, it is implemented for flows with separation or complex geometries where the convective term is non-trivial. Low-Reynolds number (LRN) wall models have been developed following Launder and Spalding (1974). The turbulence kinetic energy is solved in the near-wall region where the shear stress is considered constant, and a linear variation is assumed for the turbulent length scale across the wall layer.

Amano (1984) solved the transport equations for both the dissipation ε and turbulence kinetic energy k using cell-averaged production and dissipation rates to estimate the Reynolds stresses and subsequently the wall shear stress. His model predicts separated and reattached flows accurately, and the wall proximity characteristics are independent of flow Reynolds number. However, the computational cost of the $k-\varepsilon$ model resulted in applying assumptions that simplify LRN models. Solving the full PDEs requires a separate grid in the wall region that should have similar grid resolution requirements to a RANS grid. This is the main

disadvantage of non-equilibrium wall models. Iacovides and Launder (1984) assumed that the pressure variations across the wall layer are negligible. This assumption avoids solving the pressure field in the wall layer, which provides a low-cost model. Instead of the pressure, the wall-normal velocity is calculated from the continuity equation to conserve mass in the wall layer. Craft et al. (2004) discretized the boundary layer transport equations using the finite-volume method in one dimension along the wall. The diffusion term is only integrated in the wall-normal direction, and a simplified LRN model is applied to determine the eddy viscosity. The main drawback of the LRN wall models is that they are generally computationally expensive due to solving additional transport equations for the dissipation and turbulence kinetic energy. Balaras and Benocci (1994) proposed the thin boundary layer equations (TBLE) for a square duct which solve the wall layer as follows:

$$\frac{\partial \langle u_i \rangle}{\partial t} + \frac{\partial \langle u_n u_i \rangle}{\partial y} = -\frac{1}{\rho} \frac{\partial p}{\partial x_i} + \frac{\partial}{\partial y} \left[(\nu + \nu_t) \frac{\partial \langle u_i \rangle}{\partial y} \right], \quad (2.7)$$

where the subscript “n” indicates the wall-normal direction, and ν_t is the eddy viscosity. Eq. 2.7 is solved in wall-parallel planes, and the wall-normal velocity is obtained by solving the continuity equation. A very simple mixing length model is used to estimate the eddy viscosity and close the governing equations. Similarly, the wall layer is assumed to be sufficiently thin that the pressure gradient across the wall layer is zero. Thus, the pressure information is that imposed by the outer layer and is introduced to a source term. Moving to higher Reynolds number flows, Balaras et al. (1996) suggested including the streamwise advection in the TBLE:

$$\frac{\partial \langle u_i \rangle}{\partial t} + \frac{\partial \langle u_1 u_i \rangle}{\partial x} + \frac{\partial \langle u_n u_i \rangle}{\partial y} = -\frac{1}{\rho} \frac{\partial p}{\partial x_i} + \frac{\partial}{\partial y} \left[(\nu + \nu_t) \frac{\partial \langle u_i \rangle}{\partial y} \right], \quad (2.8)$$

where the subscript 1 denotes the streamwise direction.

There are different methods for estimating eddy viscosity. The conventional zero-equation eddy viscosity based on the mixing length hypothesis proposed by Prandtl (1925) and introducing a damping function for the inner part of a boundary layer is represented as follows:

$$\begin{aligned} \nu_t &= (\kappa y)^2 \left| \frac{\partial \langle u \rangle}{\partial y} \right| \mathcal{D}, \\ \mathcal{D} &= \left[1 - \exp(-y^+/A^+) \right]^2, \end{aligned} \quad (2.9)$$

where \mathcal{D} is the van Driest wall damping function, $y^+ = y u_\tau / \nu$ is the distance from the wall in inner coordinates, and A^+ is a constant. Johnson and King (1985) showed that Eq. 2.9 is valid for non-zero pressure gradient flows, and it reduces to $\nu_t = \kappa y u_\tau \mathcal{D}$ for zero pressure

gradient flows with a simple adjustment in the damping function to replace y^2 dependency with a y dependency. They used $A^+ = 15$ for zero pressure gradient flows compared to $A^+ = 26$ for non-zero pressure gradient turbulent flows. There are several studies based on the zero-equation eddy viscosity model that implemented different formulations in different flow geometries as shown in Table 2.1.

Table 2.1: Different zero-equation eddy viscosity models.

Models	Flow	ν_t	\mathcal{D}	A^+
Johnson and King (1985)	ZPGTBL	$\kappa y u_\tau \mathcal{D}$	$1 - \exp(-y^+/A^+)$	15
Johnson and King (1985)	NZPGTBL	$(\kappa y)^2 S \mathcal{D}$	$1 - \exp(-y^+/A^+)$	26
Balaras et al. (1996)	Channel	$(\kappa y)^2 S \mathcal{D}$	$1 - \exp(-y^+/A^+)^3$	25
Cabot (1995)	Channel	$\kappa y u_\tau \mathcal{D}$	$[1 - \exp(-y^+/A^+)]^2$	19
Cabot and Moin (2000)	Channel	$\kappa y u_\tau \mathcal{D}$	$[1 - \exp(-y^+/A^+)]^2$	17
Kawai and Larsson (2013)	ZPGTBL	$\kappa y u_\tau \mathcal{D}$	$[1 - \exp(-y^+/A^+)]^2$	17

ZPGTBL: zero pressure gradient turbulent boundary layer

NZPGTBL: non-zero pressure gradient turbulent boundary layer

The eddy viscosity ν_t indicated in Eqs. 2.7 to 2.9 not only represents the effects of the residual Reynolds stresses but also should include the effects of subgrid scale stresses introduced by the outer layer, which indicates the essential role of the eddy viscosity in non-equilibrium wall models. Cabot and Moin (2000) reviewed wall stress models and found that the eddy viscosity model over-predicts the magnitude of the eddy viscosity using the zero-equation model. The LES resolves a portion of the non-linear stresses at the interface using a coarse grid. The wall model and LES use the same wall-parallel grid resolution and velocities at the interface. Hence, the non-equilibrium wall model is assumed to predict only the unresolved portion of stresses to estimate an accurate wall shear stress. In this regard, Wang and Moin (2002) suggested the turbulent eddy viscosity in the wall layer should match the SGS eddy viscosity at the interface which is represented by use of a dynamic value of κ , i.e. $\kappa = \langle \nu_{\text{SGS}} \rangle / \langle y^+ \mathcal{D} \rangle$ with $\mathcal{D} = [1 - \exp(-y^+/A^+)]^2$. The angle bracket here refers to a spatial average in the spanwise direction and a time-average over a certain number of previous time steps. This model, the so-called dynamic wall model, later was further developed by Kawai and Larsson (2013) where the von Karman constant κ varies linearly from the wall to the matching point,

$$\kappa = 0.41\mathcal{K} + \hat{\kappa}(1 - \mathcal{K}), \quad (2.10)$$

where $\hat{\kappa} = \langle \nu_{\text{SGS}} \rangle / \langle h_{\text{wm}} u_\tau \mathcal{D} \rangle$, h_{wm} is the height of the wall layer, and \mathcal{K} is a function of y , the distance from the wall, and varies between 0 and 1. They asserted that up to a specific height, there is no effect of the resolved stress, and the standard value ($\kappa = 0.41$) can be used. Above this height, the κ -value reduces in a linear profile to balance the turbulent eddy viscosity against the SGS eddy viscosity. This critical height is specified using *ad hoc* correlations which failed the dynamic wall model in some high-Reynolds number flows.

Park and Moin (2014) further improved the dynamic wall model by calculating the resolved and modeled Reynolds stresses separately. They proposed that the Reynolds stresses in the conventional RANS equations should balance the resolved and modeled stresses in the non-equilibrium wall model as follows:

$$2\nu_t \bar{S}_{ij} - \frac{2}{3} k \delta_{ij} - \bar{R}_{ij} \approx 2\nu_t^* \bar{S}_{ij} - \frac{2}{3} k^* \delta_{ij}, \quad (2.11)$$

where S_{ij} is the strain rate tensor, δ_{ij} is the Kronecker delta, $\bar{R}_{ij} = -\overline{u'_i u'_j}$ is the resolved Reynolds stress, and superscript $*$ indicates the value is modeled using the correlations presented in Table 2.1 with the standard value of the model coefficients. The right-hand side of Eq. 2.11 refers to the total Reynolds stresses. The first two terms on the left-hand side are the modeled Reynolds stresses and the third term, \bar{R}_{ij} , is the resolved Reynolds stresses in the non-equilibrium wall model. Applying the least squares method to Eq. 2.11, an eddy viscosity related to the unresolved Reynolds stresses can be obtained. They validated this model in a separating flow over an airfoil, a high-Reynolds number turbulent boundary layer, and a channel flow, and results were in good agreement with the references.

2.1.5 Other Wall Models

Besides the zero-equation eddy viscosity models, other methods have been used to approximate the wall boundary conditions. The linear stochastic estimate (LSE) method was developed to predict the wall shear stress using the best mean square estimate instead of first order statistics (Bagwell et al., 1993). A set of linear estimations was introduced to relate the averaged wall shear stress to a vector of events such as the local velocity field, pressure, velocity gradients, quadratic products, or any other quantities that characterize the wall stresses. A two-point spatial correlation tensor is implemented to resolve the coherent structures in the wall layer and provide an accurate estimation of the wall shear stress. This model works very well in low-Reynolds number channel flows, but for high Reynolds numbers the success is limited, perhaps due to a weak linkage between errors in the outer layer and wall models.

Nicoud et al. (2001) implemented a controller for the LSE method for wall stress fluctuations by introducing an additional time integration. In the control process, they only considered discrete terms of the momentum equation explicitly at the current time step and ignored any old values. This model, which is the so-called suboptimal control model, introduces a cost function based on the difference between the mean velocity and the log-law. They also considered the effects of wall shear stress in the cost function. By optimizing the cost function at each time step, the local wall shear stress is estimated for the next time step. Notwithstanding the acceptable performance of the suboptimal control model for coarse-grid high-Reynolds number LES, the cost is much larger than the cost of explicit wall stress models.

Chung and Pullin (2009) developed an ODE using a stretched-vortex SGS model to estimate the wall shear stress without the need to resolve the wall layer. A filtered governing equation is discretized in the wall-normal direction while only streamwise diffusion is considered and the pressure-gradient across the wall layer is assumed to be negligible. Applying this ODE to the first cell near the wall and using the resolved-scale LES quantities to determine other terms, the wall shear stress is obtained. This model can be applied to inhomogeneous turbulent flows since it is entirely local. The proposed model has been used in channel flows over a wide range of Reynolds numbers with acceptable outcomes. However, the prediction of separated flows using the reduced form of the TBLE is questionable.

Duprat et al. (2011) developed an ODE for the wall layer modeling based on a simple relation proposed by Wang and Moin (2002). They neglected the convective transport and temporal terms in Eq. 2.8. The pressure gradient and diffusion terms are retained and integrated over the wall-normal direction to give

$$0 = -\frac{1}{\rho} \frac{\partial p}{\partial x} y + (\nu + \nu_t) \frac{\partial \langle u \rangle}{\partial y} - \frac{\tau_w}{\rho}. \quad (2.12)$$

A different scaling is applied to Eq. 2.12 to make it dimensionless. Instead of the friction velocity u_τ , an extended inner scaling is implemented as follows:

$$u^* = \frac{\langle u \rangle}{u_{\tau p}}, \quad y^* = \frac{y u_{\tau p}}{\nu}, \quad (2.13)$$

where $u_{\tau p} = \sqrt{u_\tau^2 + u_p^2}$, and the additional velocity scale u_p is related to the streamwise pressure gradient, $u_p = [\nu/\rho (\partial p/\partial x)]^{1/3}$. The advantage of this scaling over the classical wall coordinates is that it remains valid even for separated and reattached flows ($u_\tau = 0$).

Hence, Eq. 2.13 is expressed as

$$\frac{\partial u^*}{\partial y^*} = \frac{\text{sign}\left(\frac{\partial p}{\partial x}\right) (1 - \alpha)^{3/2} y^* + \text{sign}(\tau_w) \alpha}{1 + \frac{\nu_t}{\nu}}. \quad (2.14)$$

For further description of α , ν_t , and “sign” in their relation see Duprat et al. (2011). This wall stress model was tested on adverse and favorable pressure gradient flows, and the results were in good agreement with DNS. Furthermore, the matching point in this model can be located from the viscous sublayer ($y^+ = 5$) to the log layer ($y^+ = 120$). The wall model predicts the wall stress very well; however, its performance at high Reynolds number is questionable since the convection term is neglected.

Bose and Moin (2014) proposed a slip boundary condition using a modified low-pass differential filter for wall-bounded turbulent flows to specify the filtered velocity with no estimation of the wall shear stress. They considered a second-order linear operator of elliptic filters to find the velocity at the wall as described by

$$\tilde{\phi} - \frac{\partial}{\partial x_i} \left(l_p \frac{\partial \tilde{\phi}}{\partial x_i} \right) = \phi, \quad (2.15)$$

where $\tilde{\phi}$ is the filtered scalar, l_p is the length scale regularization parameter, and ϕ is the unfiltered variable or the actual value. Employing Eq. 2.15 at the wall in directions tangential to the wall surface, it can be assumed that $l_p = 0$ and the filter width gradient is $\frac{\partial l_p}{\partial x_k} = 0$. Hence, the velocity at the wall is as follows ($\phi = u$):

$$\tilde{u}_i - C \Delta_w \frac{\partial \tilde{u}_i}{\partial y} = 0. \quad (2.16)$$

Note that the actual velocity at the no-slip wall is assumed to be $u|_w = 0$. The magnitude of $C \Delta_w$, which is known as the slip length, represents the filter length scale at the wall and is estimated through the use of the Germano identity. Using Eq. 2.16 for a wall-modeled LES on a coarse mesh, the filter width is a non-vanishing length scale, which results in the tangential velocity at the wall. This dynamic slip wall-modeling predicts separated and attached flows correctly when the LES grid size is refined in the wall-normal direction compared with previous wall stress models. However, it is sensitive to the SGS model and numerical method used. In contrast to the dynamic slip wall model studied by Bae et al. (2018), this dynamic model represents the filtered velocity as a boundary condition to the LES domain instead of the wall shear stress.

Yang et al. (2015) developed an integral wall model based on the RANS equations in which the wall-normal velocity is obtained by integrating the continuity equation from the wall to the matching point. They asserted that their integral WMLES considers all the physics of the inner layer such as the pressure gradient, advection, and unsteadiness. Their model treated the solid surface as an immersed boundary. Although the integral wall model evaluates roughness effects with acceptable results, it is mathematically complicated and requires constrained coefficients in the LES to control the coupling of the wall layer to turbulent fluctuations in the LES region.

Suga et al. (2019) further investigated non-equilibrium wall stress models to develop a simple ODE from the TBLE. They considered the TBLE in the wall-normal direction and assumed that all terms except the diffusion term are constant inside a near-wall cell. This assumption simplified the TBLE to a reduced-form ODE. In this analytical wall function, the eddy viscosity is estimated using a one-equation-like correlation that contains the turbulence kinetic energy and the dissipation length scale based on the filtered velocity field. The model was studied in turbulent channel flows for a limited range of Reynolds numbers. It was shown that the log-layer mismatch can be suppressed using the algebraic non-equilibrium wall stress model.

Among the wall models discussed, the dynamic non-equilibrium wall model proposed by Park and Moin (2014) has the potential for the simulation of TBLs. The wall model implements the TBLE to resolve the flow motions in the near-wall region and requires no flow information *a priori*. It is less sensitive to the location of the matching point and successfully predicts both separated and reattached flows. Although the dynamic non-equilibrium wall model has demonstrated good performance, further studies are required on the coupling of the LES domain and wall layer at the matching point since they are based on two different temporal frameworks. The flow statistics inside the wall layer should also be investigated to determine a proper time averaging scheme. In this regard, the present thesis seeks to improve the performance of the dynamic wall-model, as will be discussed in Chapter 3.

2.2 Inflow Generation Methods

Spatially developing turbulent flows such as boundary layers are challenging due to their high computational memory size and simulation run-time. The advent of supercomputers has improved spatial and temporal resolution for a given computational cost. However, obtaining a simulation with coherent flow structures depends on creating a realistic turbulent flow at

the inflow. To achieve real turbulent flow structures, the most straightforward approach is to calculate the boundary layer from the leading edge. Although realistic turbulence fluctuations are achievable, the high computational cost of a long computational domain and limited Reynolds numbers are the main drawbacks of this method. This issue has led to the development of inflow generation methods that prescribe realistic turbulence at the inlet boundary. Physically realistic boundary conditions are necessary at all boundaries of a computational domain, but for a boundary layer the inlet is especially important. Generating realistic turbulence at the inflow affects the downstream flow dynamics over the entire domain.

An efficient inflow generation method should be able to faithfully recreate desired turbulence statistics by enforcing the two-point spatial correlations, higher-order moments, and spectral distribution of turbulence kinetic energy (Dhamankar et al., 2018). The method should require no further adjustment at the inlet to introduce realistic turbulence without spurious artifacts like non-physical periodicity or acoustic waves. Generating continuous flow statistics at the inflow boundary during a simulation without the need for storing and reading the inflow data is another feature of an effective inflow generation method. The method should be easily implemented in parallel computational cores and adjustable to a variety of flow problems. Furthermore, it should be compatible with different spatial discretization methods (finite volume method or finite difference method) and grid types (structured and unstructured grids).

There are various techniques to introduce inflow boundary conditions ranging from cyclic approaches to artificial turbulence methods. Any errors within the inflow generation model require a development section downstream of the inlet boundary to eliminate unrealistic turbulence fluctuations. In general, turbulent inflow generation methods are categorized as: 1) transition-inducing methods, 2) library-based methods, 3) synthetic methods, and 4) recycling methods (Bazdidi-Tehrani et al., 2016; Dhamankar et al., 2018). Fig. 2.3 summarizes the main methods and subcategories for generating inflow turbulent boundary conditions for boundary layers.

2.2.1 Transition-inducing Methods

To generate real turbulent flow dynamics, a straightforward approach is to impose a disturbance to the laminar regime and resolve the transition to turbulence. This is in contrast to natural transition where Tollmien-Schlichting waves would be formed. Resolving natural transition requires a long domain which only makes it appropriate when the transition pro-

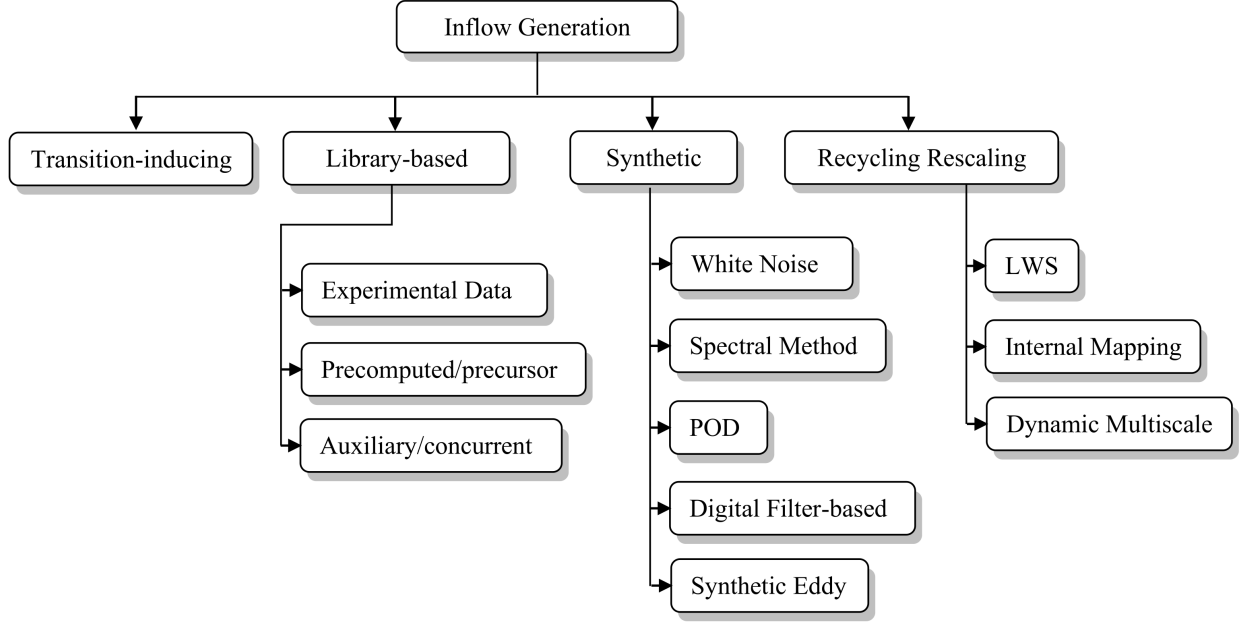


Figure 2.3: Categories of inflow generation methods.

cess is the focus of the research (Fasel et al., 1990; Sayadi et al., 2013). In general, a desired mean velocity profile with superimposed random fluctuations is introduced far upstream in the laminar region, and the turbulent boundary layer is spatially developed within the flow domain after the transition to turbulence. Most solvers implement dissipative methods to enhance the numerical stability which can smooth out small fluctuations in the flow field. A very long computational domain and limited Reynolds numbers are the main disadvantages of the transition-inducing method.

2.2.2 Library-based Methods

Library-based methods rely on an outside source to generate the inflow data for the main simulation. A separate precursor simulation, that is most often a channel flow, is simulated using periodic boundary conditions to achieve fully developed realistic turbulence (Keating et al., 2004). The velocity field in a plane normal to the streamwise direction is either stored to be used for a later simulation or simultaneously introduced at the inlet boundary of the main simulation. Li et al. (2000) stored a time series of velocity planes in a periodic simulation with time intervals comparable to the integral time scale. They transformed this signal into a periodic one that could be used for unlimited time steps in a spatially developing turbulent mixing layer. Schlüter et al. (2004) proposed a variant of the library-based method for hybrid RANS/LES simulations. This method imposes precomputed turbulent fluctuations

on a target mean velocity profile that can develop into realistic eddies. The flow database can also be used for different flow configurations and Reynolds numbers by scaling the flow statistics obtained from the precursor simulation to produce appropriate flow structures. The proposed method was implemented in a confined swirling flow, and the results were in good agreement with the experimental data. Use of a precursor simulation to produce a library or database of the turbulent flow for the main simulation increases the computational cost. Druault et al. (2004) used experimental data to estimate the inflow boundary conditions based on a proper orthogonal decomposition (POD) method and linear stochastic estimation. Their method extracts coherent structures to predict the behavior of large-scale structures at an inflow section and couples them with random fluctuations to make realistic turbulence.

An alternative method is to generate the inflow data simultaneously by running an auxiliary simulation as shown Fig. 2.4. The geometry and operating conditions of the auxiliary domain are analogous to the main domain. The auxiliary simulation runs to achieve a fully developed turbulent flow using periodic boundary conditions (Spalart, 1988) or recycling methods which will be discussed in Section 2.2.4 (Lund et al., 1998). Then, the velocity field at a sampling location is introduced to the inlet plane through a communication channel at each time step. Although a library-based method supplies physically realistic turbulent flow structures, which are temporally and spatially correlated, it is impractical for a wide variety of flow geometries (Dhamankar et al., 2018).

2.2.3 Synthetic Methods

For synthetic turbulence methods, pseudo-random artificial unsteadiness is produced and superimposed on a predefined mean flow to provide flow data at the inlet of a computational domain. There are various ways to generate pseudo-random fluctuations which include white-noise random fluctuations (Neto et al., 1993), spectral approaches (Lee et al., 1992), POD (Druault et al., 2004), digital filter-based inflow (Klein et al., 2003), and synthetic eddy methods (Jarrin et al., 2006). In some methods like the white-noise fluctuations, inflow data lack spatial and temporal coherence, and superimposed fluctuations are suppressed within a short distance downstream. Lee et al. (1992) proposed a method in which random fluctuations were estimated by a predefined power spectrum. This ensures that small-scale flow motions contain insignificant energy whereas the highest level of energy is assigned to well-resolved eddies. Turbulent statistics such as vorticity and turbulence intensity indicated good agreement with the experimental data, while the statistics of the dilatation showed differences. Later, Le et al. (1997) modified this approach by scaling the velocity fluctuations

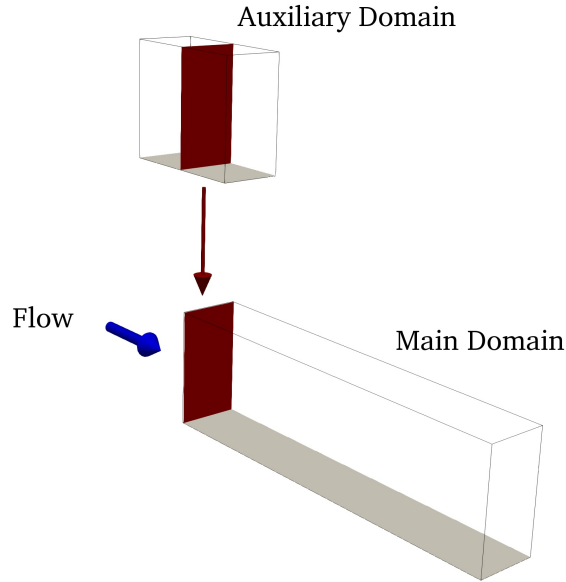


Figure 2.4: Library-based inflow generation method using an auxiliary simulation in a turbulent boundary layer.

to be comparable with the target Reynolds stresses and inlet boundary layer profile. The generated signals demonstrated satisfying second-order statistics, but they lost the statistical characteristics shortly after the inlet plane and only re-established realistic turbulence after a transition length. Physically realistic turbulence flow structures are obtained after the initial developing region and constructing phase information between real turbulent structures.

Keating et al. (2004) reviewed various inflow conditions for LES to reveal the role of phase information in generating appropriate inlet boundary conditions. They showed that uncorrelated random noise and small-scale eddies will dissipate quickly, and the library-based method using a separate calculation needs flow structures comparable to or larger than the integral length scale. It was found that the synthetic turbulence generation using reduced information from RANS simulations is more successful in developing realistic turbulence than using the Reynolds stress information due to imposing the increased wall-normal velocity fluctuations. Batten et al. (2004) proposed a synthetic turbulence generation method that controls the second moment and wavelength spectra. Their model superimposed random frequencies and wavenumbers on sinusoidal modes that stretched eddies in the direction of the larger Reynolds stresses. This is accompanied by more realistic anisotropic eddies, especially near the wall. A synthetic digital filtering method has been proposed by Béchara et al. (1994) where the velocity signals are spatially correlated using an imposed energy spectrum.

The summation of Fourier modes was implemented to approximate homogeneous isotropic turbulence at the inlet boundary. The lack of temporal correlation between two instants resulted in white noise instead of real turbulence. A digital filter through convolution with a Gaussian filter was used to impose a temporal coherence over a random temporal sequence. Klein et al. (2003) suggested imposing spatial coherence on random spatial data points to generate artificial velocity data with second-order statistics and a realistic autocorrelation function. The model implements an inverse Fourier transform and has the advantages of defining the length scale locally in each coordinate direction and being adaptable to the recorded experimental data as input.

In general, most synthetic turbulence methods are unreliable in practical applications. The efficiency of synthetic approaches is strongly dependent on the length of the initial development region required to establish turbulent flow structures, which is the main drawback of these methods. These methods produce a Reynolds stress budget that may be different than the one in a real turbulent flow (Keating et al., 2004). Furthermore, the dissipation depends on the implemented model spectrum in the synthetic method, whereas the spectral distribution of turbulence affects the dissipation in a turbulent flow. This issue results in a rapid decay of the wall-normal Reynolds stresses, and consequently a lower production and reduced streamwise Reynolds stresses. However, the flow redevelops towards more realistic turbulence some distance downstream after the transition process. This implies that the synthetic methods still require a fairly long development region to establish physically realistic turbulent structures.

2.2.4 Recycling Methods

The concept of recycling was proposed by Spalart and Leonard (1987) where the spatial growth of the boundary layer is controlled by the skin friction and momentum thickness to generate realistic turbulence using a form of periodic boundary conditions in the streamwise direction. A systematic multiple scale procedure was used to estimate the boundary layer growth. The NSEs are transformed into a new coordinate system in which the streamwise velocity field is homogeneous. As a result, several terms are introduced to the governing equations that are complicated to estimate. Although their method had advantages over previous periodic methods, it has been implemented in only a few studies to generate inflow data. Lund et al. (1998) modified Spalart and Leonard’s (1987) method by computing the spatial development of boundary layer in a Cartesian coordinate system. Their approach, known as the LWS (Lund-Wu-Squires) method, extracts instantaneous velocities at a recy-

cling plane downstream which is fairly far from the inlet plane as shown in Fig. 2.5. Then, the velocities are decomposed into the mean and fluctuating components. Each component is rescaled by applying wall or outer coordinates depending on its location from the wall. The rescaled fluctuating component is imposed on the rescaled mean component and introduced to the inlet boundary. All terms in the LWS method used to rescale the velocities are directly estimated from the mean flow field, and merely a single empirical correlation is used to relate the law of the wall at the inlet boundary to the flow field downstream.

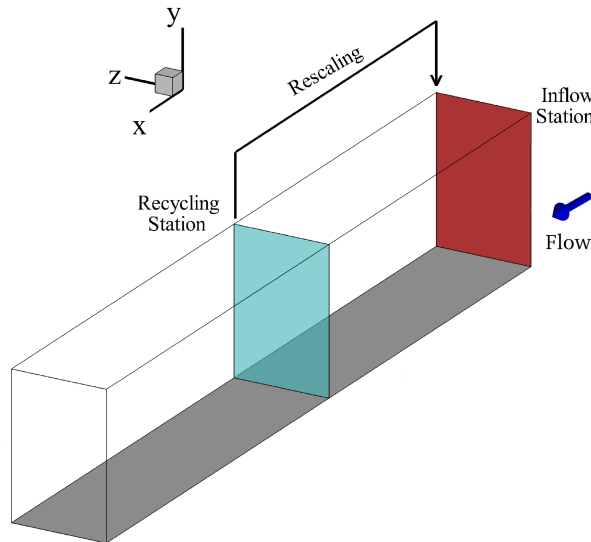


Figure 2.5: A schematic of recycling rescaling inflow generation.

Lund et al. (1998) performed the simulation of a TBL in two distinct domains. The first domain (driver) was shorter and used as a library database for the second domain, which was the main simulation as shown in Fig. 2.4. The recycling rescaling inflow generation method was implemented in the first domain. Once the flow solution in the driver domain became statistically stationary, the flow data from the mid-plane were extracted and used to update the inlet boundary condition of the main domain. Kataoka (2008) simplified the LWS method by recycling only the fluctuation components. He prescribed a constant mean velocity profile at the inlet and introduced the recycled-rescaled fluctuating components to the mean velocity. This led to a shorter length in the driver domain in contrast with LWS. Ferrante and Elghobashi (2004) suggested a modification to the LWS method by estimating the energy spectrum and Reynolds stresses in the driver domain and introducing additional steps before the rescaling process. This method preserves the production rate of turbulence kinetic energy, and a statistical correlation between the Reynolds stresses near the wall is sustained. As a result, a constant value for the velocity-derivative skewness is achieved

throughout the simulation which ensures vortex stretching and the transfer of energy from large-scale eddies to smaller vortices.

Despite the acceptable performance of the LWS method in flat-plate boundary layers, there are some inherent limitations. For instance, it needs an equilibrium region to develop the scaling terms (Dhamankar et al., 2018). In complex geometries, it is required to make an additional region upstream where the scaling laws become valid. This is in contrast to the main advantage of the LWS method which is producing a fully developed boundary layer without adjustments at the inlet. Furthermore, there is a potential for contaminating the solution by introducing spurious low-frequency components, which depend on the location of the recycling station and the mean convective speed of the flow (Morgan et al., 2011). There is also a risk of locking the turbulent structures in the spanwise direction when a short domain is used due to its lower computational cost for the inflow turbulence generation with periodic boundary conditions. Munters et al. (2016) proposed a clever technique to prevent the spanwise locking in a flow domain without increasing the streamwise domain length. They shifted the recycling plane uniformly in the spanwise direction within a predefined and constant distance. This approach was mainly conducted for channel flows, but it can be extended to the recycling rescaling method for a flat-plate TBL. Jewkes et al. (2011) modified the LWS method by mirroring the flow structures at the inlet boundary to avoid spurious linking between the recycling and inlet planes. They also replaced the boundary layer thickness (δ) with displacement thickness (δ^*) to rescale the outer region since δ is a poorly conditioned parameter and varies with small velocity variations.

Recall that running concurrent simulations (auxiliary and main domains) as used by Lund et al. (1998) increases the complexity of the simulation by transferring the flow data through a communication channel between the auxiliary and main domain. Including the recycling box in the main computational domain, i.e. so-called internal mapping, reduces this complexity and the corresponding computational cost. In an earlier version of the LWS method, Wu et al. (1995) estimated the inflow conditions from the velocity field at a location close to the outflow boundary but in a single domain as shown in Fig. 2.5. Choosing the location of the recycling plane far from the inlet boundary is effective in mitigating the spurious periodicity (Wu, 2017). In contrast, moving the recycling station far downstream may result in uncorrelated time scale and spanwise length scale of flow structures at the recycling and inlet planes and increase errors. However, the internal mapping method has been widely implemented in studies of TBLs (Urbin and Knight, 2001; Tabor and Baba-Ahmadi, 2010; Araya et al., 2011; Inoue and Pullin, 2011).

Later, a dynamic recycling inflow generation method was developed. Liu and Pletcher (2006) pointed out the slow response of the LWS method to generate turbulence downstream. They introduced a dynamic recycling plane which is initially located close to the inlet boundary, and then it moves to a predefined station downstream. The numerical time that they required to develop the TBL is shorter than the LWS method. This method, which is subject to ZPGTBLs, significantly reduces the numerical transient at the beginning of the simulation. However, the proposed recycling rescaling inflow generation methods are unable to produce inflow turbulence in boundary layer flows with pressure gradients. Araya et al. (2011) developed a methodology that relates the velocity and length scales at the inlet and recycling stations through a dynamic multiscale approach in the rescaling process. An additional plane is introduced between the inlet and recycling planes that is the so-called test plane. The development of a boundary layer between the test and recycling planes is monitored to estimate the friction velocity at the inlet. This feature enables the dynamic multiscale method to be used in zero, favourable, and adverse pressure gradient boundary layers. The authors reported that due to the dependence of the flow on the spatial development of the boundary layer downstream, this method is not recommended for boundary layers with strong non-equilibrium transitions like flow separation or relaminarization. However, it can capture the effects of roughness in the inflow generation.

Cardillo et al. (2013) performed the dynamic multiscale approach on a ZPGTBL with a rough surface. They modified the rescaling factors in the dynamic model of Araya et al. (2011) near the wall to consider the effects of surface roughness. The viscous sublayer is disturbed in a boundary layer by the presence of roughness, and the estimation of the friction velocity by traditional methods is difficult if not impossible. Hence, the momentum integral equation is used to calculate the scaling factor at the inner layer based on a power-law variation of the momentum thickness. They evaluated their model on a low-Reynolds number turbulent boundary layer ($Re_\theta = 2077 - 2439$) with a sand grit roughness, and the results showed good agreement with experiments. They found that the effects of the surface roughness on the Reynolds stresses are dependent on the roughness scale.

There are numerous inflow generation methods with some modifications outlined in this study to provide realistic inflow conditions. Bazdidi-Tehrani et al. (2016) investigated the performance of some of the inflow generation methods discussed in the previous sections in the simulation of flow around a model building in a turbulent atmospheric boundary layer. Their study indicated that the recycling method has some advantages over three other methods including the generation of high-frequency velocity fluctuations and larger turbulence intensity, higher energy levels, and coherent structures. Dhamankar et al. (2018)

reviewed inflow generation techniques with more attention given to the synthetic method due to its application in industrial problems.

Although there are successful synthetic methods for the simulation of turbulent boundary layers, the simplicity of the LWS method is compelling. The LWS method recycles the flow dynamics to the inlet plane where they are rescaled using the friction velocities at the recycling and inlet stations. It needs no further analysis such as a power spectrum or phase information. However, the auxiliary domain in the LWS method is a significant disadvantage, which directly affects the computational cost. This study implements the LWS method to generate realistic turbulence at the inlet plane without any auxiliary domain. Instead, the recycling station is located inside the main domain. Locating the recycling station requires careful consideration to avoid contaminating the inflow by numerical errors at the inlet and outlet boundaries, which will be discussed in Chapter 5.

Chapter 3

Numerical Methodology in Wall-modeled Large Eddy Simulation

In LES, the filtered continuity and NSEs are used to resolve the flow dynamics, and the residual stresses are modeled using an SGS model. An in-house LES code is implemented for all simulations in this thesis. The code allows for different SGS models, however, the dynamic nonlinear SGS model proposed by Wang and Bergstrom (2005) is employed for all simulations. This chapter outlines the mathematical equations and numerical methods implemented in the LES and wall-modeling. First, the algorithm for solving the momentum equations for an incompressible flow is elaborated. Spatial and temporal discretization methods are discussed, and the numerical algorithm for applying the wall shear stress at the first node as a boundary condition in the WMLES is explained. To describe the methodology of wall-modeling, the boundary layer equations are introduced. Finally, the method in which the wall layer communicates with the outer layer is presented.

3.1 Governing Equations

The flow of an incompressible Newtonian fluid with constant properties is considered in this study; it is governed by the relations for conservation of mass and momentum as shown in Eqs. 1.5 and 1.6. The governing equations are discretized based on the finite-volume method, and a second-order central-difference scheme is used to approximate all spatial derivatives on a collocated grid. A two-step fractional step method is used to temporally advance the momentum equations. The second-order explicit Adams-Bashforth scheme developed by Kim

and Moin (1985) splits the momentum equation into the following equations:

$$(\tilde{u}_i^* - \tilde{u}_i^n) = \frac{\Delta t}{2} (3H_i^n - H_i^{n-1}) \quad , \quad H_i = -\frac{\partial}{\partial x_j}(\tilde{u}_i \tilde{u}_j + \tau_{ij}^*) + \nu \frac{\partial^2 \tilde{u}_i}{\partial x_j \partial x_j}, \quad (3.1)$$

$$\frac{\tilde{u}_i^{n+1} - \tilde{u}_i^*}{\Delta t} = -\frac{\partial p^{n+1}}{\partial x_i}, \quad (3.2)$$

where Δt is the time step to advance the simulation, ρ is the density of the fluid, the superscript n indicates the current time step, and \tilde{u}_i^* indicates the intermediate velocity in the fractional step method. The new velocity \tilde{u}_i^{n+1} is achieved by solving the pressure field at the second step of fractional step method (shown by superscript $n+1$). A pressure-correction method is implemented to calculate the pressure components by solving the filtered continuity equation.

3.1.1 Pressure-correction Method

Using the finite-volume method and locating the mass flux at the faces of the control volume shown in Fig. 3.1, the continuity equation is given as

$$(\dot{m}_e - \dot{m}_w) + (\dot{m}_n - \dot{m}_s) + (\dot{m}_f - \dot{m}_b) = 0. \quad (3.3)$$

where $\dot{m}_e = \rho \tilde{u}_e A_e$ is the mass flux at the east face, and A_e is the face area at east. Eq. 3.3 can be rewritten as

$$\frac{\tilde{u}_w - \tilde{u}_e}{\Delta x} + \frac{\tilde{v}_s - \tilde{v}_n}{\Delta y} + \frac{\tilde{w}_b - \tilde{w}_f}{\Delta z} = 0. \quad (3.4)$$

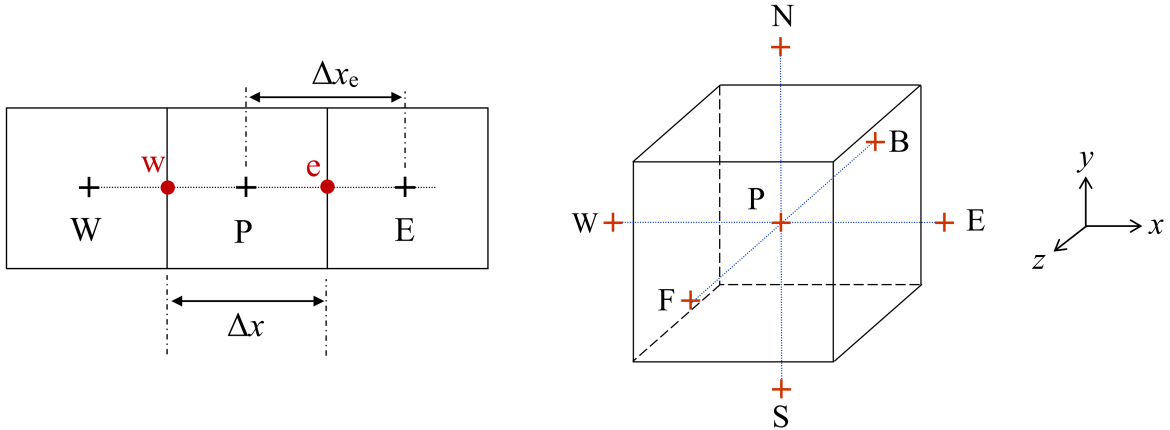


Figure 3.1: A sketch of the control volume used in the pressure-correction method.

The width of control volume in the streamwise, wall-normal, and spanwise directions is shown by Δx , Δy , and Δz , respectively.

The intermediate velocity \tilde{u}_i^* in Eq. 3.2 does not guarantee mass conservation over the control volume, and a velocity correction is required to satisfy continuity. In this regard, the mass flux at the face is linked to the nodal pressure-correction field on a collocated grid, so that

$$\tilde{u}_e = \tilde{u}_e^* - \frac{\Delta t}{\rho \Delta x_e} (p'_E - p'_P), \quad (3.5)$$

where Δx_e is the cell width at the east face as shown in Fig. 3.1, and p' is the pressure correction. Substitution of the corrected velocity in Eq. 3.4 above results in the following discrete Poisson equation for the pressure-correction field:

$$a_P p'_P = \sum a_{NP} p'_{NP} + b, \quad (3.6)$$

where the subscript NP represents the neighbouring nodes, and the coefficients are defined as

$$\begin{cases} a_E = a_W = A_x \frac{\Delta t}{\Delta x} & , & a_N = a_S = A_y \frac{\Delta t}{\Delta y} & , & a_F = a_B = A_z \frac{\Delta t}{\Delta z}, \\ a_P = \sum a_{NP}, \\ b = \rho [A_x (\tilde{u}_e^* - \tilde{u}_w^*) + A_y (\tilde{u}_n^* - \tilde{u}_s^*) + A_z (\tilde{u}_f^* - \tilde{u}_b^*)], \end{cases} \quad (3.7)$$

where A_i indicates the face area normal to the direction i . To implement the pressure-correction method, the face velocity at the intermediate step, e.g. \tilde{u}_e^* , is estimated as follows:

$$\tilde{u}_e^* = \frac{\tilde{u}_P^* + \tilde{u}_E^*}{2} - \frac{\Delta t}{\rho \Delta x_e} (p_E - p_P). \quad (3.8)$$

The solution of pressure-correction field obtained from Eq. 3.6 is employed to update the pressure components at nodes,

$$p^{(n+1)} = p^n + p', \quad (3.9)$$

which is used to calculate the new velocity in the second step of the fractional step method as expressed in Eq. 3.2.

3.1.2 Numerical Solver and Convergence Criteria

The discrete equation given in Eq. 3.6 can be solved to obtain p'_P . Note that the pressure-correction at the center node p'_P is estimated based on information at the neighboring nodes, while each neighbor is also dependent on its neighboring nodes. There are different methods

to solve the discrete equation, especially when the field is multi-dimensional. In this case, an alternating direction implicit (ADI) solver based on the tri-diagonal matrix algorithm (TDMA) is used to solve the pressure-correction equations. The direct solver is applied in only one direction, and it needs to be repeated to obtain the final solution.

The main computational task in CFD relates to solving the pressure-correction field. The elliptic characteristic of the pressure-correction equation increases the challenge of solving the pressure field in large flow domains. Multigrid solvers have been developed to accelerate the convergence process by smoothing out the errors of wavelengths at different frequencies using a hierarchy of grid levels (Stüben and Trottenberg, 1982). There are forms of multigrid solvers with different grid levels and iterations. In this study, a multigrid solver with four grid levels and a control strategy to move the solution to an appropriate grid level is implemented to achieve robust and fast convergence. Full details of this pressure solver are provided in Yin (2008).

To examine convergence, the residual of the pressure-correction equation “ r ” at each node is calculated for all grid points. The sum of the residuals for all grid points is obtained as follows to monitor the convergence:

$$R = \sum |r_j| \quad \text{where} \quad r_j = \sum a_{\text{NP}} p'_{\text{NP}} + b - a_{\text{P}} p'_{\text{P}}. \quad (3.10)$$

The conventional method is to compare the difference between the new residual R_i and the old residual R_{i-1} (from the previous iteration) for convergence. If the difference is less than a small fraction α of the old residual, the convergence is satisfied,

$$\frac{|R_i - R_{i-1}|}{|R_{i-1}|} \leq \alpha. \quad (3.11)$$

However, using Eq. 3.11 does not necessarily guarantee convergence. Hence, the new residual is compared with an initial residual R_o , which is obtained at the beginning of the iteration process, i.e.,

$$\left| \frac{R_i}{R_o} \right| \leq \alpha. \quad (3.12)$$

3.2 Discretization of the First Cell in the LES Domain

The first issue in wall-modeling is how the wall shear stress is introduced to the LES as a boundary condition. To clarify this issue, consider the discrete filtered NSE for the first cell off the wall,

$$\frac{\partial \tilde{u}}{\partial t} + \frac{\partial}{\partial x_j}(\tilde{u}_i \tilde{u}_j) = -\frac{\partial p}{\partial x_i} + \frac{\partial}{\partial x_j} \left(\nu \frac{\partial \tilde{u}_i}{\partial x_j} \right) + \frac{\partial \tau_{ij}^*}{\partial x_j}. \quad (3.13)$$

To simplify the explanation, all terms except the diffusion are represented by \mathcal{G}_{ij} as follows:

$$\mathcal{G}_{ij} + \frac{\partial}{\partial x_j} \left(\nu \frac{\partial \tilde{u}_i}{\partial x_j} \right) = 0 \quad \text{where} \quad \mathcal{G}_{ij} = \frac{\partial \tilde{u}}{\partial t} + \frac{\partial}{\partial x_j}(\tilde{u}_i \tilde{u}_j) + \frac{\partial p}{\partial x_i} + \frac{\partial \tau_{ij}}{\partial x_j}. \quad (3.14)$$

For the control volume shown in Fig. 3.2, Eq. 3.14 is integrated in the wall-normal direction as

$$\int_t^{t+\Delta t} \int_s^n \left(\mathcal{G}_{ij} + \frac{\partial}{\partial x_j} \left(\nu \frac{\partial \tilde{u}_i}{\partial x_j} \right) \right) dy dt = \left[\mathcal{G}_n - \mathcal{G}_s + \nu_n \frac{\partial \tilde{u}_i}{\partial y} \Big|_n - \underbrace{\nu_s \frac{\partial \tilde{u}_i}{\partial y} \Big|_s}_{\tau_{w,i}/\rho} \right] \Delta t, \quad (3.15)$$

where $\tau_{w,i}$ is the wall shear stress in the i -direction. The discrete form of Eq. 3.15 represents a discrete Poisson equation written as

$$a_P \tilde{u}_P = \sum a_{NP} \tilde{u}_{NP} + \underbrace{b_o - \tau_{w,i} \Delta t / \rho}_b. \quad (3.16)$$

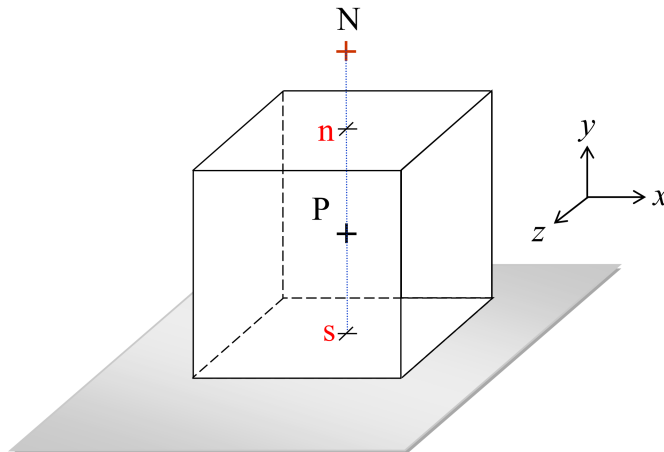


Figure 3.2: First cell off the wall in LES.

This formulation is used in the x - and z - directions, while a conventional discretization is employed in the wall-normal (y) direction with a no penetration boundary condition at the south face.

3.3 Wall Layer Modeling

The dynamic non-equilibrium wall model proposed by Park and Moin (2014) is implemented in an embedded near-wall mesh as shown in Fig. 3.3 to resolve the wall layer. The model is based on the unsteady three-dimensional Reynolds-Averaged Navier-Stokes equations. A dynamic eddy viscosity model is employed to complement the resolved Reynolds stresses in the prediction of an accurate wall shear stress. The governing equations for the momentum transport are based on the two-dimensional boundary layer equations proposed by Balaras and Benocci (1994) as given in Eq. 2.7. The wall layer is assumed to be thin enough that the pressure gradient across the wall layer is negligible, and the thin boundary layer behaves analogous to a Couette flow driven by the outer flow. Balaras et al. (1996) later improved this method by introducing convection in the streamwise direction. Since the pressure field is enforced by the outer flow, a different approach should be used for the conservation of mass. Consequently, the momentum equations are only solved in the streamwise and spanwise directions, and the continuity equation is implemented to estimate the wall-normal velocity and conserve mass in the wall layer. The discretization of the governing equations will be described in the following section.

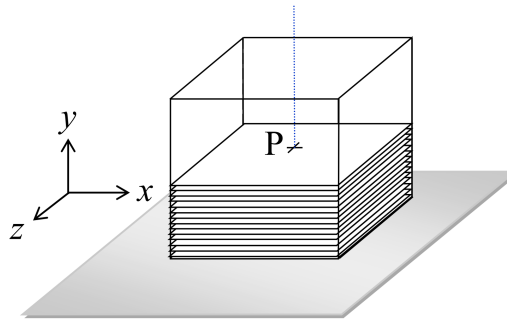


Figure 3.3: A schematic of a three-dimensional embedded mesh in the first cell of the LES domain.

3.3.1 Discrete Form of the Thin Boundary Layer Equations

To discretize the TBLEs in a three-dimensional wall layer, a simple form of Eq. 2.8 for the control volume shown in Fig. 3.4 is adopted in the streamwise direction,

$$\frac{\partial \bar{u}}{\partial t} + \bar{U}_f \frac{\partial \bar{u}}{\partial x} + \bar{V}_f \frac{\partial \bar{u}}{\partial y} = -\frac{1}{\rho} \frac{\partial p}{\partial x} + \frac{\partial}{\partial y} \left[(\nu + \nu_t) \frac{\partial \bar{u}}{\partial y} \right], \quad (3.17)$$

where \bar{U}_f and \bar{V}_f are the face velocities in the streamwise and wall-normal directions, respectively. An overbar indicates the parameter is time-averaged, which will be discussed further in Section 3.3.3. A second-order central-difference scheme is used for space integration, and a backward Euler method is used for time integration. The discrete form of each term in Eq. 3.17 is given as follows:

$$\begin{aligned} \left. \frac{\partial \bar{u}}{\partial t} \right|_o^1 &= \frac{\bar{u}_P^1 - \bar{u}_P^o}{\delta t}, \\ \bar{U}_f \left. \frac{\partial \bar{u}}{\partial x} \right|_w^e &= \frac{\bar{U}_{f,e} \bar{u}_e - \bar{U}_{f,w} \bar{u}_w}{\delta x}, \quad \bar{u}_e = \frac{\bar{u}_E + \bar{u}_P}{2}, \quad \bar{u}_w = \frac{\bar{u}_W + \bar{u}_P}{2} \\ &= \bar{U}_{f,e} \frac{\bar{u}_E + \bar{u}_P}{2\delta x} - \bar{U}_{f,w} \frac{\bar{u}_W + \bar{u}_P}{2\delta x}, \\ \bar{V}_f \left. \frac{\partial \bar{u}}{\partial y} \right|_s^n &= \bar{V}_{f,n} \frac{\bar{u}_N + \bar{u}_P}{2\delta y} - \bar{V}_{f,s} \frac{\bar{u}_S + \bar{u}_P}{2\delta y}, \\ -\frac{1}{\rho} \left. \frac{\partial p}{\partial x} \right|_w^e &= \frac{1}{\rho} \frac{p_e - p_w}{\delta x} \\ &= \frac{p_E - p_W}{2\rho\delta x}, \\ \frac{\partial}{\partial y} \left[(\nu + \nu_t) \frac{\partial \bar{u}}{\partial y} \right]_s^n &= (\nu + \nu_t) \left. \frac{\partial \bar{u}}{\partial y} \right|_n - (\nu + \nu_t) \left. \frac{\partial \bar{u}}{\partial y} \right|_s \\ &= \left[(\nu + \nu_t)_n \frac{\bar{u}_N - \bar{u}_P}{\delta y_n} - (\nu + \nu_t)_s \frac{\bar{u}_P - \bar{u}_S}{\delta y_s} \right]. \end{aligned} \quad (3.18)$$

Inserting the discretized terms in Eq. 3.18 into Eq. 3.17 and arranging the TBLE in neighboring groups,

$$a_P \bar{u}_P = \sum a_{NP} \bar{u}_{NP} + b, \quad (3.19)$$

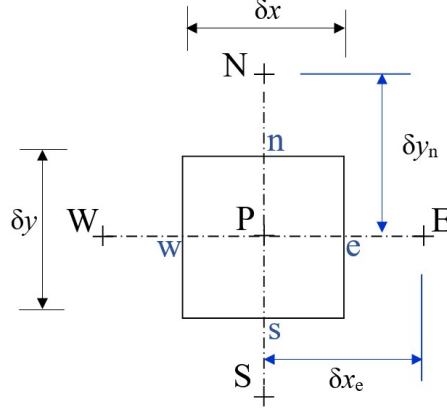


Figure 3.4: A schematic of the control volume used in the wall-modeling.

where the coefficients are as follows:

$$\begin{aligned}
 a_E &= -\frac{1}{2}\bar{U}_{f,e}A_x \quad , \quad a_W = \frac{1}{2}\bar{U}_{f,w}A_x, \\
 a_N &= -\frac{1}{2}\bar{U}_{f,n}A_y + (\nu + \nu_t)_n \frac{A_y}{\delta y_n} \quad , \quad a_S = \frac{1}{2}\bar{U}_{f,s}A_y + (\nu + \nu_t)_s \frac{A_y}{\delta y_s}, \\
 a_P &= \frac{\delta V}{\delta t} + \frac{1}{2}\bar{U}_{f,e}A_x - \frac{1}{2}\bar{U}_{f,w}A_x + \frac{1}{2}\bar{U}_{f,n}A_y - \frac{1}{2}\bar{U}_{f,s}A_y + \frac{(\nu + \nu_t)_n}{\delta y_n}A_y + \frac{(\nu + \nu_t)_s}{\delta y_s}A_y \\
 b_P &= -\frac{A_x}{2\rho}[p_E - p_W] + \frac{\delta V}{\delta t}\bar{u}_P^o,
 \end{aligned} \tag{3.20}$$

where δV is the volume of the cell, and \bar{u}_P^o indicates the old velocity. The same procedure is implemented to solve the wall layer in the spanwise direction. Given the streamwise and spanwise velocity components, the continuity equation is discretized and solved to obtain the wall-normal velocity, i.e.,

$$\frac{\bar{u}_w - \bar{u}_e}{\delta x} + \frac{\bar{v}_s - \bar{v}_n}{\delta y} + \frac{\bar{w}_b - \bar{w}_f}{\delta z} = 0, \tag{3.21}$$

where \bar{v}_s and \bar{v}_n are unknown. To calculate the wall-normal velocities, Eq. 3.21 must be solved from the wall to the top of the wall layer, assuming $\bar{v}_s = 0$ for the first cell due to the impermeability of the wall. Given the face velocities, a linear interpolation is used to approximate the wall-normal velocity at the node.

3.3.2 Dynamic Eddy Viscosity

The eddy viscosity model used in the wall-modeling is a zero-equation eddy viscosity model based on Prandtl's mixing length hypothesis:

$$\nu_t = (\kappa y)^2 |S| \mathcal{D}, \quad (3.22)$$

where $|S|$ is the magnitude of the rate-of-strain tensor defined as $|S| = \sqrt{2\overline{S_{ij}}\overline{S_{ij}}}$. The van Driest wall-damping function is given by $\mathcal{D} = [1 - \exp(-y^+/A^+)]^2$ with $A^+ = 26$. The eddy viscosity must be lower than its typical RANS value in Eq. 3.22 due to the contribution of the resolved Reynolds stresses in the convection term as suggested by Wang and Moin (2002) and Park and Moin (2014). This implies that conventional RANS models the entire Reynolds stress, whereas a fraction of the Reynolds stress is resolved in the outer layer and imposed to the wall layer. Hence, the dynamic eddy viscosity model should only account for the unresolved part of the Reynolds stresses. To achieve this, the eddy viscosity obtained from the conventional RANS with the conventional value should equate to the sum of the resolved and modeled Reynolds stresses in the wall layer (Park and Moin, 2014), i.e.,

$$2\nu_t \overline{S_{ij}} - \frac{2}{3}k\delta_{ij} - \overline{R_{ij}} \approx 2\nu_t^* \overline{S_{ij}} - \frac{2}{3}k^*\delta_{ij}, \quad (3.23)$$

where ν_t^* represents the modeled eddy viscosity obtained from Eq. 3.22 with the conventional value, i.e. $\kappa = 0.41$. The turbulence kinetic energy (k and k^*) on both sides of Eq. 3.23 should balance if they are modeled precisely. $\overline{R_{ij}}$ is the resolved Reynolds stresses in the wall layer given by $\overline{R_{ij}} = -\overline{u'_i u'_j}$. The strain rate is $\overline{S_{ij}} = \frac{1}{2}(\overline{u_{i,j}} + \overline{u_{j,i}})$.

To approximate ν_t , a least-square minimization is implemented as follows:

$$\epsilon_{ij} = 2(\nu_t - \nu_t^*)\overline{S_{ij}} - \frac{2}{3}(k - k^*)\delta_{ij} - \overline{R_{ij}} \quad , \quad \epsilon \equiv \epsilon_{ij}\epsilon_{ij}, \quad (3.24)$$

and applying $\partial\epsilon/\partial\nu_t = 0$, the wall-modeled eddy viscosity is determined to be

$$\nu_t = \nu_t^* + \frac{\overline{R_{ij}}\overline{S_{ij}}}{2\overline{S_{ij}}\overline{S_{ij}}}. \quad (3.25)$$

Given $\nu_t = (\kappa_{\text{wm}} y)^2 |S| \mathcal{D}$ and $\nu_t^* = (\kappa y)^2 |S| \mathcal{D}$, the dynamic eddy viscosity of Eq. 3.25 can be expressed using the von Karman constant as follows:

$$\kappa_{\text{wm}}^2 = \kappa^2 + \frac{\overline{R_{ij}}\overline{S_{ij}}}{2\overline{S_{ij}}\overline{S_{ij}}} \frac{1}{y^2 |S| \mathcal{D}}. \quad (3.26)$$

Substituting the dynamic von Karman constant into Eq. 3.22, the eddy viscosity of the non-equilibrium wall model is obtained.

3.3.3 Time Averaging and Temporal Filtering

Another topic that should be addressed in the wall-modeling is the period of time used for averaging the flow field. Wall functions and equilibrium wall-models implement a Time Averaging scheme over the entire simulation period (Schumann, 1975; Cabot and Moin, 2000). The full RANS equations are applied to resolve the wall layer in some non-equilibrium wall-models (Kawai and Larsson, 2013). Taking the average over too long a time period makes the wall model unresponsive to the essential stress-carrying flow structures in the outer layer. Other wall-models apply a Time Averaging scheme on the TBLE to resolve the flow in the near-wall region (Cabot and Moin, 2000; Wang and Moin, 2002). The time-averaged approach implemented in this study uses a predefined time period. Flow properties in the wall layer are averaged over a certain number of (previous) time steps to provide a more realistic instantaneous wall shear stress to the outer flow. However, choosing the number of time steps for Time Averaging is a challenge.

Since the wall layer is resolved using a form of the unsteady RANS (URANS) equations, a Time Averaging operator is required to average the flow parameters. An exponentially weighted-averaging function, which ensures that the flow parameters at recent times are more significant than older values, is defined as follows (Xiao and Jenny, 2012):

$$\bar{\phi}(t) = \frac{1}{T_{av}} \int_{-\infty}^t \phi(\tau) e^{-\delta t/T_{av}} d\tau, \quad (3.27)$$

where t and τ are the current and previous times, respectively, T_{av} is the characteristic averaging time scale, and δt is the computational time step. Using a first-order approximation and Leibniz's rule for differentiation under an integral, Eq. 3.27 can be simplified into a linear correlation (Tunstall et al., 2017). As such, a combination of weighted terms based on the previous time-averaged value and the new value is implemented to estimate the time-averaged parameter in the current time and reduce the memory load (Meneveau et al., 1996):

$$\bar{\phi}^{n+1} = \varepsilon_{av} \phi^{n+1} + (1 - \varepsilon_{av}) \bar{\phi}^n, \quad \varepsilon_{av} = \frac{\delta t/T_{av}}{1 + \delta t/T_{av}}, \quad (3.28)$$

where $\bar{\phi}^n$ is the time-averaged parameter from the previous time step, and ϕ^{n+1} is the new value. The characteristic averaging time scale T_{av} is comparable to the convective time scale

taken as a ratio of the channel height to the velocity at the center of the channel. The Time Averaging scheme using this strategy ensures a wall model that can respond to the instantaneous flow structures in the LES.

The wall layer is coupled to the instantaneous velocity and pressure fields in the LES at its upper boundary. These flow parameters can fluctuate at high-frequencies and with short wavelengths. The input of high-frequency fluctuations to the wall layer can lead to an over-prediction or under-prediction of the skin friction that manifests in the mean velocity field as the log-layer mismatch (Larsson et al., 2016). The input data into the wall layer should correspond to the time scale of the wall layer since the wall model is implemented in an URANS framework. One solution to mitigate this mismatch is using a Temporal Filtering for the input flow data at the matching point over a particular time period to provide the low-frequency fluctuations in the LES (Yang et al., 2015, 2017). Eliminating the high-frequency unsteadiness reduces the log-layer mismatch. Hence, the top boundary of the wall layer becomes more compatible with the wall-model's averaging time scale. A similar exponentially weighted operator is employed to filter the velocity and pressure parameters in the LES at the matching point (Yang et al., 2015),

$$\hat{\phi}(t) = \varepsilon_{\text{fl}} \phi(t) + (1 - \varepsilon_{\text{fl}}) \hat{\phi}(t - \delta t) \quad , \quad \varepsilon_{\text{fl}} = \frac{\delta t}{T_{\text{fl}}}, \quad (3.29)$$

where the hat symbol represents a temporal-filtered parameter. In contrast to the Time Averaging, the characteristic time scale T_{fl} used in Temporal Filtering is defined based on the turbulent diffusion time scale across the wall layer.

Throughout this dissertation, turbulent channel flows and turbulent boundary layers use the numerical methodology discussed in this chapter to resolve the flow dynamics in the LES domain. The subgrid scale flow structures are modeled using the dynamic non-linear model (DNM), which is explained in Appendix A.3. In the WMLES test problems, the wall layer is modeled using the dynamic non-equilibrium wall model discussed in Section 3.3.

Chapter 4

Large Eddy Simulation of Channel Flows at Moderate and High Reynolds Numbers

Fully developed turbulent channel flows are widely implemented in the investigation of wall-bounded turbulent flows due to their simple geometries, which makes them a classic benchmark flow geometry for numerical testing and exploring the flow dynamics. The channel flow is homogeneous in the streamwise (x) and spanwise (z) directions. Hence, the mean flow field is invariant in the x - and z -directions, and the flow is statistically one-dimensional. The presence of high shear and small-scale flow dynamics in the inner layer, $\delta/y < 0.1$, led researchers to investigate relatively low Reynolds number channel flows. Deardorff (1970) implemented LES to calculate a three-dimensional turbulent channel flow and examined the characteristics of turbulence. Later, Moin and Kim (1982) studied a turbulent channel flow at a higher Reynolds number ($\text{Re}_\tau = 640$, where the Reynolds number is defined based on the friction velocity as $\text{Re}_\tau = \frac{u_\tau \delta}{\nu}$) using a fine grid. They indicated that the LES method can predict turbulent flow structures effectively, and the low- and high-speed streaks are dominant characteristics in the wall region. Use of the channel flow geometry is not limited to these studies, and there are numerous works that have implemented a channel flow to conduct their research objectives.

The present research considers an incompressible turbulent channel flow at Reynolds numbers ranging from $\text{Re}_\tau = 395$ to $\text{Re}_\tau = 2000$ to investigate the performance of LES and wall-modeling. First, the wall-resolved LES (WRLES) channel flow is studied at a moder-

ate Reynolds number, and the results are compared to reference studies. Then, the non-equilibrium wall model is implemented for the same Reynolds number using a coarse grid to compare the computational cost. The location of the matching point is investigated in the wall-modeled channel flow at moderate-Reynolds number. The WMLES is used to examine the performance of wall-modeling at different Reynolds numbers up to $\text{Re}_\tau = 2000$. Finally, the effects of time averaging and temporal filtering schemes on the log-layer mismatch in the wall-modeling are investigated in the high Reynolds number channel flow.

4.1 Numerical Method

The computational domain for the wall-resolved and wall-modeled turbulent channel flows at different Reynolds numbers is $2\pi\delta \times 2\delta \times \frac{4}{3}\pi\delta$ in the streamwise, wall-normal, and spanwise directions, respectively as shown in Fig. 4.1, where δ is half-channel height. The flow domain size in the periodic directions is motivated by use of a pseudo-spectral method in another study to provide the best possible resolution to capture high wavenumber components (Moin and Kim, 1982). No-slip boundary conditions are implemented at the upper and lower walls, and the flow is periodic in the streamwise and spanwise directions. In the WRLES channel flow at $\text{Re}_\tau = 395$, a mesh with 96^3 grid points was used to resolve the flow field, which has a uniform grid in the wall-parallel planes and a non-uniform distribution in the wall-normal direction. The grid resolution is presented in Table 4.1, where Δx^+ , Δy_c^+ , and Δz^+ show the grid spacing in the streamwise direction, wall-normal direction at the center of the channel, and spanwise direction, respectively, in wall coordinates. The first node near the wall is located at $y_1^+ \approx 0.87$. To begin the simulation, the initial velocities were estimated based on Spalding's mean velocity profile (Spalding, 1961) shown in Eq. 4.1 and introducing random fluctuations on the order of 5% of the local mean velocity,

$$y^+ = u^+ + 0.1108 \left[\exp(0.4u^+) - 1 - 0.4u^+ - \frac{(0.4u^+)^2}{2} - \frac{(0.4u^+)^3}{6} - \frac{(0.4u^+)^3}{24} \right]. \quad (4.1)$$

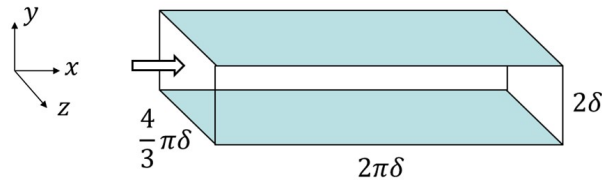


Figure 4.1: A schematic of flow domain used in the simulation of turbulent channel flows.

Table 4.1: Grid and temporal resolution of turbulent channel flows at different Reynolds numbers.

Turbulent channel flow	$n_x \times n_y \times n_z$	$\Delta x^+, \Delta y_c^+, \Delta z^+$	y_1^+	N_m	h_{wm}^+	T	δt^+
WRLES, $Re_\tau = 395$	$96 \times 96 \times 96$	26, 15, 17	0.87	-	-	3360	0.336
WMLES, $Re_\tau = 395$	$64 \times 32 \times 48$	38, 25, 34	12.0	4 th	84.5	5800	0.783
WMLES, $Re_\tau = 550$	$64 \times 32 \times 64$	54, 34, 34	17.2	4 th	117.5	7050	0.671
WMLES, $Re_\tau = 950$	$96 \times 48 \times 64$	62, 39, 62	19.8	5 th	173.2	8700	0.730
WMLES, $Re_\tau = 2000$	$96 \times 64 \times 64$	130, 62, 130	31.2	5 th	272.2	9300	1.338

N_m : Node location of the matching point in the LES domain

h_{wm}^+ : Height of the wall layer

The simulation was run for a sufficient time period for the transition from the initial random fluctuations to real turbulence. Once the flow statistics stabilized, the simulation was run for a non-dimensional time $T = t/t_v$, where t_v is the viscous time scale and is defined as $t_v = \nu/u_\tau^2$.

The WMLES channel flow at $Re_\tau = 395$ has a lower resolution, i.e. $64 \times 32 \times 48$, but with a uniform grid distribution in the wall-normal direction and the matching point located at the 4th node in the LES domain with $h_{wm}^+ \approx 84.5$ in wall coordinates. Thirty grid points in the wall-normal direction are used in the wall layer with the same grid resolution for the LES domain in the wall-parallel planes. For the other wall-modeled channel flows, the grid distribution was similar to what was used for the WMLES channel flow at $Re_\tau = 395$ but with different resolutions as shown in Table 4.1. A Courant number of $CFL = 0.3$ was used in the LES region and $CFL = 15$ in the wall-layer. The time step varies according to the Courant number, and the average time step non-dimensionalized by the viscous time scale (t_v) is $\delta t^+ = 0.783$. The wall layer statistics are averaged over the convective time scale given by $T_{av} = \delta/u_c$, where u_c is the mean velocity at the center of the channel. The filtering time scale is determined as a fraction of $T_\Pi = h_{wm}/\kappa u_\tau$, where h_{wm} is the height of the wall layer.

4.2 Wall-resolved LES Channel Flow at $Re_\tau = 395$

The first set of results pertains to a wall-resolved fully developed channel flow at a moderate-Reynolds number of $Re_\tau = 395$. Both the dynamic Smagorinsky model (DSM) and the dynamic nonlinear SGS model (DNM) are implemented to calculate the effects of the unfiltered flow dynamics. Fig. 4.2a shows the mean velocity profiles in wall coordinates compared with the DNS study of Moser et al. (1999). The DSM shows a deviation in the outer layer

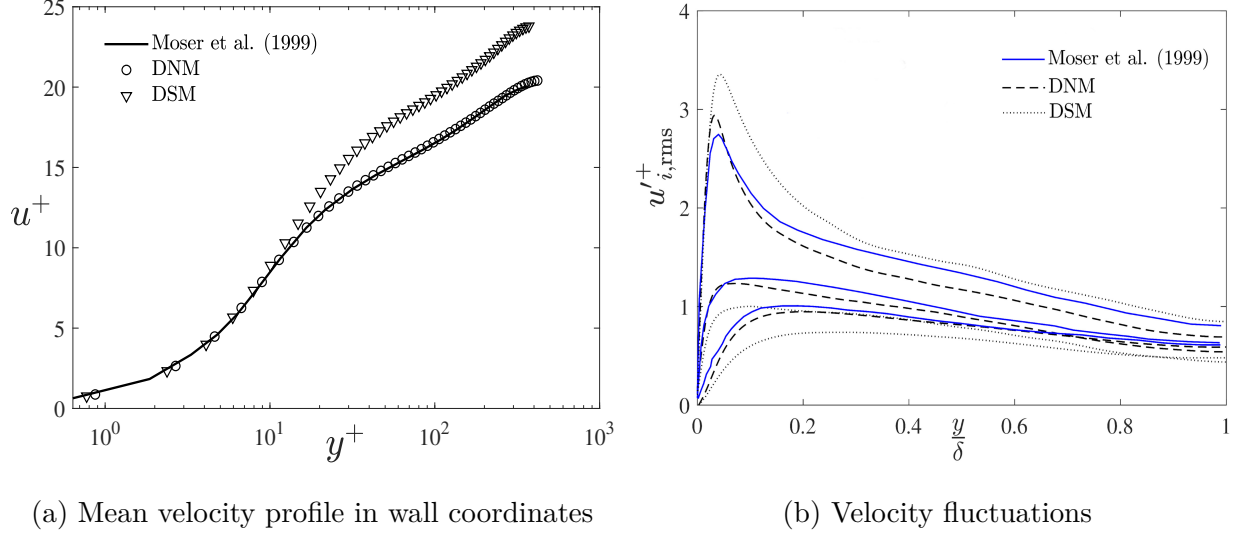


Figure 4.2: (a) The mean velocity profile and (b) *rms* of velocity fluctuations (bottom to top: v'_{rms}^+ , w'_{rms}^+ , u'_{rms}^+) in a wall-resolved channel flow at $Re_\tau = 395$ using the DSM and DNM.

while improved performance is observed for the DNM. Both simulations used a single computational domain with similar grid resolution. A better prediction is also observed for the root mean square (*rms*) of velocity fluctuations using the DNM as shown in Fig 4.2b. In general, the DNM effectively calculates the velocity fluctuation, especially in the near-wall region. However, the results of the DSM show noticeable discrepancies for all velocity fluctuations.

To further investigate the performance of the DSM and DNM, contours of the instantaneous resolved and SGS dissipation in a vertical plane across the channel are presented in Fig. 4.3. The rate of resolved viscous dissipation ε_r and the SGS dissipation ε_{SGS} of the turbulence kinetic energy are defined as,

$$\varepsilon_r = 2\nu\tilde{S}_{ij}\tilde{S}_{ij} \quad , \quad \varepsilon_{SGS} = -\tau_{ij}^*\tilde{S}_{ij}. \quad (4.2)$$

The top section of Fig. 4.3a corresponds to the resolved dissipation using the DSM whereas the resolved dissipation of the DNM is shown below. The peak of the resolved dissipation, which occurs at the filtered scale, is mainly attributed to the local velocity gradients in the wall region. It is clear that the LES using DNM captures more details of the flow structures in comparison with the DSM. This behavior is also observed in Fig. 4.3b where the SGS dissipation of turbulence kinetic energy is presented. It can be concluded that the performance of the SGS model used to estimate the SGS dissipation affects the flow structures. The over-prediction of the mean velocity profile presented in Fig. 4.2a and under-prediction of the velocity fluctuations shown in Fig. 4.2b using the DSM indicate a deficiency

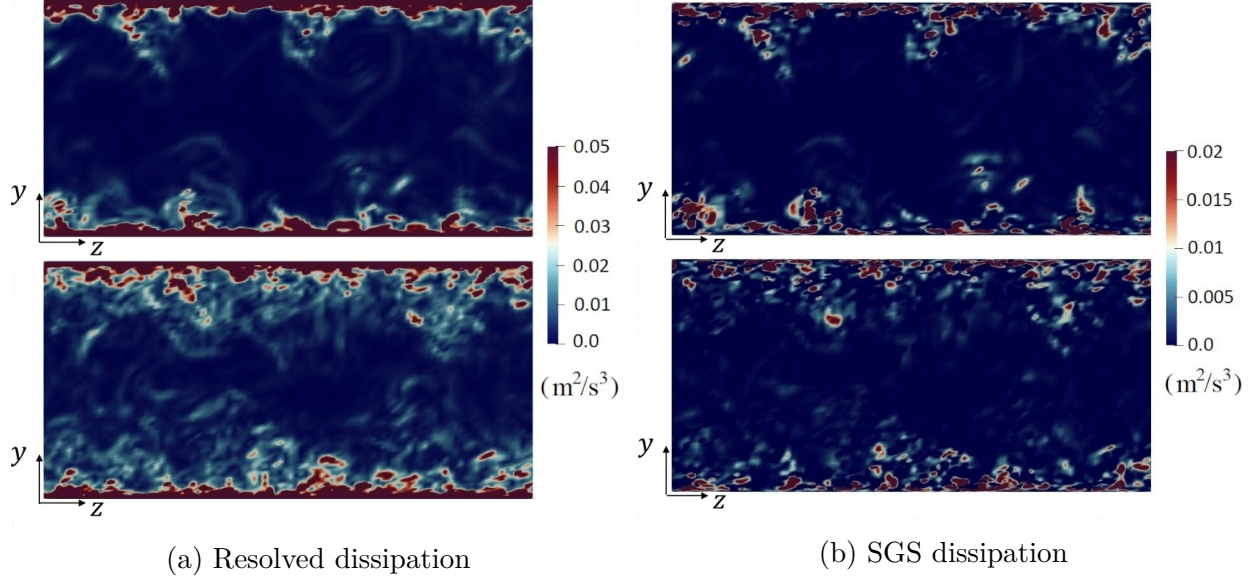


Figure 4.3: The rate of dissipation of turbulence kinetic energy ε in a vertical plane perpendicular to the flow stream, the DSM at the top and the DNM on the bottom.

in the DSM. Moreover, the time-averaged rate of the resolved and SGS turbulent kinetic energy dissipation indicates similar behavior as shown in Fig. 4.4. The resolved dissipation reaches a plateau when moving towards the wall. On the other hand, the SGS dissipation decreases when moving towards the wall due to the grid resolution used in the WRLES channel flow that is similar to the grid resolution used in the DNS. Hereafter, all simulations

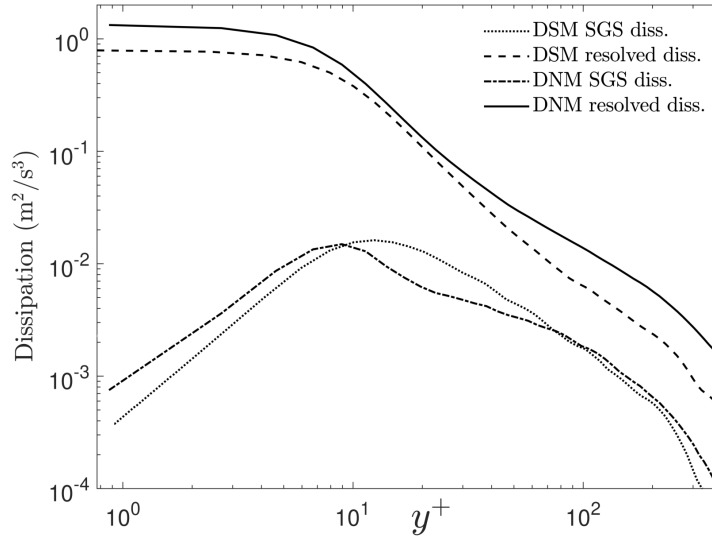


Figure 4.4: Profile of the resolved and SGS dissipation in the wall-resolved channel flow.

throughout this research implement the DNM approach for modeling the SGS motions.

4.3 Wall-modeled LES Channel Flow at $\text{Re}_\tau = 395$

The dynamic non-equilibrium wall model discussed in Section 3.3.2 is implemented to model the flow dynamics in the wall layer and transmit the wall shear stress to the LES domain. In the first simulation, the wall-modeling is performed for the same Reynolds number of the wall-resolved channel flow at $\text{Re}_\tau = 395$. Then, the results of WMLES channel flow are compared with the WRLES, although wall-modeling is intended for simulation of high-Reynolds number flows. The location of the matching point between the wall layer and the LES domain is carefully examined. Recall that the wall layer is embedded in the LES domain as shown in Fig. 4.5a. It extends from the wall to meet the LES domain at the matching point as shown in Fig 4.5b. At the matching plane, the velocities and pressure are set as Dirichlet conditions for the wall layer, and the wall shear stress returns to the LES as a boundary condition.

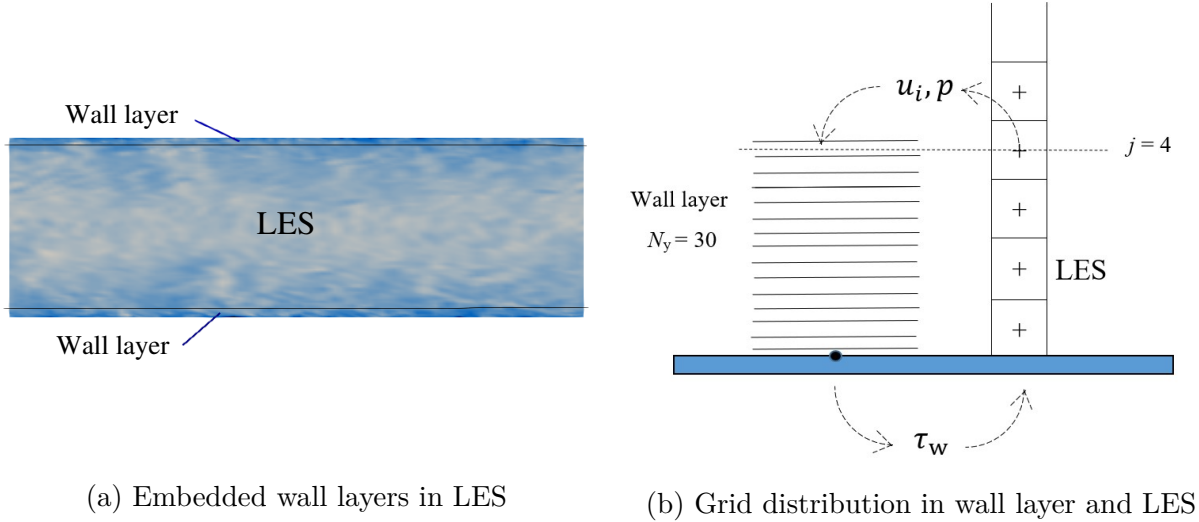


Figure 4.5: Interaction between the wall layer and LES domain in a side view of the channel flow; (a) the extent of the wall layer on the vertical symmetry plane showing streamwise velocity contours, and (b) a schematic of wall-modeling grid embedded in the LES domain.

One issue often encountered in WMLES is the log-layer mismatch which is the consequence of errors associated with either the wall model or the LES at the first grid point off the wall (Kawai and Larsson, 2013). Regardless of the accuracy of the wall-model, using LES at the first grid cell near the wall is associated with errors since the filter width is larger than

the energy-containing motions in the wall region (Nicoud et al., 2001). The performance of LES at the first grid point is inevitably affected by neglecting these stress-carrying motions. Consequently, the prediction of the wall model is inaccurate, which leads to a mismatch between the mean velocity profile and the logarithmic law. This mismatch can be either negative for wall stress models using a staggered grid for incompressible flows or positive for wall stress models with a collocated grid or hybrid RANS/LES approach. This shows that the mismatch is also dependent on the numerical method applied in the code and the modeling in LES. Studies have found that locating the matching point between the top of the viscous layer ($y^+ > 50$) and the outer layer ($y/\delta < 0.2$) better predicts the effects of the solid surface (Kawai and Larsson, 2012). In high Reynolds number flows, the efficacy of the SGS model deteriorates significantly on a coarse mesh (Bae et al., 2018). A remedy for avoiding this problem is to locate the matching point far away from the wall where the requirements of the SGS model are satisfied by the grid resolution. Hence, the matching point for the WMLES channel flow is located at the 4th cell away from the wall to locate the height of the wall layer at $h_{\text{wm}}^+ = 84.5$. Time and grid resolutions were presented in Table. 4.1.

Fig. 4.6 presents the mean velocity profiles obtained by the WMLES in a fully developed channel flow both in wall coordinates and outer coordinates. The results are compared with the results of the WRLES test case. The over-prediction of the mean velocity profile is clearly observed in Fig. 4.6a for the grid points below the matching point. The coarse grid near the

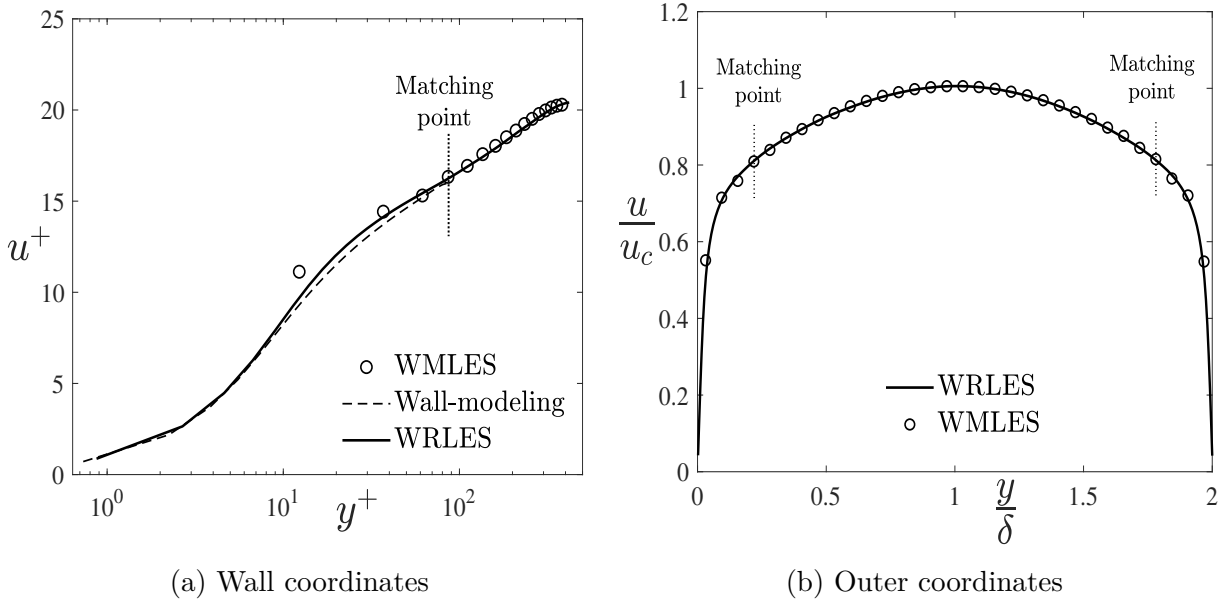


Figure 4.6: Mean velocity profiles in the WMLES channel flow at $Re_\tau = 395$ in different coordinates.

wall is inconsistent with the requirements of the SGS model, which eventually results in the over-prediction of mean velocities for grid points below the matching point. Above the matching point, the mean velocity profile matches the WRLES profile. Fig. 4.6b reconfirms the acceptable performance of the WMLES in the outer layer above the matching point, i.e. the 4th node. The promising point for using wall-modeling is revealed when the CPU-hours of computing the WMLES and WRLES test problems are compared. Both simulations were performed in a single core of Intel Xeon E5-1620 3.7 GHz with 32 GB of RAM. However, the WMLES test case required 7 CPU-hours in contrast to 141 CPU-hours spent for the WRLES test case. Furthermore, the computational memory size for the WMLES is 9 times smaller than what is needed for the WRLES, when the number of grid points provided in Table 4.1 are compared.

The resolved velocity fluctuations obtained from the WMLES channel flow are documented in Fig. 4.7a. The normalized *rms* of the velocity fluctuations are compared with the results of the WRLES test problem at the same Reynolds number. Again, the inconsistency between the grid resolution and the SGS model results in over-prediction of the velocity fluctuations in the wall layer. The distribution of the Reynolds shear stress across the channel is shown in Fig. 4.7b for both the WMLES and WRLES channel flows normalized by the total shear stress τ_{tot} . The prediction of the WMLES matches the τ_{tot}/τ_w curve for grid points above the matching point. However, at the first nodes near the wall the WMLES is unable to accurately predict the Reynolds shear stress.

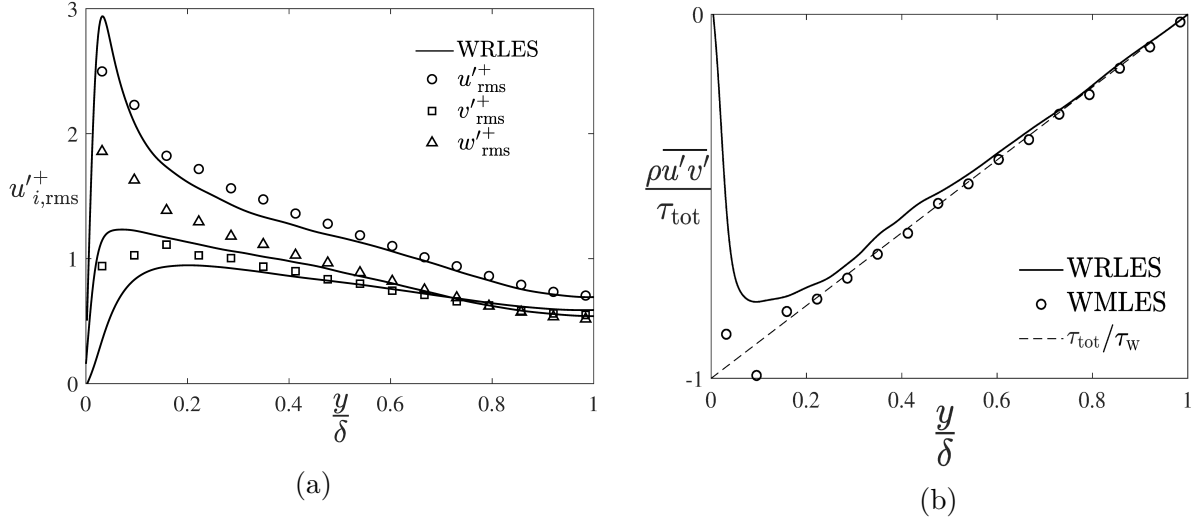


Figure 4.7: Velocity fluctuations and Reynolds shear stress for the WMLES channel flow at $Re_\tau = 395$: (a) *rms* of velocity fluctuations, bottom to top: v'_{rms} , w'_{rms} , u'_{rms} , symbols; WMLES, solid line; WRLES (b) shear stress.

The location of the matching point affects the log-layer mismatch as discussed earlier. Hence, different locations for the matching point are studied for the channel flow. Fig. 4.8 shows the mean velocity profiles of the WMLES channel flow when the matching point moves from the first node at the wall to the 4th node. In all cases, 30 grid points are used to resolve the wall layer. The profiles are shifted by five units upward for clarity. It is obvious that moving the matching point to higher nodes results in a better prediction of the wall shear stress. The matching points at the first and second nodes over-predict the wall shear stress while moving the matching point to the third and fourth nodes leads to a better prediction. This issue will be further investigated in Section 4.5.5 for a high Reynolds number channel flow.

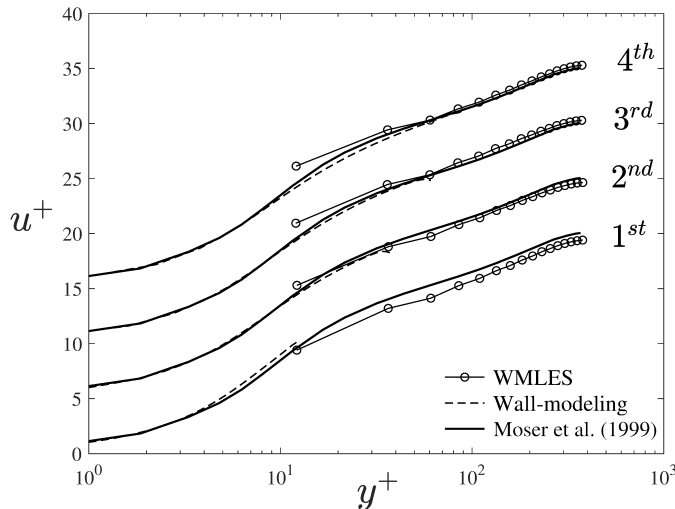


Figure 4.8: The mean velocity profiles for a wall-modeled channel flow at $Re_\tau = 395$ using different locations for the matching point.

4.4 Effects of Reynolds Number in Wall-modeling

The performance of wall-modeling is more reliable at high Reynolds numbers since the wall model represents the averaged effects of the near-wall eddies on the outer layer (Piomelli and Balaras, 2002). The coarse grid near the wall should contain a large sample of near-wall eddies to enable a RANS approach. Increasing the Reynolds number implies that the number of small eddies in the wall layer increases, which permits the application of wall-modeling. Hence, the Reynolds number is increased up to $Re_\tau = 2000$. Fig. 4.9 shows the mean velocity profiles of the WMLES channel flow for moderate to high Reynolds numbers. The matching

point is located at the 4th and 5th nodes as indicated in Table. 4.1. The velocity profiles are shifted upward five units for clarity. In general, the performance of the wall model is good for different Reynolds numbers based on comparison with the DNS results.

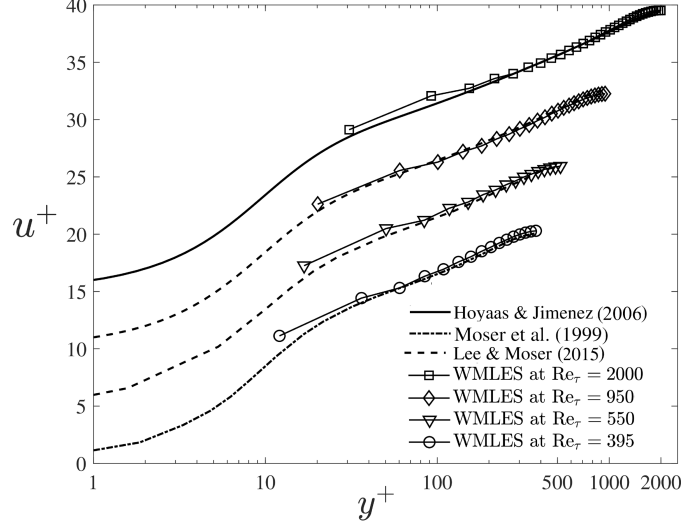


Figure 4.9: The prediction of the mean velocity profile at $Re_\tau = 395, 550, 950$, and 2000 in a WMLES channel flow.

Table 4.2 shows the standard deviation between the WMLES and the DNS results. It is clear that the deviation at the 1st node decreases for increasing Reynolds number. The deviation at the 2nd node shows no dependence on the Reynolds number. The error at the 2nd node is due to the error at the 1st node and the poor performance of the SGS model used in the coarse grid. Excluding the first two nodes, the mean velocity profile predicted by the WMLES has a lower deviation for the higher Reynolds numbers. In general, the performance of wall-modeling improves when moving to high Reynolds numbers as shown in the last column of Table. 4.2. The quantified comparison between the WMLES and DNS profiles indicates the discrepancy in the mean velocity profiles is low (less than 1%) over the

Table 4.2: The standard deviation between the mean velocities obtained from the WMLES channel flow and the DNS results presented in Fig. 4.9; all values are in percent.

WMLES Channel Flow	1 st node	2 nd node	Entire range excluding first two nodes
$Re_\tau = 395$	13.43	1.69	0.88
$Re_\tau = 550$	7.97	4.08	0.45
$Re_\tau = 950$	4.08	1.30	0.68
$Re_\tau = 2000$	3.49	2.32	0.39

outer regions, where is the focus of wall-modeled turbulent flows. Use of experimental data to quantitatively evaluate the prediction of wall-bounded flows increases complexity of an assessment due to experimental uncertainties associated with measurement techniques.

The velocity fluctuations at $\text{Re}_\tau = 550$ and 950 are shown in Fig. 4.10; a further investigation of the WMLES channel flow at $\text{Re}_\tau = 2000$ will be given in Section 4.5.1. The velocity fluctuations at $\text{Re}_\tau = 950$ are shifted by three units for clarity. The wall-normal velocity fluctuation (v'^+_{rms}) matches the DNS results of Lee and Moser (2015) after the peak in the wall layer, although different locations for the peak are observed. A better prediction is observed for the streamwise and spanwise velocity fluctuations in the outer layer in contrast to the predictions in the wall layer. A plausible explanation is that the governing equations in the streamwise and spanwise directions implement the wall shear stress as a boundary condition, whereas a no-slip boundary condition is used to resolve the flow domain in the wall-normal direction.

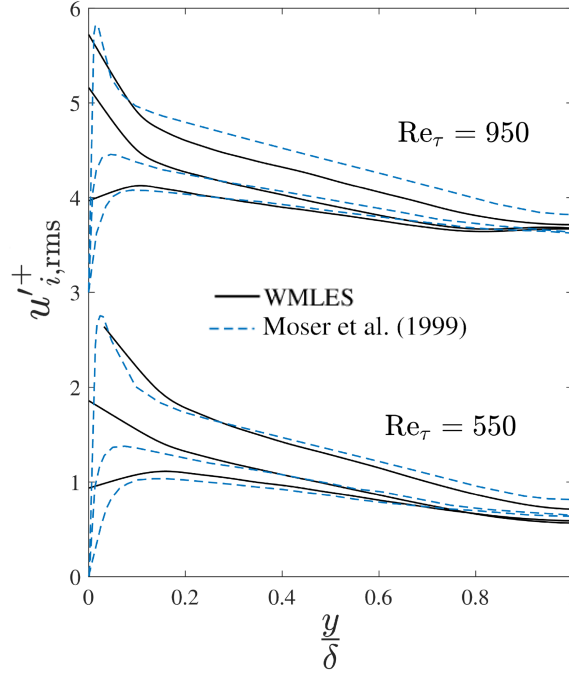


Figure 4.10: Velocity fluctuations at $\text{Re}_\tau = 550$ and 950 in the WMLES channel flows; from bottom to top: v'^+_{rms} , w'^+_{rms} , u'^+_{rms} .

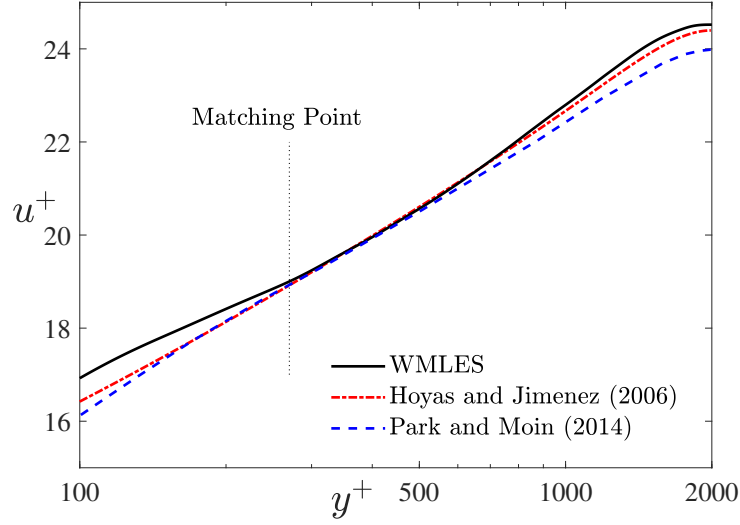
4.5 Time Averaging and Temporal Filtering in WM-LES Turbulent Channel Flows

Regardless of what wall-modeling approach is employed from those listed in Fig. 2.1, the wall-modeling potentially suffers from the log-layer mismatch (Chen et al., 2012; Larsson et al., 2016; Yang et al., 2017; Frère et al., 2017; Bae et al., 2018). This section attempts to address the mismatch issue using the dynamic wall model proposed by Park and Moin (2014) in the simulation of a turbulent channel flow at a Reynolds number of $Re_\tau = 2000$. To mitigate the log-layer mismatch, two temporal schemes are introduced to average the wall layer solution and to filter the flow information input to the wall layer as discussed in Section 3.3.3.

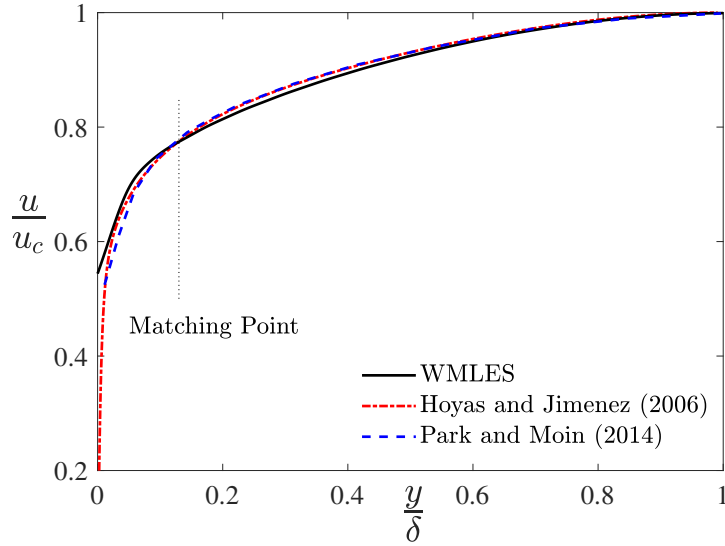
4.5.1 WMLES Channel Flow at $Re_\tau = 2000$

First, the results of a fully developed channel flow using a much shorter computational domain compared to the study of Park and Moin (2014) and with the DNM rather than the DSM are presented. The wall-modeling uses the time-averaged TBLEs (URANS), and a temporal filtering scheme recently employed by Yang et al. (2017) is also implemented. Park and Moin (2014) used a dimensionless time period of $T_W = 1.0$ to average the eddy viscosity in their study (where $T_W = T_{av} u_c / \delta$). The performance of WMLES in this research is initially investigated using a similar averaging time scale. An initial dimensionless filtering time period of $T_F = 1.0$ is employed (where $T_F = T_{fl} \kappa u_\tau / h_{wm}$), T_{fl} is the filtering time period, and $h_{wm} / \kappa u_\tau$ is the turbulent diffusion time scale. This time period was recommended to reduce the log-layer mismatch (Yang et al., 2017). Figs. 4.11 and 4.12 demonstrate the results of using the time averaging on the TBLE in the wall-modeling strategy and compares them with results taken from the literature. The mean velocity profile and *rms* of velocity fluctuations are non-dimensionalized using the friction velocity u_τ , which is obtained from the wall layer. The wall shear stress is calculated using the time-averaged velocity at the first grid point of the wall layer ($\tau_w = \mu \frac{du}{dy}$), and the friction velocity is defined by $u_\tau = \sqrt{\frac{\tau_w}{\rho}}$.

As shown in Fig. 4.11, the mean velocity profile obtained from the LES follows closely both the DNS results of Hoyas and Jiménez (2006) and the WMLES of Park and Moin (2014). The velocity profiles in both Fig. 4.11a using inner coordinates and Fig. 4.11b using outer coordinates match the reference profiles. However, an over-prediction is observed below the matching point down to the wall. According to the previous studies, this deviation relates



(a) Mean velocity profile in wall coordinates



(b) Mean velocity profile in outer coordinates

Figure 4.11: Mean velocity profiles at $\text{Re}_\tau = 2000$ with $T_W = 1.0$, $T_F = 1.0$.

to the implementation of a very coarse grid in the wall region, where the subgrid scale flow structures are not captured by the SGS model. Instead, the mean velocity profile obtained from the wall-modeling has the potential to predict the flow field below the matching point. This issue will be discussed further in the following sections. An over-prediction is observed where the results of the WMLES are compared with the results of Park and Moin (2014). Recall that the domain size implemented by Park and Moin (2014) is longer and wider than the flow domain used in this study. Abe et al. (2007), Lozano-Durán and Jiménez (2014), and Lee and Moser (2015) studied the effects of domain size in the streamwise direction for

turbulent channel flows using DNS. They found that the large-scale flow structures diminish when the size of the flow domain decreases for the same Reynolds number and grid resolution. Lozano-Durán and Jiménez (2014) showed that an over-prediction can be observed at the center of a channel using a very short domain. Note that the central region of the channel flow using the DNS has a grid resolution comparable to the grid resolution near the wall region using the WMLES. Furthermore, the shorter domain might result in introducing statistical noise to the solution and increasing the velocity variance.

The results at the center of the channel are promising. They confirm the improved performance of the DNM compared to the DSM in calculating the rate of turbulence kinetic energy transfer between the filtered and subgrid scales (Wang and Bergstrom, 2005). Due to the inconsistency of the SGS model with the grid resolution in the near-wall region, a poor prediction is obtained for the velocity fluctuations in the wall region as shown in Fig. 4.12. The prediction of the velocity fluctuations improves when moving towards the center of the channel in comparison with the results of Park and Moin (2014). The u'_{rms} profile matches the prediction of the streamwise velocity fluctuation by Park and Moin (2014), and both profiles indicate an under-prediction of u'_{rms} compared with the DNS. In contrast, the other two velocity fluctuation profiles demonstrate better predictions above the matching point, and

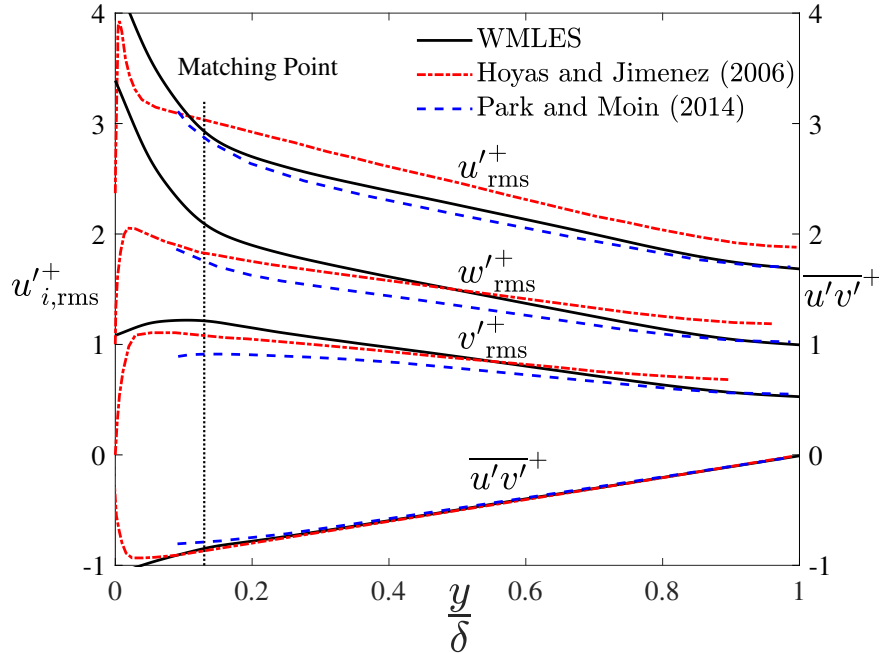


Figure 4.12: Velocity fluctuations and Reynolds shear stress profiles at $\text{Re}_\tau = 2000$ with $T_W = 1.0$, $T_F = 1.0$ (w'_{rms} and u'_{rms} profiles are shifted by +0.5 and +1.0, respectively)

smoothly reduce to match the results of Park and Moin (2014) at the center of the channel. Excellent agreement is observed between the turbulent shear stress ($\overline{u'v'}^+$) and the reference data above the matching point. In Fig. 4.12, only the v'_{rms}^+ profile decreases towards the wall whereas the u'_{rms}^+ and w'_{rms}^+ profiles indicate over-predictions below the matching point. Note that the zero-velocity boundary condition is only applied to the wall-normal velocity (v) at the wall. Overall, the results in Fig. 4.11 and 4.12 confirm the potential of the wall model. The following sections will investigate the flow characteristics in the wall layer and the effects of different time averaging and temporal filtering schemes on the performance of the wall model.

4.5.2 Eddy Viscosity in the Wall Layer

The dynamic non-equilibrium wall model of Park and Moin (2014) implements Eq. 3.25 to modify the eddy viscosity in the wall layer. As discussed in Section 3.3.2, a portion of the Reynolds stresses in the wall layer is resolved. The velocity fluctuations in the streamwise and spanwise directions (u'_{rms}^+ and w'_{rms}^+) indicate a rapid increase when moving towards the matching point, as shown in Fig. 4.13. This is due to the instantaneous velocity field input from the LES domain as the top boundary condition. However, the wall layer is governed by the time-averaged governing equations that model the velocity fluctuations. The wall-normal velocity fluctuation linearly increases across the wall layer. An explanation is that the wall layer is resolved only in the x - and z -directions using the TBLEs. Instead, the

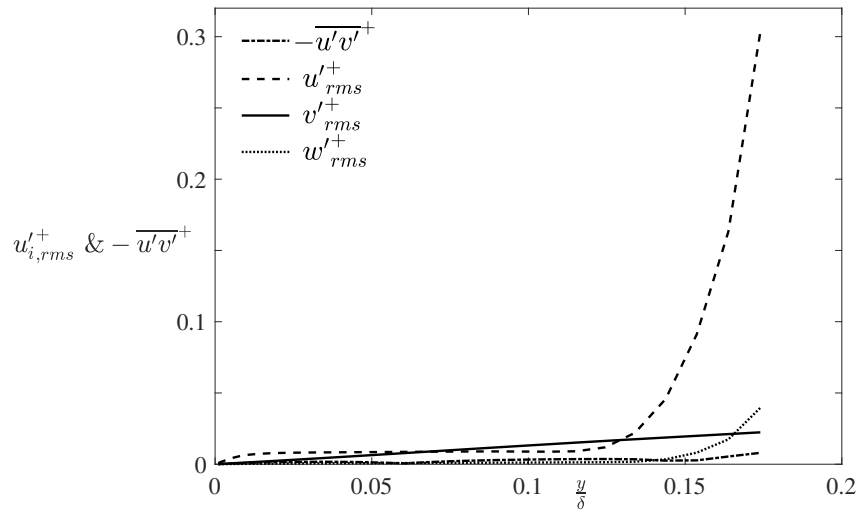


Figure 4.13: Resolved velocity fluctuations and Reynolds shear stress across the wall layer.

wall-normal velocity is estimated using the continuity equation, which consequently affects the wall-normal velocity fluctuation (v_{rms}^+). Comparing the resolved velocity fluctuations in the wall layer with the velocity fluctuations in the filtered flow field shown in Fig. 4.12 reveals that the velocity fluctuations and Reynolds shear stress in the wall layer are an order of magnitude smaller than the velocity fluctuations and Reynolds stress in the LES domain. The magnitude of the resolved velocity fluctuations and Reynolds shear stress relates to their role in modifying the eddy viscosity according to Eq. 3.25.

The modified eddy viscosity profile across the wall layer at $\text{Re}_\tau = 2000$ is presented in Fig. 4.14. The eddy viscosity obtained by Prandtl's mixing length hypothesis is also shown (Prandtl, 1925). Based on the mixing length hypothesis, the eddy viscosity is estimated by $\nu_t = \kappa u_\tau y \mathcal{D}$, where \mathcal{D} is the van Driest damping function. The eddy viscosity profile matches Prandtl's mixing length profile in the near-wall region. However, the eddy viscosity decreases as it approaches the matching point at $y^+ = 272$. The prediction of the eddy viscosity very close to the matching point indicates high fluctuations due to instantaneous flow information input from the LES domain and is removed for clarity. Recall that the wall layer experiences instantaneous velocities at the top boundary from the LES domain. Hence, the velocity fluctuations and consequently the Reynolds stresses R_{ij} increase at the interface. Based on the contribution of the second term on the right-hand side of Eq. 3.25, the eddy viscosity is modified when moving towards the matching point. This confirms the concept of the dynamic non-equilibrium wall model reducing the eddy viscosity to represent only the unresolved Reynolds stresses in the wall layer.

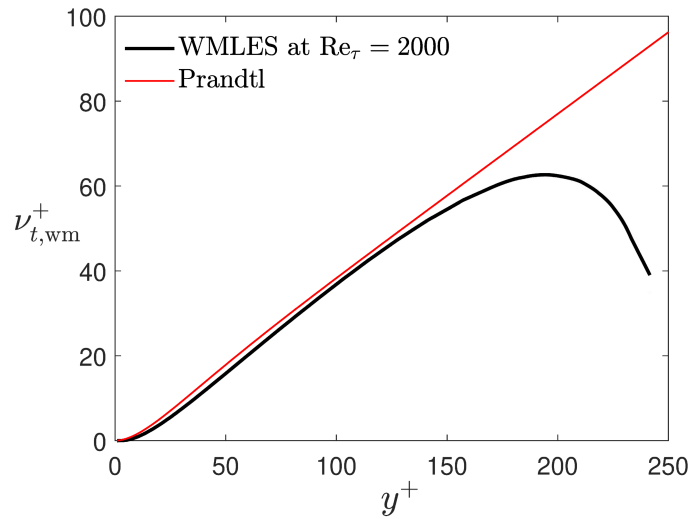


Figure 4.14: Eddy viscosity across the wall layer.

4.5.3 Temporal Filtering and Time Averaging Schemes

First, the effects of the temporal filtering scheme are studied. Based on the location of the matching point, two scenarios are introduced: Scenario A and Scenario B. The matching point is located at the first node off the wall in Scenario A, while the fifth node inside the LES domain is used for the matching point in Scenario B. The mean velocity profiles using inner coordinates for both scenarios are presented in Fig. 4.15 with $T_W = 1.0$ and $T_F = 1.0$. The case studies without temporal filtering are also presented. The instantaneous flow field from the LES is directly implemented as the top boundary condition for the wall layer in no-filtering cases. In a previous study by Yang et al. (2017), the effects of temporal filtering on the simulation of a turbulent channel flow using a wall function based on the logarithmic law were studied. They found that temporal filtering had a significant effect on the results when the matching point is located at the first node. In the present study, the non-equilibrium wall-model, which can respond to the temporal-filtered inputs from the LES domain, is implemented instead of the wall function. For clarity, vertical dotted lines are employed to highlight the location of the matching point, and the profiles in Scenario B are shifted upwards. Scenario A shows that even though the difference between the results with and without temporal filtering is small, temporal filtering reduces the mismatch. In contrast, there is no significant difference between the two cases in Scenario B, indicating that when the matching point is sufficiently far from the wall, temporal filtering is ineffective

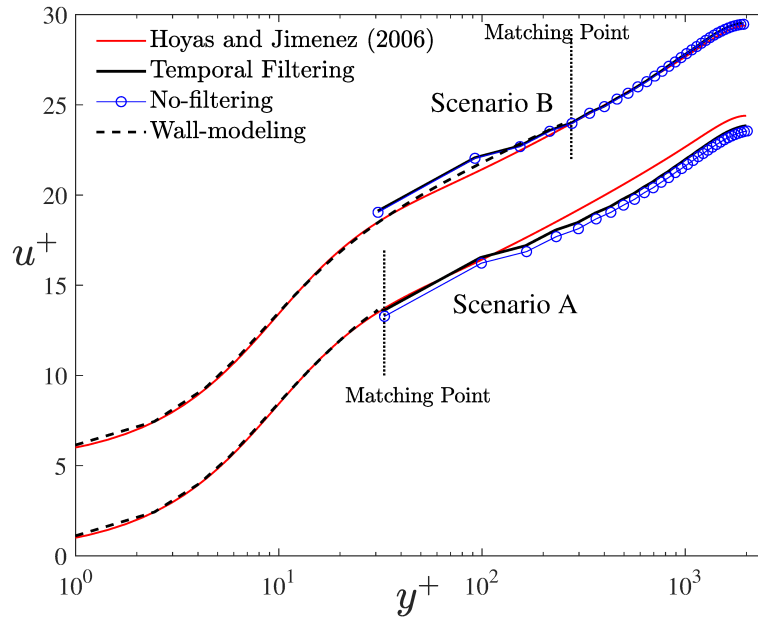


Figure 4.15: Temporal filtering versus no-filtering with $T_W = 1.0$ and $T_F = 1.0$.

and may be unnecessary. Yang et al. (2017) concluded that temporal filtering is essential when the matching point is located at the first node off the wall. In the wall layer and below the matching point, the mean velocity profile obtained from the wall-modeling (dashed-line) matches the DNS results of Hoyas and Jiménez (2006) very well, and it can serve as an alternative solution to the results of the LES in the wall region. Recall that the results presented in Fig. 4.15 were achieved with $T_W = 1.0$ and $T_F = 1.0$ for the temporal-filtered cases. In the following paragraphs, the use of different values for the time averaging and temporal filtering time periods are investigated to reveal their effects on the mean velocity profile.

Fig. 4.16 presents the performance of wall-modeling for other values of the time averaging and temporal filtering characteristic time scales. The values $T_W = 0.1$ and $T_F = 0.1$ show the effects of shorter time periods for averaging the wall layer and filtering input from the LES domain. A smaller value for T_F implies that the top boundary of the wall layer is now responsive to the higher frequency turbulent fluctuations. Two values, $T_F = 1.0$ and 0.1 , are introduced to evaluate the effects of temporal filtering, while two characteristic time scales, $T_W = 1.0$ and 0.1 , are investigated for time averaging. The upper set of mean velocity profiles in Fig. 4.16a relate to Scenario A, where the wall layer is resolved with a temporal filtering using $T_F = 0.1$. The mean velocity profiles are under-predicted regardless of the time averaging period. In the lower set of profiles with $T_F = 1.0$, the velocity profile at $T_W = 1.0$ matches better with the DNS results. The overall conclusion of Fig. 4.16a is that a better prediction is obtained for the results with $T_F = 1.0$ compared to the results with $T_F = 0.1$.

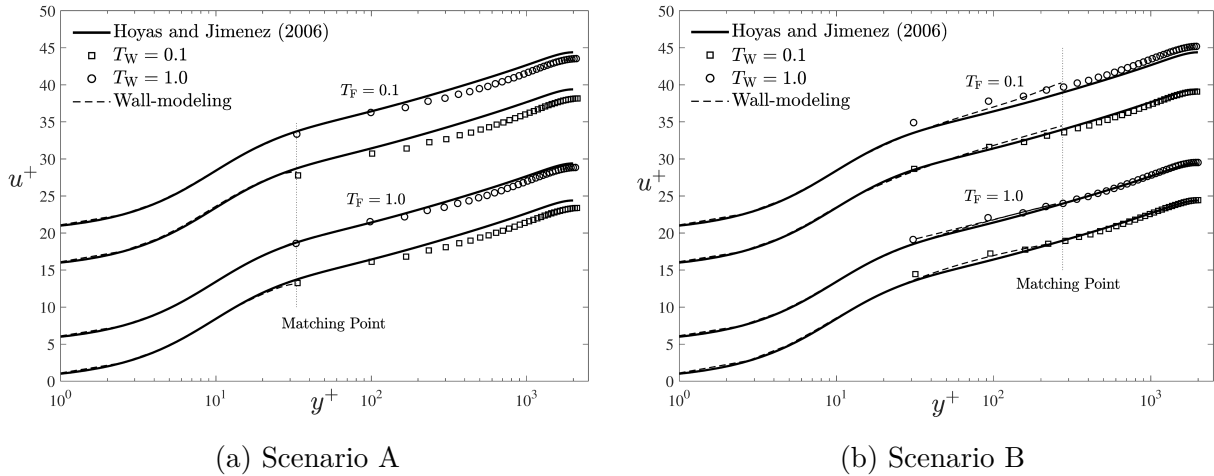


Figure 4.16: The effects of various filtering and averaging time periods: (a) Scenario A with the matching point at the first node, and (b) Scenario B with the matching point at the fifth node.

It substantiates the role of filtering high-frequency flow information from the outer layer to reduce the mismatch in the simulations for a matching point located at the first node.

Next, Scenario B is considered and the results are shown in Fig. 4.16b. At first glance, the results look independent of the temporal filtering scheme in contrast to Fig. 4.16a. However, a smaller time averaging period ($T_W = 0.1$) results in a better prediction of the flow field for both temporal filtering cases. In general, the mean velocity profiles with $T_F = 1.0$ are slightly closer to the DNS than the results with $T_F = 0.1$. Additional simulations were conducted for test cases without temporal filtering. The results (not shown here) reconfirm that a smaller value for time averaging, i.e. $T_W = 0.1$, improves the prediction of the mean velocity profile.

The performance of time averaging and temporal filtering as a function of the location of the matching point is evaluated and also shown in Fig. 4.16. The mean velocity profiles in Scenario A are under-predicted in all cases, which is the consequence of the over-prediction of the friction velocity due to the use of the SGS model on a coarse grid in the near-wall region, as discussed earlier. Higher values of T_F and T_W indicate better performance in Scenario A. On the other hand, Scenario B shows a minimal dependence on the variations of the averaging schemes. According to the small changes observed, a combination of a higher value of T_F and a lower value of T_W seems to improve the performance of the averaging schemes in Scenario B. Comparing Scenario A with Scenario B based on time averaging and temporal filtering schemes, note that moving the location of the matching point to a higher node in the LES domain implies more grid points are used to resolve the wall layer, which then increases the computational cost of the wall-modeling. For instance, the wall layer is resolved with 20 nodes in the wall-normal direction in Scenario A whereas 30 nodes are used in Scenario B. This leads to a lower resolution at the top of the wall layer (matching point) in Scenario B, i.e. $\Delta y^+ \approx 16$, while Scenario A has a grid spacing of $\Delta y^+ \approx 0.5$ for the last node in the wall-normal direction.

To examine the interaction between the LES and the wall model, two probes tracked the velocity components in the channel flow close to the matching point ($x = \pi\delta$, $y = h_{wm}$, $z = \frac{2}{3}\pi\delta$). One of them recorded the instantaneous and temporal-filtered streamwise velocities inside the LES domain, while the other probe tracked the time-averaged velocity in the wall layer at the last node in the wall-normal direction. Figs. 4.17 and 4.18 present the velocity fluctuations recorded by these probes over a finite time period, where the time T is normalized by the convective time scale. Note that the temporal-filtered velocity is introduced to the wall layer as a top boundary condition. The upper set of profiles in Fig. 4.17 corresponds to $T_W = 1.0$ and are shifted a half unit upwards for clarity. The lower set of profiles pertain to

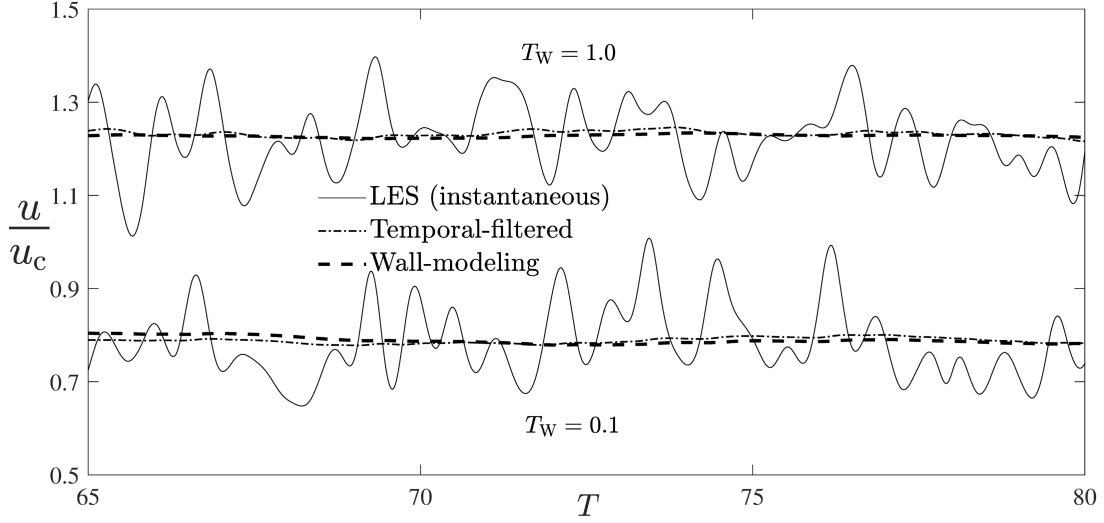


Figure 4.17: Tracking the streamwise velocity at the matching point (5th node) for the instantaneous and temporal-filtered LES and time-averaged wall layer with the dimensionless filtering time period $T_F = 1.0$.

the test cases with $T_W = 0.1$. It is obvious that for both cases in Fig. 4.17 with $T_F = 1.0$, the temporal-filtered velocity and consequently the wall layer velocity does not respond to the high-frequency fluctuations in the LES field at the matching point.

In contrast, the upper set of profiles in Fig. 4.18, which presents the results for $T_F = 0.1$ and $T_W = 1.0$, indicates that the temporal-filtered velocity now begins to respond to the stronger fluctuations in the LES domain. However, there is no minimal response to the stronger fluctuations in the wall layer velocity. The values of $T_W = 0.1$ and $T_F = 0.1$ are applied to the test cases in the lower region of Fig. 4.18. The results show a rapid response to the high-frequency fluctuations in the temporal-filtered velocity, which is also observed in the wall layer when a shorter period is used for time averaging. Although using $T_F = 0.1$ creates a very responsive wall model, non-essential high-frequency fluctuations are introduced to the wall layer, and the wall layer is unable to respond to the essential stress-carrying turbulent motions. This issue was evident in Fig. 4.16a where the mean velocity profiles are under-predicted. Further analysis of the effects of different values of T_W and T_F on the mean velocity field is given below.

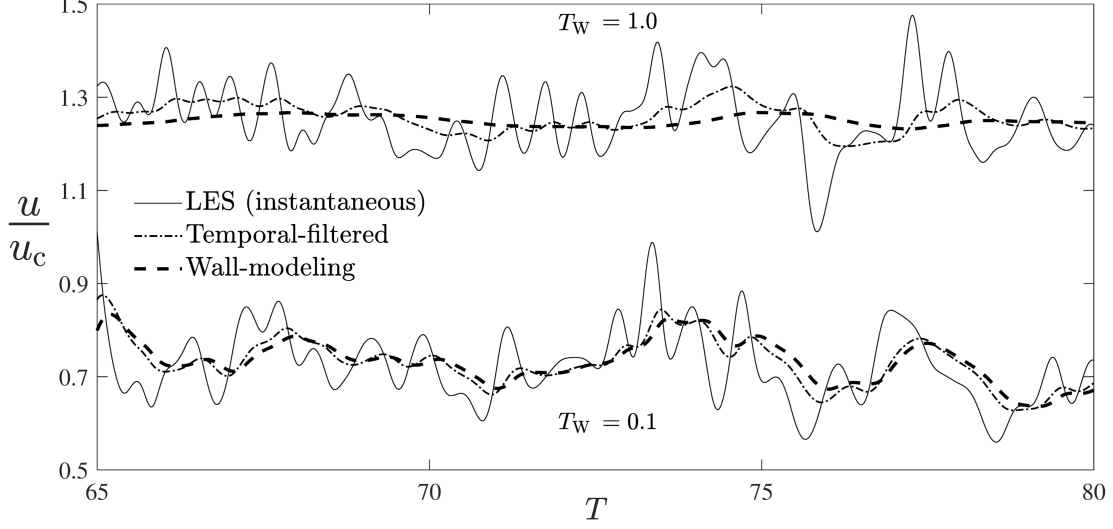


Figure 4.18: Tracking the streamwise velocity similar to Fig. 4.17 with $T_F = 0.1$.

4.5.4 Wall Layer Response to Input Velocity

To investigate the effect of the time period employed for time averaging the flow solution in the wall layer, the streamwise velocity inside the wall layer was tracked at the first node near the wall, in the buffer region, and in the log-law region using three probes. A channel flow with $T_F = 1.0$ and the matching point located at the fifth node was used to conduct the numerical experiment. The temporal-filtered velocity at the top boundary of the wall layer, which drives the flow motions in the wall layer, was also monitored. Non-dimensional velocity fluctuations tracked by each probe over time are shown in Fig. 4.19. A local peak is observed at $T = 76$ for the temporal-filtered profile used as input to the wall layer. The probe inside the wall layer at $y^+ = 112$ indicates a peak at $T = 81$ as shown in Fig. 4.19a. Local peaks for the next two probes at $y^+ = 40$ and $y^+ = 0.87$ are observed at $T = 96$ and $T = 117$, respectively. The first node off the wall represents the fluctuations in the wall shear stress. A blue line connects the local peaks of each probe with a slope of $1/5200$. Although the temporal-filtered velocity varies too quickly to precisely identify the local peak that drives the other peaks, a plausible peak in the temporal-filtered velocity is shown, but it was not included in determining the slope. Fig. 4.19a indicates that the wall layer with $T_W = 1.0$ responds to a strong fluctuation in the LES domain over a relatively long time span (36 times the convective time scale). A different trend was observed when T_W was decreased to 0.1. Fig. 4.19b displays the local peaks for the velocity at the input, highest, middle, and lowest probes at $T = 80, 82, 85$, and 88 , respectively. This implies that a specific fluctuation passes through the wall layer and reaches the wall in less than 500 time steps (8 times the

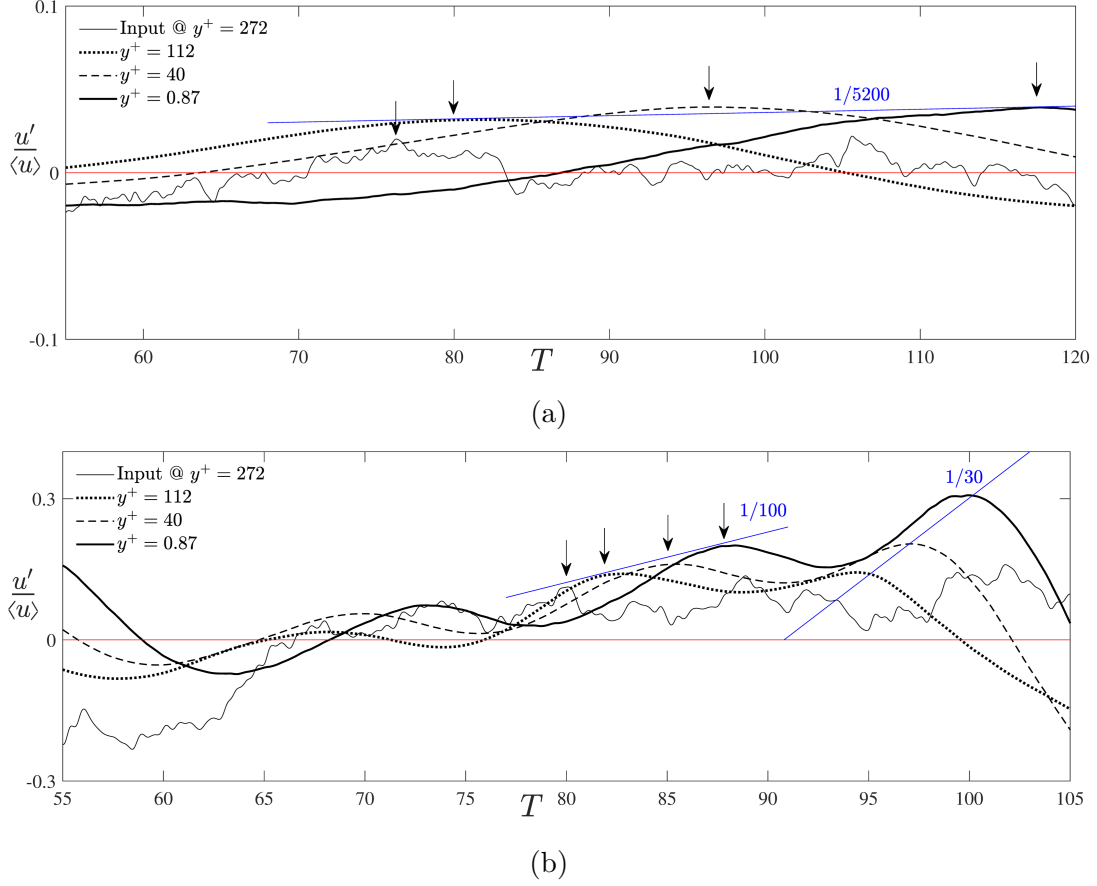


Figure 4.19: Response of wall-modeling to LES field for dimensionless averaging time periods of (a) $T_W = 1.0$, and (b) $T_W = 0.1$.

convective time scale). In comparison to Fig. 4.19a, this local peak approaches the wall at least six times faster. Another set of local peaks is also identified, and the slopes of the fitted-blue lines for these two sets of peaks are approximately $1/100$ and $1/30$. This shows a more responsive wall layer to the oscillations in the flow field at the top boundary. One can conclude from Fig. 4.19 that implementing an averaging time period comparable to the convective time scale ($T_W = 1.0$) leads to a relatively slow response in the wall layer to the fluctuations in the LES region. This behavior resembles that in the study of Park and Moin (2014).

The main feedback to the LES from the wall layer is the wall shear stress, which will be scrutinized in the following analysis. Fig. 4.20 indicates the wall shear stress with time advancement. Since the wall shear stress is estimated by $\tau_w = \mu \frac{du}{dy}$, the velocity at the first node in the wall layer is representative of the wall shear stress. The variations in wall shear stress for four different test cases are presented in Fig. 4.20 using different values for T_W and T_F as previously discussed with Fig. 4.17 and 4.18. The wall shear stress fluctuations

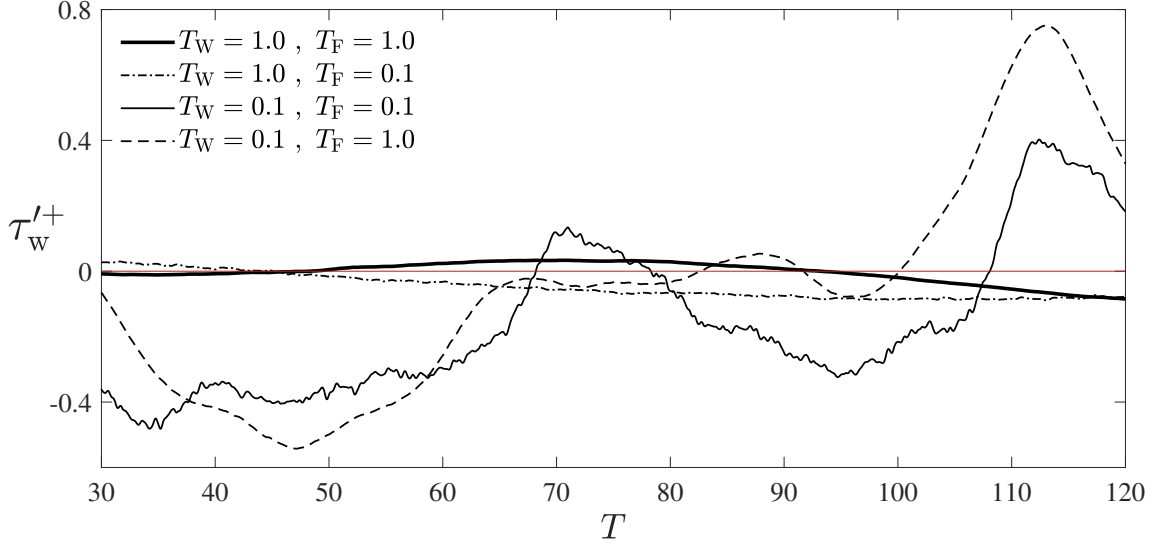


Figure 4.20: Wall shear stress fluctuations for various T_F and T_W values for the WMLES channel flow at $\text{Re}_\tau = 2000$.

and velocity variations in the LES are normalized by the corresponding mean values. The profiles with $T_W = 1.0$ show slow variations over time, whereas the profiles with $T_W = 0.1$ indicate more rapid variations. It can be concluded that a lower value for time averaging is the proper choice for wall-modeling. The case with $T_F = 1.0$ damped high-frequency signals in the LES, while the case with $T_F = 0.1$ admits more variations with higher frequencies.

The results of a wall-resolved channel flow are introduced to investigate the wall shear stress fluctuations in addition to the WMLES turbulent channel flow, as shown in Fig. 4.21. However, due to the high computational cost of the high resolution required for a wall-resolved channel flow at a Reynolds number comparable to the WMLES channel flow, i.e. $\text{Re}_\tau = 2000$, the wall-resolved channel flow was simulated for $\text{Re}_\tau = 395$. Fig. 4.21 shows the τ_w fluctuations for both the wall-resolved and wall-modeled moderate Reynolds number channel flow, while the results of the WMLES channel flow at $\text{Re}_\tau = 2000$ are also included with $T_F = 1.0$ and $T_W = 0.1$. Comparing the τ_w fluctuations in the WMLES at $\text{Re}_\tau = 395$ and $\text{Re}_\tau = 2000$, a higher amplitude is observed for the WMLES channel flow at $\text{Re}_\tau = 395$. Recall that the wall-modeling was intended for turbulent flows at high Reynolds numbers since the coarse grid near the wall represents the time-averaged effects of the small flow structures in the near-wall region (Piomelli and Balaras, 2002). For wall-modeling at a moderate Reynolds number, some of the small turbulent structures can be resolved due to a higher grid resolution compared to the grid resolution used at higher Reynolds numbers. The variation of the wall shear stress for the WRLES at $\text{Re}_\tau = 395$ is also shown to provide a better comparison between the wall-resolved and wall-modeled channel flows. Since the

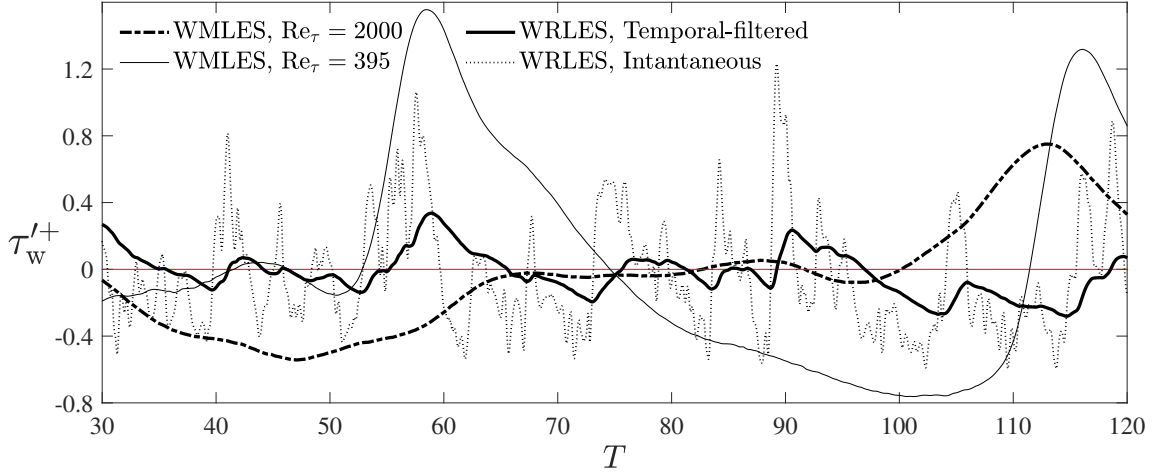


Figure 4.21: Comparison of wall shear stress fluctuations of WMLES (at $Re_\tau = 2000$ and $Re_\tau = 395$ with $T_F = 1.0$ and $T_W = 0.1$) with WRLES at $Re_\tau = 395$ with/without temporal filtering with $T_F = 1.0$.

input to the wall model is filtered over T_F , the temporal-filtered wall shear stress obtained by the wall-resolved channel flow is also presented for comparison. Hence, a temporal filtering scheme analogous to what is used for the WMLES channel flows is implemented for τ_w for the WRLES channel flow with $T_F = 1.0$. Both the WRLES and WMLES profiles at $Re_\tau = 395$ show the variations in τ_w based on the flow velocity at $y^+ \approx 0.8$. It is clear that the fluctuations in the WMLES profile respond slowly to the LES input at the matching point in contrast to the temporal-filtered WRLES. Using an unsteady approach, the WRLES is able to track the instantaneous wall shear stress whereas the Reynolds-averaged value in the WMLES varies slowly over time. However, the amplitude of the variations in the wall shear stress obtained from the WMLES is higher than that of the WRLES at a moderate Reynolds number.

4.5.5 Grid Distribution and Matching Point

Given the results in previous sections, one can conclude that the WMLES obtains better performance in the prediction of the wall shear stress using $T_F = 1.0$ and $T_W = 0.1$. Those values correspond to the turbulent diffusion time scale for the wall layer and a time scale which is smaller than the convective time scale used for temporal filtering and time averaging, respectively. In this section, two other scenarios are introduced to further investigate the characteristics of the wall layer. In Scenario C, the matching point is moved to the 3rd node, and the grid distribution in the wall-normal direction changes to maintain the first node (in

the wall layer) at $y_1^+ \approx 0.87$ with the same number of grid points, i.e. 30. Scenario D keeps the matching point at the first node in the LES domain while the wall-normal grid distribution in the wall layer is modified to locate the first grid point (in the wall layer) at $y_1^+ \approx 0.17$. The number of wall-normal grid points increases to 30 in contrast to Scenario A which used 20 nodes. The mean velocity profiles for Scenario A to D using $T_F = 1.0$ and $T_W = 0.1$ are shown in Fig. 4.22. The upper set of profiles pertains to Scenario B and C with the matching point above the first node. A better prediction is observed using temporal-filtered cases, while the cases without temporal filtering (NTF) slightly under-predict the mean velocity profiles. Recall that the TF and NTF cases in Fig. 4.15 show similar results. In that case, the wall layer was averaged with $T_W = 1.0$ whereas the time averaging period implemented in Fig. 4.22 is much shorter. It is observed that the effects of moving the matching point from the 5th to the 3rd node have minimal effect on the final results. The matching points, i.e. $y^+ = 272$ for Scenario B and $y^+ = 155$ for Scenario C, are located above the buffer layer and in the log-law region.

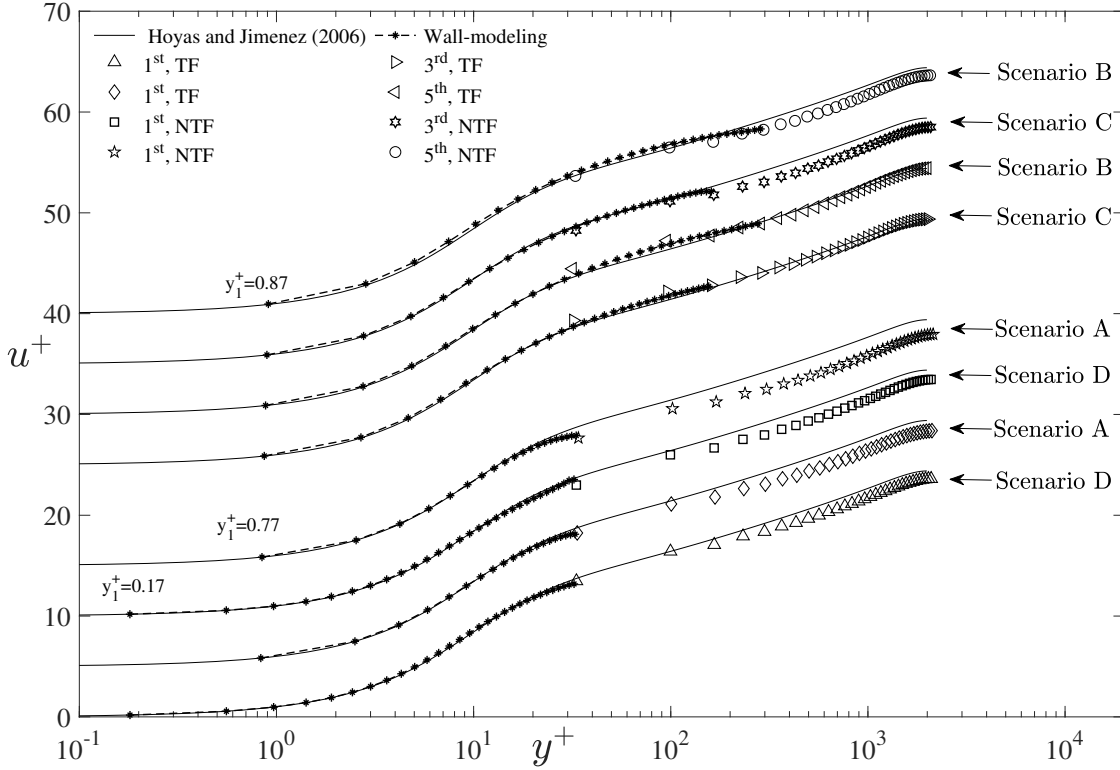


Figure 4.22: Comparison of four scenarios with $T_F = 1.0$ and $T_W = 0.1$ using the temporal filtering (TF) and non-temporal filtering (NTF) schemes. The profiles in the lower region pertain to Scenario A and D, where the matching point is located at the first node. The upper region presents the results for Scenario B and C with the matching point located at the 5th and 3rd nodes, respectively.

The lower set of profiles in Fig. 4.22 pertains to Scenario A and D. The cases without temporal filtering indicate a noticeable mismatch, while the cases with temporal filtering demonstrate better results for both scenarios. A comparison between Scenario A and D for similar filtering conditions reveals that Scenario D yields a better prediction of the mean velocity profile, which demonstrates the potential of moving the first node in the wall layer closer to the wall (e.g. $y_1^+ \approx 0.17$) to alleviate the mismatch in the velocity profiles. A plausible reason is that the wall layer is more dependent on the flow motions inside the viscous sub-layer region than the flow structures at the top boundary in the prediction of the friction velocity. The main conclusion from this analysis is that the temporal filtering and time averaging schemes are able to mitigate the mismatch, and that the location of the first node in the wall layer relative to the wall should also be considered, especially in cases with the matching points located at the first node in the LES.

4.6 Conclusions

Wall-modeled and wall-resolved turbulent channel flows were studied at Reynolds numbers ranging from $Re_\tau = 395$ to 2000. The instantaneous flow structures were solved by the filtered NSEs. The performance of the DSM and DNM in a wall-resolved channel flow at $Re_\tau = 395$ was investigated in terms of the dissipation of the filtered and unfiltered motions. It was found that the DSM underestimates the residual flow motions, which results in the over-prediction of the mean velocity profile and velocity fluctuations. Hence, the DNM was applied to calculate the residual stresses for all simulations. Next, a dynamic non-equilibrium wall model was implemented to model the wall layer at the same Reynolds number with a lower grid resolution, especially near the wall. The results indicated that the WMLES can predict the mean velocity profile and velocity fluctuations compared to available numerical studies although some nodes below the matching point are overestimated. The performance of the SGS models in the near-wall region is inadequate due to the use of a very coarse grid which on the other hand reduces the simulation run-time. Furthermore, different locations for the matching point were studied, and it was concluded that the matching point should be located away from the wall for a better prediction of the friction velocity.

The characteristic time scale of time averaging in the wall layer and temporal filtering at the matching point were investigated together with the location of the matching point in a high Reynolds number channel flow at $Re_\tau = 2000$. An analysis of averaging in the wall layer indicates that the wall model responds very slowly to the variations at the top

boundary when too large a time period is employed for time averaging. Consequently, neither the temporal-filtered nor unfiltered flow data from the LES domain provide an appropriate boundary condition for the wall model. A realistic wall shear stress from the wall model is achieved when a smaller time averaging period is implemented. The role of temporal filtering of the input to the wall layer is more essential when the matching point is located close to the wall. A period comparable to the turbulence diffusion time scale is recommended for temporal filtering in all scenarios regardless of the location considered for the matching point. However, temporal filtering with $T_F = 1.0$ and time averaging with $T_W = 0.1$ yield a better prediction and more responsive wall layer when the matching point is located farther away from the wall. In contrast, a longer time period for time averaging (i.e. $T_W = 1.0$) indicates better performance for cases with a matching point at the first node ($y^+ < 100$). Overall, it is shown that time averaging and temporal filtering schemes reduce the mismatch of the mean velocity profile for WMLES turbulent flows.

Chapter 5

Numerical Approach to Inflow Generation for Turbulent Boundary Layers

Using simply periodic boundary conditions to generate realistic turbulence at the inlet boundary of a TBL results in the growth of the boundary layer. Some modifications are required to rescale the flow field before recycling it back to the inlet. In the recycling method, the velocity field obtained from the recycling station at an appropriate distance from the exit plane is rescaled and transferred to the inflow boundary. In this chapter, the numerical methodology of the Lund-Wu-Squires (LWS) method is described and implemented for the simulation of TBLs in Chapter 6. The LWS method is reliable if the location of the recycling plane is correctly specified. Note that many recycling methods that originated from the LWS method have been modified for specific flow problems. The TBL considered in this research has a simple geometry without any surface roughness. Hence, the LWS method is selected to generate realistic turbulence at the inlet boundary of the simulation domain.

5.1 LWS Method

The Spalart-type inflow generation method needs a coordinate transformation to produce streamwise homogeneity, and it requires multiple simulations to estimate the growth terms. In contrast, the LWS method is conducted in a Cartesian coordinate frame and is compatible with conventional flow solvers. The spatial growth of the boundary layer is computed directly

from the mean flow field downstream to estimate the rescaling parameters. A fixed boundary layer thickness at the inlet boundary is used, and a single empirical correlation calculates the friction velocity at the inlet station. In general, turbulent boundary layers follow a scaling law that suggests a similarity coordinate. More specifically, the mean velocity in the inner region conforms with the law of the wall, whereas the defect law prevails in the outer region (Wu et al., 1995).

The first step of the rescaling method is to decompose the velocity components at the recycling station into the fluctuating and mean parts. The mean velocity U in Eq. 5.1 is obtained by averaging in time and the spanwise direction. Subsequently, the fluctuating part is obtained as follows (Lund et al., 1998):

$$u'_i(x, y, z, t) = \tilde{u}_i(x, y, z, t) - U_i(x, y), \quad (5.1)$$

where u' is the fluctuation, and \tilde{u} is the filtered instantaneous velocity. For clarity, the streamwise, wall-normal, and spanwise velocity components are denoted by \tilde{u} , \tilde{v} , and \tilde{w} and the corresponding coordinate directions as x , y , and z , respectively.

5.1.1 Rescaling the Mean Velocity

The mean velocity field is divided into a near-wall and outer region. The similarity coordinate in the inner and outer regions is given by $y^+ = yu_\tau/\nu$ and $\zeta = y/\delta$, respectively, where y^+ is the wall coordinate, y is the distance from the wall, and δ is the boundary layer thickness. Hence, the law of the wall and the defect law are expressed as

$$\begin{aligned} U^{\text{inner}} &= u_\tau f_1(y^+) && \text{Law of the wall,} \\ U_\infty - U^{\text{outer}} &= u_\tau f_2(\zeta) && \text{Defect law,} \end{aligned} \quad (5.2)$$

where $u_\tau = \sqrt{\nu(\partial U/\partial y)_{\text{wall}}}$ is the friction velocity, and f_1 and f_2 are two universal functions. f_1 and f_2 indicate the functional dependence and scaling acceptance, and they are required to be determined.

The relations used to determine the rescaled streamwise velocities at the inlet for both the inner and outer regions are as follows:

$$U_{\text{inlet}}^{\text{inner}} = \gamma U_{\text{recy}}(y_{\text{inlet}}^+), \quad (5.3)$$

$$U_{\text{inlet}}^{\text{outer}} = \gamma U_{\text{recy}}(\zeta_{\text{inlet}}) + (1 - \gamma)U_\infty. \quad (5.4)$$

The mean velocity at the recycling station U_{recy} in Eq. 5.3 is evaluated for the inner coordinate y_{inlet}^+ at the inlet station. Since the wall unit at the inlet station is different from the one at the recycling station, a linear interpolation is used for the mean velocity. A similar procedure should be employed for the velocity in the outer region based on the boundary layer thickness. The scaling factor γ in Eqs. 5.3 and 5.4 is defined as

$$\gamma = \frac{u_{\tau, \text{inlet}}}{u_{\tau, \text{recy}}}. \quad (5.5)$$

To obtain the mean wall-normal velocity component consistent with the scaling of the mean velocity profile, $V^{\text{inner}} \sim (\nu/u_\tau) du_\tau/dx$ in the inner region and $V^{\text{outer}} \sim u_\tau d\delta/dx$ in the outer region should be employed based on the continuity equation. Approximating the derivatives du_τ/dx and $d\delta/dx$ is problematic. Instead, the following scalings are implemented as convenient approximations:

$$\begin{aligned} V^{\text{inner}} &= U_\infty f_3(y^+), \\ V^{\text{outer}} &= U_\infty f_4(\zeta), \end{aligned} \quad (5.6)$$

where f_3 and f_4 are two other universal functions. The mean value of the V velocity at the inlet station is related to that at the recycling station as follows:

$$V_{\text{inlet}}^{\text{inner}} = \gamma V_{\text{recy}}(y_{\text{inlet}}^+), \quad (5.7)$$

$$V_{\text{inlet}}^{\text{outer}} = \gamma V_{\text{recy}}(\zeta_{\text{inlet}}). \quad (5.8)$$

No scaling is required for the mean spanwise velocity, since it is assumed to be zero at the inlet boundary;

$$W_{\text{inlet}}^{\text{inner}} = W_{\text{inlet}}^{\text{outer}} = 0. \quad (5.9)$$

5.1.2 Rescaling the Fluctuating Velocity

The fluctuating parts are scaled similarly using the wall units and boundary layer thickness in the inner and outer regions, respectively. The friction velocity as an explicit parameter is used for scaling the fluctuations to isolate the streamwise inhomogeneity, i.e.

$$\begin{aligned} (u'_i)^{\text{inner}} &= u_\tau f_5(x, y^+, z, t), \\ (u'_i)^{\text{outer}} &= u_\tau f_6(x, \zeta, z, t). \end{aligned} \quad (5.10)$$

The universal functions f_5 and f_6 are supposed to be homogeneous in the streamwise direction. In contrast to the periodic boundary condition implemented by Spalart and Leonard (1987), the fluctuations at the recycling station are transferred to the inlet using Eq. 5.10, and a convective boundary condition is used at the exit plane. The velocity fluctuations at the inlet boundary are obtained by

$$(u'_i)_{\text{inlet}}^{\text{inner}} = \gamma (u'_i)_{\text{recy}}(y_{\text{inlet}}^+, z, t), \quad (5.11)$$

$$(u'_i)_{\text{inlet}}^{\text{outer}} = \gamma (u'_i)_{\text{recy}}(\zeta_{\text{inlet}}, z, t). \quad (5.12)$$

5.1.3 Inflow Velocity Component

To combine Eqs. 5.3 to 5.12 into a single equation that provides the velocity components in both the inner and outer regions, the following expression using a weighting factor is adopted:

$$\tilde{u}_{i,\text{inlet}} = [(U_i)_{\text{inlet}}^{\text{inner}} + (u'_i)_{\text{inlet}}^{\text{inner}}] [1 - W(\zeta_{\text{inlet}})] + [(U_i)_{\text{inlet}}^{\text{outer}} + (u'_i)_{\text{inlet}}^{\text{outer}}] W(\zeta_{\text{inlet}}), \quad (5.13)$$

where the weighting function W is defined by

$$W(\zeta) = \frac{1}{2} \left[1 + \tanh \left[\frac{\alpha(\zeta - b)}{(1 - 2b)\zeta + b} \right] / \tanh(\alpha) \right], \quad (5.14)$$

where $\alpha = 4$ and $b = 0.2$ to give a smooth transition between the inner and outer layers as shown in Fig. 5.1. The parameter b defines the location at which the rescaled velocities obtained from the inner and outer rescaling coordinates make an equal contribution to the

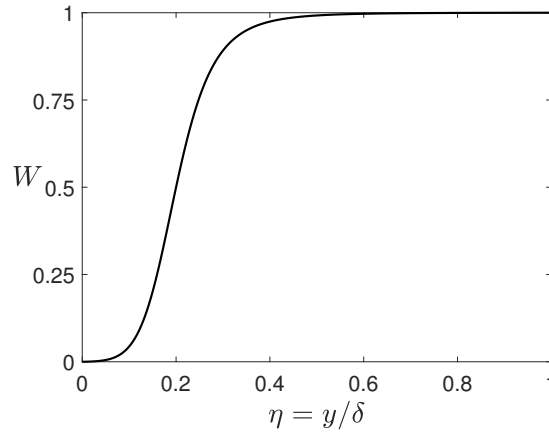


Figure 5.1: Weighting function across the boundary layer.

final inlet velocity, which implies $W = 0.5$. The width of the transition region is determined by α ; higher values for α transform the weighting function into a step function at b . A constraint of $W = 1$ is imposed for W larger than one.

Scaling parameters u_τ and δ are required at both the recycling station and inlet. The mean velocity profile at the recycling station is employed to estimate the friction velocity and boundary layer thickness. It was found that using fixed u_τ and δ independently at the inlet leads to an unrealistic solution (Lund et al., 1998). Hence, one of these two parameters relates to the solution downstream and the other one is used as a controlling parameter. The LWS method fixes δ at the inlet and calculates u_τ based on an empirical correlation as follows:

$$u_{\tau,\text{inlet}} = u_{\tau,\text{recy}} \left(\frac{\theta_{\text{recy}}}{\theta_{\text{inlet}}} \right)^{1/[2(n-1)]}, \quad (5.15)$$

where θ is the momentum thickness obtained from the following relation using the mean velocity profile at the recycling station and inlet (White, 2003):

$$\theta = \int_0^\infty \frac{U}{U_\infty} \left(1 - \frac{U}{U_\infty} \right) dy. \quad (5.16)$$

The empirical relation in Eq. 5.15 is derived from a power-law approximation of the momentum thickness and skin-friction coefficient with $n = 5$;

$$\frac{\theta}{x} \sim \text{Re}_x^{-1/n}, \quad C_f \sim \text{Re}_x^{-1/n}. \quad (5.17)$$

5.2 Heaviside Function

Rescaled fluctuations are used only inside the boundary layer; imposing the fluctuations outside the boundary layer results in sharp changes at the inlet boundary that may propagate into the flow. A smooth transition from inside the boundary layer to the outside occurs if the fluctuations are rescaled in the freestream region. However, an unstable top boundary is observed if the rescaled fluctuations extend outside the boundary layer. Hence, a smoothed Heaviside function is implemented to suppress the fluctuations outside the boundary layer

at the inflow boundary as follows (Sussman et al., 1999; Bohr, 2005):

$$H(\phi) = \begin{cases} 1 & \text{if } \phi < -\epsilon \\ \frac{1}{2} \left[1 - \frac{\phi}{\epsilon} - \frac{1}{\pi} \sin \left(\frac{\pi\phi}{\epsilon} \right) \right] & \text{if } |\phi| \leq \epsilon \\ 0 & \text{if } \phi > \epsilon, \end{cases} \quad (5.18)$$

where ϕ defines the distance from a new coordinate near the edge of the boundary layer as

$$\phi = y - 1.2\delta_{\text{inlet}} - \epsilon. \quad (5.19)$$

The second term in Eq. 5.19 indicates that the fluctuations begin to reduce after $1.2\delta_{\text{inlet}}$, and they smoothly transition to zero over a distance of 2ϵ , which is specified as a function of the boundary layer thickness at the inlet, i.e. $\epsilon = \frac{\delta_{\text{inlet}}}{4}$. Fig. 5.2 shows the Heaviside function for different values of ϵ .

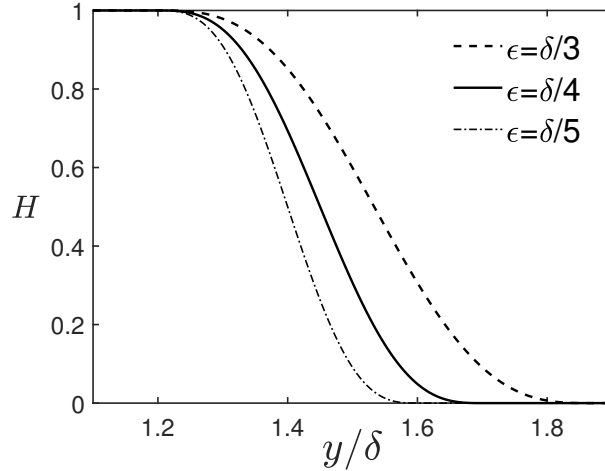


Figure 5.2: Heaviside function.

5.3 Boundary Conditions

Boundary conditions are both critical and challenging in the simulation of a TBL. The inlet boundary was described in the previous sections, and the LWS method was selected for generating the turbulent velocity field at the inflow plane. The other boundaries, i.e. the outlet plane, top of the domain, lateral sides, and the lower wall are shown in Fig. 5.3. In

this section, the boundaries at the top and outlet planes are discussed in detail and different boundary conditions from the literature are presented.

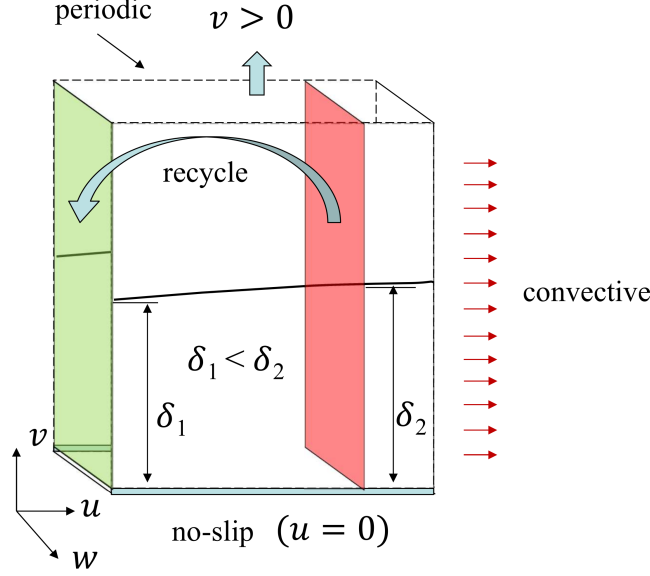


Figure 5.3: Boundary conditions in the turbulent boundary layer.

5.3.1 Top Boundary Treatment

In the mean flow field, the boundary layer grows along the flow stream as shown in Fig. 5.3. This is manifest as an increase in the boundary layer thickness δ . As a result, the wall-normal velocity at the top boundary should take a positive value. This is consistent with mass conservation, and the wall-normal velocity is estimated by the following relation (Lund et al., 1998):

$$\tilde{v}(x) = U_\infty \frac{d\delta^*}{dx} + (\delta^* - h) \frac{dU_\infty}{dx}, \quad (5.20)$$

where h is the height of the simulation domain, and δ^* is the displacement thickness given by

$$\delta^* = \int_0^\infty \left(1 - \frac{U}{U_\infty}\right) dy. \quad (5.21)$$

The first term on the right-hand side of Eq. 5.20 relates to the mass flux that should leave the domain at the top due to the growth of the displacement thickness. The second term estimates the decrease in the mass flux of the boundary layer due to a finite pressure gradient. ZPGTBLs are used in this research; hence, the second term on the right-hand side of Eq. 5.20 is assumed to be zero. The velocity gradients of the streamwise and spanwise veloc-

ity components are assumed to be zero at the top boundary, so that the boundary conditions become as follows:

$$\frac{\partial \tilde{u}}{\partial y} = 0 \quad , \quad \tilde{v} = U_\infty \frac{d\delta^*}{dx} \quad , \quad \frac{\partial \tilde{w}}{\partial y} = 0. \quad (5.22)$$

There are a variety of boundary conditions in the literature presented in Table 5.1 which are different from those in Eq. 5.22. Ferrante and Elghobashi (2004) used a simple boundary condition for spatially developing boundary layers: a zero wall-normal velocity at the top boundary in a zero pressure gradient (ZPG) flow together with the zero gradient condition for the two other velocity components. A growing boundary layer requires a mass flux at the top boundary to conserve mass in the flow domain, and this is in conflict with a zero mass flux at the top boundary. In a boundary layer with adverse pressure gradient (APG), Na (1996) estimated the wall-normal velocity V_{TOP} based on a blowing-suction velocity distribution to match the wall-pressure distribution of their experiment. This boundary condition was also used in a ZPGTBL. A zero-vorticity boundary condition was applied for the streamwise velocity, while a zero gradient Neumann boundary condition was used to estimate the velocity component in the spanwise direction. Lee et al. (2010) focused on the streamwise velocity instead of the vertical velocity. They suggested that the streamwise velocity at the top plane should have the form of a power-law correlation for a boundary layer with an APG, and the wall-normal velocity was described by the zero-vorticity boundary condition. The power exponent m as shown in Table 5.1 takes $m = 0, -0.15$, and -0.2 corresponding to a ZPG, moderate APG, and strong APG turbulent boundary layer, respectively. Wu and Moin (2009) considered a transitional boundary layer and suggested using the analytical profile proposed by Blasius for the estimation of the vertical velocity at the top boundary. The zero-vorticity

Table 5.1: Top boundary conditions in turbulent boundary layers.

	u	v	w
Lund et al. (1998)	$\frac{\partial u}{\partial y} = 0$	$v = U_\infty \frac{\partial \delta^*}{\partial x}$	
Ferrante and Elghobashi (2004)	$\frac{\partial u}{\partial y} = 0$	$v = 0$	
Na (1996) (APG)	$\frac{\partial u}{\partial y} = \frac{\partial v}{\partial x}$	$v = V_{\text{TOP}}(x)$	$\frac{\partial w}{\partial y} = 0$
Lee et al. (2010) (APG)	$U_\infty \left(1 - \frac{x}{x_o}\right)^m$	$\frac{\partial v}{\partial x} = \frac{\partial u}{\partial y}$	
Wu and Moin (2009)	$\frac{\partial u}{\partial y} = \frac{\partial v}{\partial x}$	$V_{\text{Blasius}} = 0.86 \sqrt{\frac{\nu U_\infty}{x}}$	$\frac{\partial w}{\partial y} = \frac{\partial v}{\partial z}$

condition was applied for the streamwise and spanwise velocity components. The last three studies implemented the zero-vorticity condition for the streamwise velocity. This indicates a potential for employing the zero-vorticity conditions instead of the zero velocity gradient while the boundary conditions of Lund et al. (1998) are applied.

5.3.2 Adjustment of Outflow

Several exit boundary conditions have showed appropriate behavior for both boundary layers and mixing layers. Pauley et al. (1990) applied different boundary conditions at the outlet for an unsteady laminar separated boundary layer, and they found that the viscous terms should be removed from the outflow boundary conditions to prevent numerical instability. The time-dependent convective boundary conditions developed by Lowery (1987) for spatially evolving mixing layers provided good performance in moving structures out of the simulation domain.

$$\frac{\partial \tilde{u}_i}{\partial t} + U_c \frac{\partial \tilde{u}_i}{\partial x} = 0, \quad (5.23)$$

where U_c is the convective velocity, which is obtained by averaging the mean streamwise velocity across the exit plane. It is appealing to use a local bulk velocity in this context. A space-dependent U_c does not guarantee mass balance at each time step between the inflow and outflow boundaries, and a mass correction is required at the outflow boundary. However, a negligible difference was observed between case studies using a variable and constant U_c (Le, 1995; Na, 1996).

Assuming the last interior node in the streamwise direction is ie and the fictitious node is $ie + 1$ as shown in Fig. 5.4, the discretization of Eq. 5.23 over the exit plane is as follows:

$$\tilde{u}_{ie+1}^{n+1} = \tilde{u}_{ie+1}^n - \frac{U_c \Delta t}{\Delta x_e} (\tilde{u}_{ie+1}^n - \tilde{u}_{ie}^n), \quad (5.24)$$

where the superscript $n + 1$ indicates the value of the parameter at the new time step, and n indicates the value obtained from the old solution.

5.4 Summary

The boundary conditions for the simulation of TBLs were discussed in this chapter. The inflow boundary uses a modified form of the LWS method without any auxiliary domain

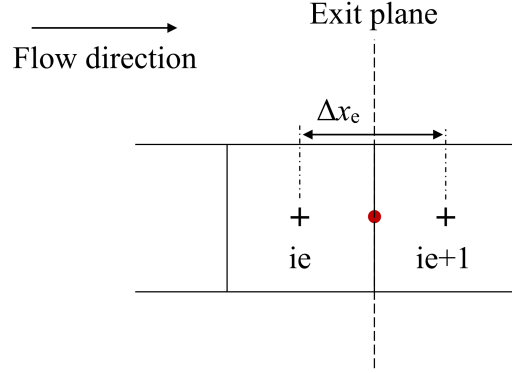


Figure 5.4: Schematic of control volumes at the exit plane.

to generate realistic turbulence, and the wall-normal velocity is also rescaled. A Heaviside function is applied to prevent unwanted fluctuations in the freestream region. Zero gradient conditions are used in the wall-parallel planes at the top boundary, and the wall-normal velocity is estimated using the growth of the displacement thickness. The exit boundary implements a convective boundary condition, and the time-averaged bulk velocity is used as the convective velocity at the outlet plane. These boundary conditions are employed in studying the TBL at different Reynolds numbers in the next chapter.

Chapter 6

Large Eddy Simulation of Zero Pressure Gradient Turbulent Boundary Layers

Turbulent boundary layers have important applications in engineering and meteorological problems: for example, the friction drag on an object or the study of the heat and mass transfers between the atmosphere and ground. Although many surfaces are curved and often rough, the spatially developing TBL over a smooth flat plate is an important benchmark study. The most crucial aspect of simulating a TBL is to provide realistic boundary conditions. This chapter considers the simulation of a fully developed TBL over a smooth flat plate for a range of Reynolds numbers from $Re_\theta = 2037$ to $Re_\theta = 25\,523$. A rescaling inflow generation method is used to provide realistic turbulence at the inlet.

The first section of this chapter uses a wall-resolved TBL to evaluate the performance of a recycling rescaling inflow generation method at a moderate Reynolds number. Different features of turbulent boundary layers, such as the skin-friction coefficient and shape factor, are compared with experimental studies. Next, the dynamic non-equilibrium wall-modeling is applied to a TBL at the same Reynolds number but with a lower grid resolution giving a lower computational cost. Then, the Reynolds number is increased to study the flow characteristics of high Reynolds number boundary layers using a coarse grid. The results will show the ability of wall-modeling to predict essential features of TBLs and reduce the computational cost.

6.1 Computational Set-up

The computational domain implemented for the simulation of a wall-resolved TBL is $10\delta \times 3\delta \times \frac{\pi}{2}\delta$ ($L_x \times L_y \times L_z$) in the streamwise, wall-normal, and spanwise directions, respectively, where δ is the boundary layer thickness at the inlet station. The recycling station is located at 8δ downstream of the inlet and sufficiently far from the exit plane to avoid any contamination from the outflow boundary. A uniform grid is used in wall-parallel planes with a resolution of $\Delta x^+ \simeq 71$ and $\Delta z^+ \simeq 25$ upstream of the flow domain in the streamwise and spanwise directions, respectively. A non-uniform grid distribution in the wall-normal direction locates the first node at $y_1^+ \simeq 1.2$ and gives $\Delta y_{\max}^+ \simeq 36$ at the top boundary as shown in Table 6.1. The no-slip boundary condition is applied at the wall, and the flow is periodic in the spanwise direction. The LWS inflow generation method generates realistic turbulence at the inlet. At the top boundary, zero-gradient velocity boundary conditions are used for the streamwise and spanwise directions, and the wall-normal velocity is obtained based on the streamwise development of the displacement thickness as discussed in Table 5.1, which conserves mass in the computational domain (Lund et al., 1998). Convective boundary conditions are employed at the exit plane as discussed in Section 5.3.2. To begin the simulation, initial velocities are prescribed using Eq. 4.1 for the mean streamwise velocity with random fluctuations. A Courant number of $\text{CFL} = 0.5$ is used to prevent numerical instabilities. The simulation is run for $190\delta/U_\infty$ to eliminate any initial transients. The mean flow characteristics such as the momentum thickness θ in the recycling rescaling inflow generation method or the displacement thickness δ^* in the boundary conditions at the top of the computational domain are estimated using empirical correlations, i.e. $\delta/x = 0.37/\text{Re}_x^{1/5}$ and $U/U_\infty = (y/\delta)^{1/7}$ (Schlichting and Gersten, 2017). These parameters, after the flow statistics are recorded for $300\delta/U_\infty$, are obtained directly from the mean flow field using $\delta^* = \int_0^\infty (1 - U/U_\infty)dy$ and $\theta = \int_0^\infty (U/U_\infty)(1 - U/U_\infty)dy$.

In the wall-modeled test cases, the grid resolution and the size of the computational domain change according to the specifications presented in Table 6.1. The matching point in all cases is located in the log law region and above the first grid point in the LES domain. Thirty grid points in the wall-normal direction are employed to resolve the wall-layer using the dynamic non-equilibrium wall model of Park and Moin (2014) in all test problems except test case 5 which used 50 grid points. These grid points have a non-uniform distribution in the wall-normal direction while the grid resolution in the wall-parallel planes is the same as in the LES domain. The recycling station in the last two test problems moves to 12δ downstream of the inlet plane to ensure robust input for the inlet turbulence generation. The Courant

Table 6.1: Computational specifications for flat plate turbulent boundary layer simulations.

Test Problem	1	2	3	4	5
	Wall-resolved		Wall-modeled		
Re_θ	2496-2930	2037-2996	7449-8833	11 906-13 565	22 060-25 523
Re_τ^\dagger	1130	939	3150	4275	8535
Re_δ^\dagger	27 180	23 025	86 400	123 750	259 050
$Re_{\delta^*}^\dagger$	3656	3449	12 941	18 535	38 800
L_x, L_y, L_z	$10\delta, 3\delta, \frac{\pi}{2}\delta$	$10\delta, 3\delta, 2\delta$		$15\delta, 4\delta, 2\delta$	
$n_x \times n_y \times n_z$	$144 \times 64 \times 64$	$128 \times 48 \times 32$	$160 \times 48 \times 32$	$256 \times 64 \times 48$	$384 \times 64 \times 48$
$\Delta x^+, \Delta y_{\max}^+, \Delta z^+$	71, 36, 25	75, 81, 59	182, 247, 180	230, 335, 163	296, 1475, 315
y_1^+	1.2	15	46	62	49
N_m	-	5 th	5 th	4 th	5 th
h_{wm}^+	-	139	422	427	455
$\delta t^+ (\delta t u_\tau^2 / \nu)$	0.197	0.494	0.485	0.937	1.835

† : At recycling station

N_m : Location of the matching point in the LES domain

h_{wm}^+ : Height of the wall layer

number is also reduced to $\text{CFL} = 0.3$ in the LES domain, and with a $\text{CFL} = 15$ in the wall layer. Time averaging and temporal filtering schemes, which were discussed earlier in Sections 3.3.3 and 4.5.3, are implemented in the wall-modeling with $T_F = 1.0$ and $T_W = 0.1$ values to ensure a responsive wall layer.

6.2 Wall-resolved Boundary Layer at $\text{Re}_\theta = 2710$

The performance of the inflow generation method is initially studied in a wall-resolved TBL. First, two probes at the inlet plane tracked the instantaneous streamwise velocity inside the wall layer ($y/\delta = 0.035$) and the freestream region ($y/\delta = 2.0$). The results are shown in Fig. 6.1 where the velocities are normalized by the freestream velocity and the time advancement is normalized by the convective time scale. The upper profile indicates approximately zero fluctuations after $T = 40$ whereas the lower one shows high-frequency fluctuations after $T = 25$ which depicts turbulence. Recall that the probes are located at the inlet plane, and a finite time is required for the turbulent flow at the inlet boundary to approach the exit plane and generate a fully developed TBL. To ensure fully developed turbulence, the simulation is initially advanced for $130\delta/U_\infty$ to eliminate the effects of starting transients as suggested by Urbin and Knight (2001) for a similar flow geometry. Once the flow is stabilized, the flow statistics are collected for $520\delta/U_\infty$ to achieve the following results.

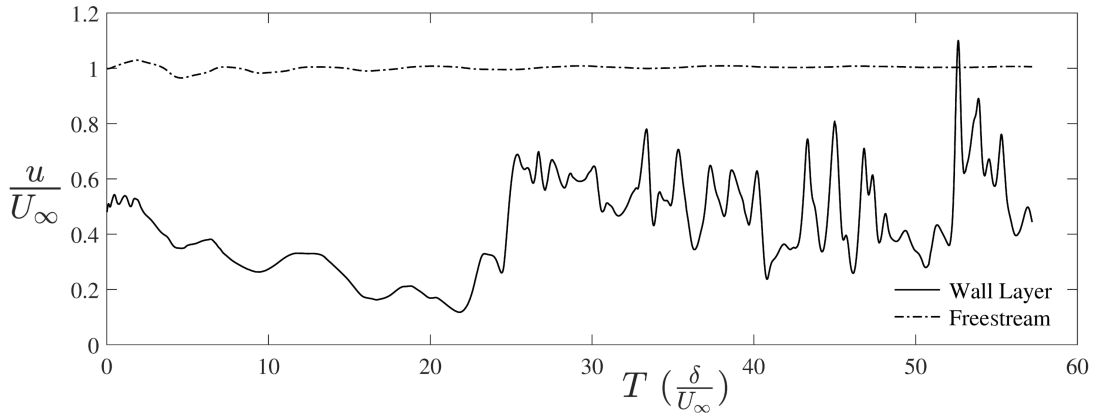


Figure 6.1: Time series of streamwise velocity in the wall layer at $y/\delta = 0.035$ ($y^+ \approx 31$) and in the freestream region at $y/\delta = 2.0$.

The mean velocity profile at the recycling station of the wall-resolved boundary layer is shown in Fig. 6.2. Inner coordinates are used to compare the streamwise velocity with experimental references in Fig. 6.2a. The DNS study of Rai and Moin (1993) and Spalart

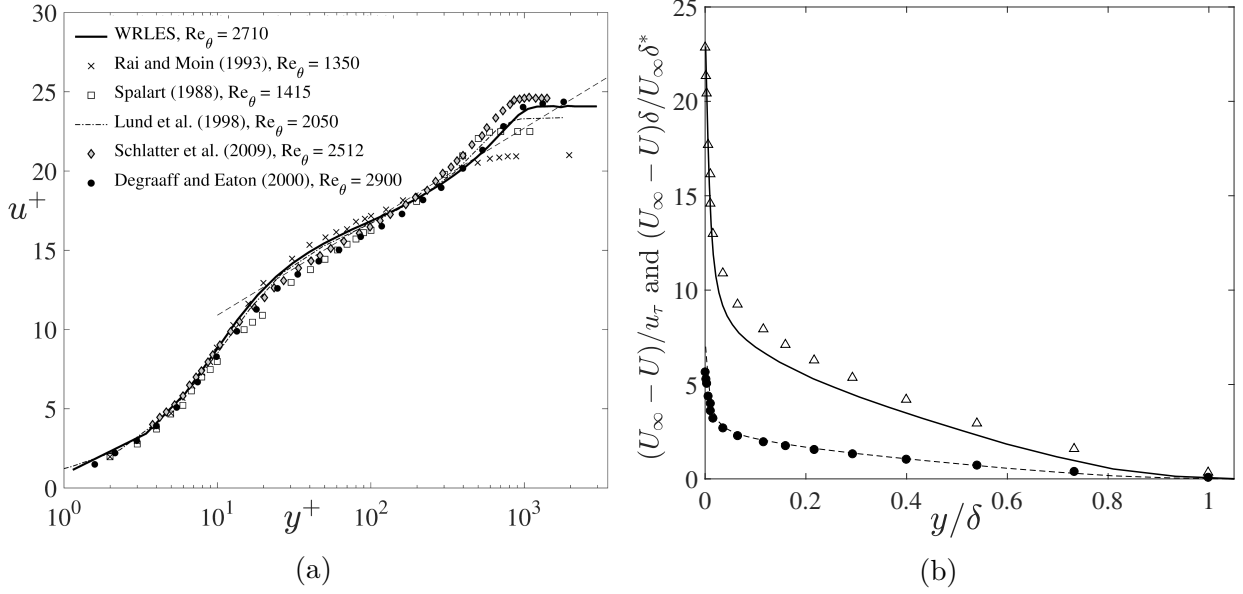


Figure 6.2: Mean velocity profiles for the wall-resolved boundary layer at $Re_\theta = 2710$ in (a) inner coordinates, and (b) defect formulation (WRLES: solid line, $(U_\infty - U)/u_\tau$; WRLES: dashed line, $(U_\infty - U)\delta/U_\infty\delta^*$; Degraaff and Eaton (2000): \triangle , $(U_\infty - U)/u_\tau$; Degraaff and Eaton (2000): \bullet , $(U_\infty - U)\delta/U_\infty\delta^*$).

(1988) are shown for a better comparison. All profiles follow each other closely in the near-wall region. Moving to the buffer region, the WRLES profile shows an over-prediction, which implies a low grid resolution in resolving the flow structures and under-estimation in modeling the subgrid scales. However, it improves when moving towards the logarithmic region. A clear wake region is observed before approaching the freestream flow. The WRLES profile at $Re_\theta = 2710$ follows closely the experimental data of Degraaff and Eaton (2000) at $Re_\theta = 2900$, whereas the results of Schlatter et al. (2009) indicate higher values for a lower Reynolds number at $Re_\theta = 2512$. The scale of the flow dynamics in the outer layer is characterized by the global flow properties such as the boundary layer thickness δ and freestream velocity U_∞ . Hence, Fig. 6.2b presents the mean velocity profiles in terms of the velocity defect law, i.e. $(U_\infty - U)/u_\tau$, as a function of y/δ together with the experimental data of Degraaff and Eaton (2000). The WRLES and experiment are not quite identical throughout the boundary layer; however, they display similar trends. In a similar study presented by Wu and Moin (2009) to compare the DNS results of a TBL with experimental data, under-estimation was observed for the DNS velocity defect profile analogous to what is shown in Fig. 6.2b. They proposed a modified scaling law of Zagarola et al. (1998), which yielded self-similar profiles with a better collapse in most regions. Hence, the mean velocity in the modified scaling law, i.e. $(U_\infty - U)\delta/U_\infty\delta^*$, is also presented. The mean velocity profile is qualitatively similar to the experimental data of Degraaff and Eaton (2000).

The velocity fluctuations and Reynolds shear stress across the boundary layer are shown in Fig. 6.3 and compared with the numerical study of Lund et al. (1998) for a wall-resolved boundary layer at $Re_\theta = 2050$ and the experimental study of Degraaff and Eaton (2000) at $Re_\theta = 2900$. The shear stress, $\overline{u'v'}^+$, indicates good agreement with the experimental and numerical data. The predictions for the velocity fluctuations (u'_{rms}^+ , v'_{rms}^+ , and w'_{rms}^+) in the wall layer show similar trends with the results of Lund et al. (1998) and are close to the experimental values. The peak of the streamwise velocity fluctuation, u'_{rms}^+ , has the value of 3.5 whereas the experiment indicates 2.8, both at the same location $y/\delta = 0.012$. One can infer that the grid resolution in the streamwise direction is lower than the requirements of the LES, which results in a poor prediction of u'_{rms}^+ . In contrast, the wall-normal velocity fluctuation, v'_{rms}^+ , which is obtained for a fine mesh near the wall, matches the profile of Lund et al. (1998). The wall-parallel grid resolution in this study is $\Delta x^+ = 71$ and $\Delta z^+ = 25$ while Lund et al. (1998) implemented $\Delta x^+ = 64$ and $\Delta z^+ = 15$. The spanwise velocity fluctuation, w'_{rms}^+ , compares well with the other numerical studies; no experimental data were measured by Degraaff and Eaton (2000). The profiles for u'_{rms}^+ , v'_{rms}^+ , and w'_{rms}^+ approach the experimental data in the region $0.1 < y/\delta < 0.4$ with a small under-prediction. The WRLES profiles closely follow the other numerical results and give a slightly better prediction at $y/\delta = 1$.

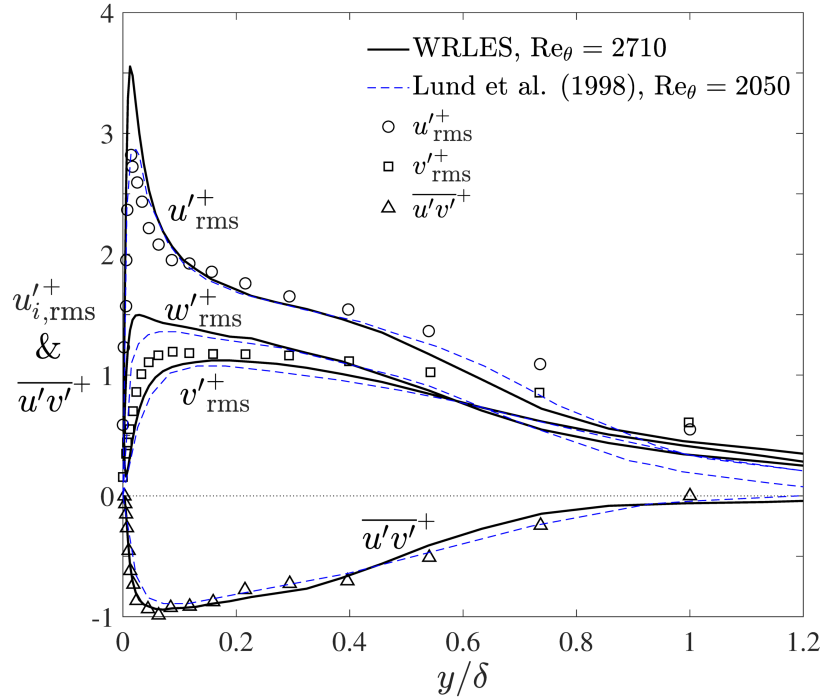


Figure 6.3: Velocity fluctuations and Reynolds shear stress in the wall-resolved TBL at $Re_\theta = 2710$; symbols: experiment by Degraaff and Eaton (2000) at $Re_\theta = 2900$.

Two parameters that describe a fully developed boundary layer are shown in Fig. 6.4. The shape factor $H = \delta^*/\theta$, which represents the prediction of displacement thickness and momentum thickness, is shown as a function of the Reynolds number based on momentum thickness in Fig. 6.4a. The displacement thickness and momentum thickness are estimated using the integral definitions as discussed in Section 6.1. Two LES studies by Lund et al. (1998) and Schlatter et al. (2009) are also presented. The results of the WRLES are similar to those of Lund et al. (1998); both studies under-predict the shape factor in comparison to the experiment of Österlund (1999). The results of Schlatter et al. (2009) show less deviation due to a grid resolution that is roughly three times higher than for the other numerical simulations. Fig. 6.4b presents the skin-friction coefficient as a function of Reynolds number. A short region upstream and a small section downstream of the flow domain are excluded due to the numerical errors in applying the boundary conditions at the inlet and exit planes. The qualitative trend of the WRLES shows good agreement with the experimental studies. The skin friction depends directly on the wall shear stress, which relates to the grid resolution near the wall region. The first node that is used to estimate the wall shear stress ($\tau_w = \mu dU/dy$) is located inside the viscous sub-layer at $y_1^+ = 1.2$.

To further examine the performance of the recycling rescaling method, the scaling factor γ given in Eq. 5.5 is compared with empirical correlations. The power-law exponent λ is

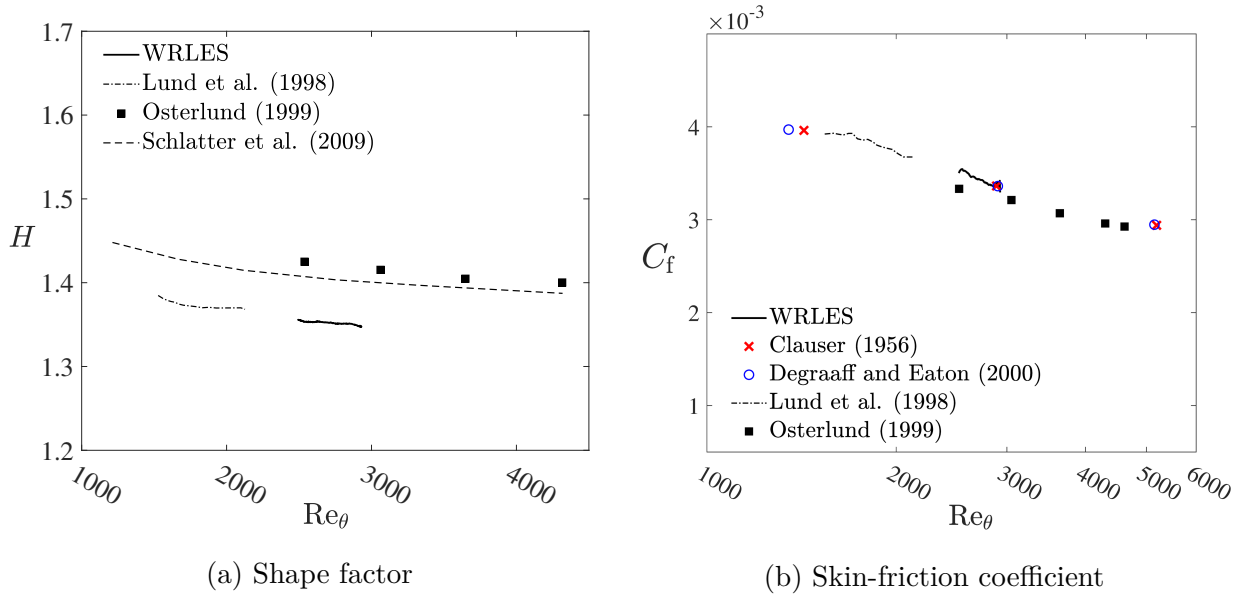


Figure 6.4: Characteristics of the mean velocity for the wall-resolved boundary layer at moderate Reynolds numbers.

presented for ZPG boundary layers as follows (Araya et al., 2011):

$$\lambda = \frac{\ln \left(\frac{u_{\tau, \text{inlt}}}{u_{\tau, \text{recy}}} \right)}{\ln \left(\frac{\delta_{\text{inlt}}}{\delta_{\text{recy}}} \right)}, \quad (6.1)$$

where the ratio in the numerator, which represents the scaling factor, can be obtained by calculating the momentum thickness from the mean solution at the inlet and recycling stations using Eq. 5.15. A time series of the power-law exponent is shown in Fig. 6.5, where $T = t/t_v$ is the dimensionless time advancement of the simulation. It is observed that the computed λ varies mildly around a value of -0.125 while stronger local fluctuations are indicated. The value of -0.125 can be obtained using the classical empirical correlation proposed by White (2006) for the friction velocity as $u_\tau/U_\infty \sim \text{Re}_\delta^{-0.125}$. However, the power-law exponent depicted in Fig. 6.5 varies in a narrower range compared to the results of Araya et al. (2011), who implemented a dynamic approach in generating inflow turbulence. Recall that the friction velocity and boundary layer thickness are two main parameters to rescale the velocity components, and Fig. 6.5 indicates that the rescaling is in accordance with the empirical correlation.

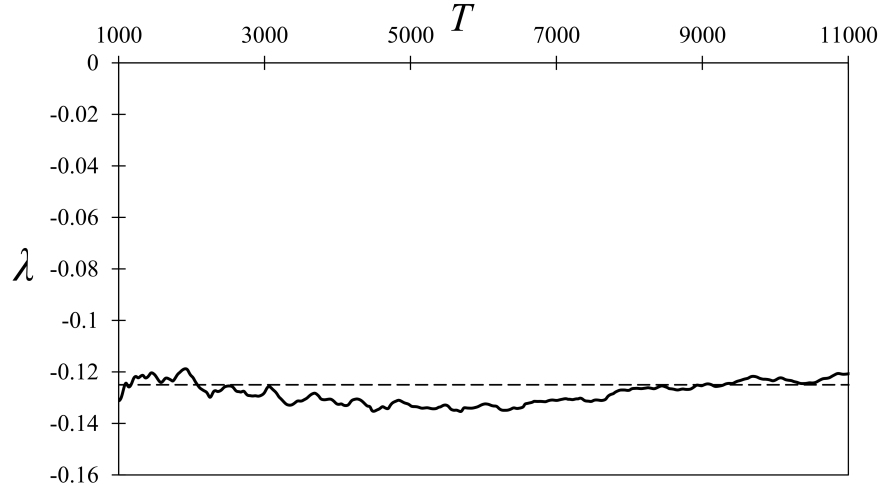


Figure 6.5: Variation of the power-law exponent λ (solid line) in comparison with the empirical value (-0.125 , dashed line) in a spatially developing ZPGTBL.

6.3 Sensitivity to Grid Resolution

The transition from a WRLES to a WMLES is a challenging process due to coarse grid used near the wall. Additional challenges are encountered in the simulation of turbulent boundary layers related to the boundary condition at the outlet and inflow turbulence generation. One challenge is unphysical numerical oscillations in CFD simulations. Fig. 6.6a shows undesirable streamwise oscillations in the freestream region when the grid points used in the wall-resolved TBL (Section 6.2) are reduced to $96 \times 48 \times 32$ at the same Reynolds number. A probe was used to track the instantaneous streamwise velocity at the spanwise center of the computational domain near the edge of the boundary layer. Fig. 6.6c shows the time variation of velocity normalized by the mean velocity. A sinusoidal acceleration-deceleration is observed at a higher frequency, which is superimposed on low-frequency oscillations. These oscillations emerge when a coarse grid and the non-dissipative central-difference scheme are employed (Xu and Yang, 2021). There are different methods to avoid these numerical instabilities such as using upwind schemes or artificially increasing the viscosity. However, the most straightforward solution is grid refinement in regions of rapid flow acceleration or deceleration (Sabau and Raad, 1999).

Grid refinement was initially applied at the outlet region by adding 16 additional layers of control volumes. These control volumes are fitted in a short region downstream, which

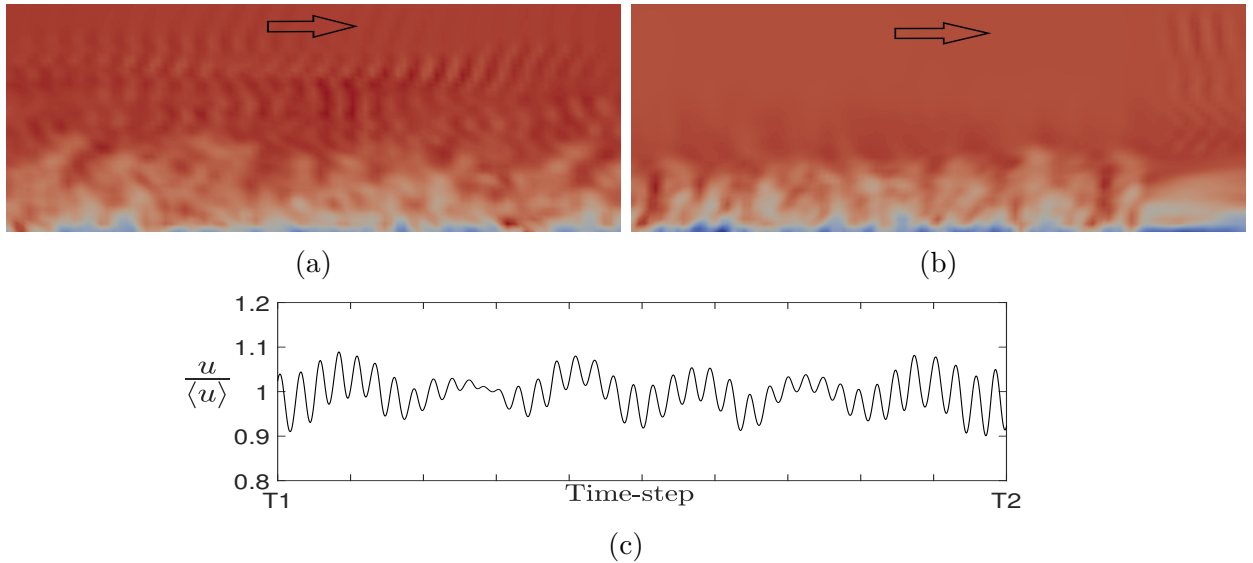


Figure 6.6: Instantaneous velocity contours on a control vertical plane in a WRLES boundary layer using a coarse grid with (a) streamwise unphysical oscillations, (b) oscillations at the outflow region, and (c) time variation of streamwise velocity near the edge of the boundary layer.

approximately occupy one percent of the length of the flow domain. The results are presented in Fig. 6.6b. It is observed that the streamwise oscillations disappear in most regions and persist only in the outflow region. This implies that the numerical solution is sensitive to the outlet boundary when too coarse a grid is implemented. Xu and Yang (2021) suggested using one refined layer of grids at the critical boundary, such as the outlet boundary. However, one refined layer in the current computational domain was insufficient to improve the oscillation issue. Hence, two layers of grid points with one fifth of the grid resolution defined for the flow domain in the streamwise direction were added to the outflow boundary region to remove the unphysical numerical oscillations. This grid refinement is applied to all the wall-modeled LES turbulent boundary layers in the following sections to avoid numerical instabilities.

6.4 Wall-modeled LES of Turbulent Boundary Layers at $Re_\theta = 2037 - 25\,523$

Wall-modeling promises to reduce the computational cost of numerical solutions. This section begins with calculations of the same TBL as discussed in Section 6.2 but using the wall-modeling methodology and a lower number of grid points. As presented in Table 6.1, the number of grid points decreases from 589 824 ($144 \times 64 \times 64$) nodes in the wall-resolved boundary layer to 196 608 ($128 \times 48 \times 32$) control volumes in a wall-modeled boundary layer, which represents a 66% reduction. Note that the WMLES needs only 1% of the control volumes that were used in the DNS study of Schlatter et al. (2009) for a similar Reynolds number and flow domain. The mean velocity profile of the WMLES turbulent boundary layer at $Re_\theta = 2620$ is shown in Fig. 6.7 using inner coordinates. An over-prediction is observed for the velocities below the matching point, i.e. the 5th node, similar to the wall-modeled turbulent channel flows demonstrated in Fig. 4.9. However, the prediction improves when moving towards the logarithmic region, and a clear wake region is observed in the outer layer adjacent to the freestream.

To further evaluate the WMLES, the Reynolds number was increased to higher values. For the same computational domain and grid points, the Reynolds number was increased to $Re_\theta = 8400$, which represents one third of the grid resolution used for test problem 2 as shown in Table 6.1. There are no numerical or experimental results for a WRLES turbulent boundary layer at the same Reynolds number to the knowledge of the author. The highest Reynolds number in the literature pertains to Schlatter et al. (2010) at $Re_\theta = 4300$, which used 37 million grid points for a similar size of flow domain. In contrast, the WMLES uses

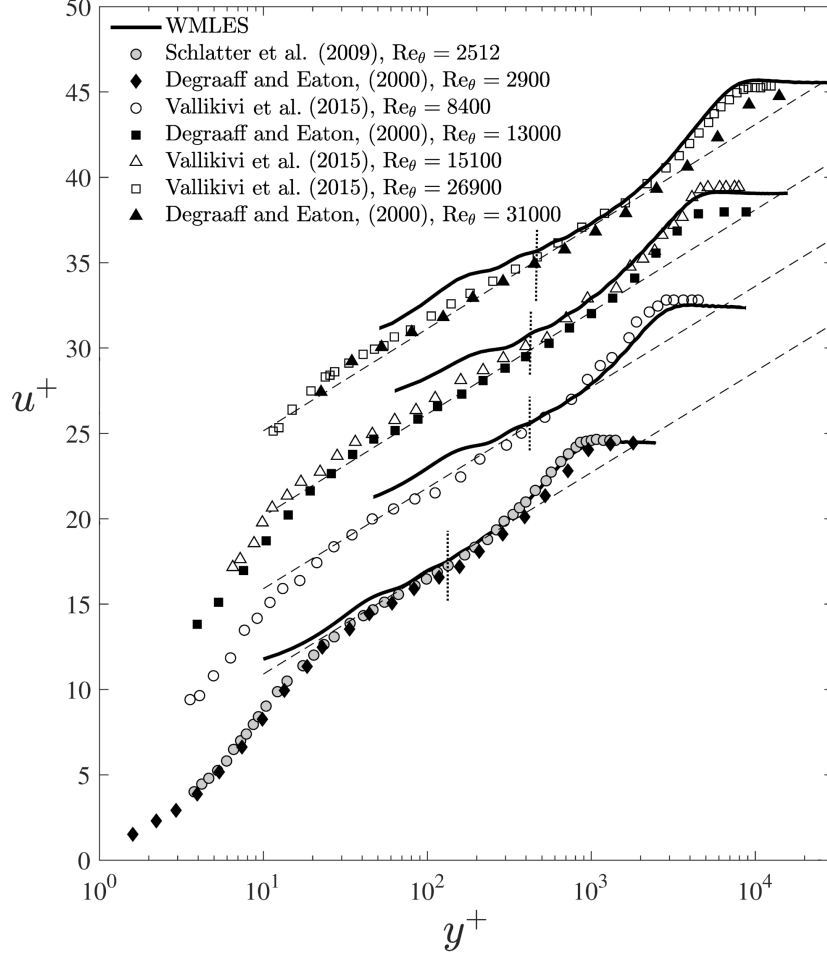


Figure 6.7: Mean velocity profiles of TBLs using inner coordinates, WMLES: solid lines, at $Re_\theta = 2620, 8400, 13100$, and 24500 from bottom to top; experiments: symbols; log law [$\kappa = 0.39$ and $B = 5.0$ for the two bottom profiles and $\kappa = 0.384$ and $B = 4.17$ for the two top profiles (Nagib and Chauhan, 2008)]: dashed line. Dotted lines show the location of the corresponding matching point. The profiles are shifted with increments of five units for clarity.

less than 1% of the grid points at twice the Reynolds number. In general, a good prediction of the mean velocity profile is presented. However, a slight under-prediction is observed in the outer region and above the matching point, which is located at $y^+ = 422$.

Next, the length of the computational domain was increased to 15δ to reduce the risk of contaminating the solution with errors associated with the inflow generation approach at the inlet plane for higher Reynolds numbers. A wall-modeled TBL at $Re_\theta = 13100$ was simulated in test problem 3. The velocity profile follows the experimental results of Vallikivi et al. (2015) at $Re_\theta = 15100$, although it over-predicts the experimental data of Degraaff

and Eaton (2000) at $Re_\theta = 13\,000$. Note that the grid resolution remains approximately constant compared to the grid resolution of test case 2. The log law profile suggests the experimental profile of Vallikivi et al. (2015), which was obtained using nanoscale anemometry probes with an uncertainty lower than 2.2%, is in better agreement with the solution of the WMLES turbulent boundary layer. In the last test problem (number 4), a TBL was simulated at $Re_\theta = 24\,500$. The grid resolution in wall coordinates is one half of the previous test case. An under-prediction for the experimental results of Degraaff and Eaton (2000) is again observed in the outer region although the corresponding Reynolds number is higher than the Reynolds number of Vallikivi et al. (2015). The WMLES profile closely matches the experimental data of Vallikivi et al. (2015) at $Re_\theta = 26\,900$. Fig. 6.7 demonstrates the performance of wall-modeling is reliable across a range of Reynolds numbers in terms of the mean velocity field.

Fig. 6.8 shows the mean defect profile using outer coordinates and the modified scaling law for different Reynolds numbers. The numerical results are compared with the measurements of Degraaff and Eaton (2000) over a wide range of $2620 < Re_\theta < 31\,000$. The mean velocities for the WMLES display identical trends as those of the experimental data and are well

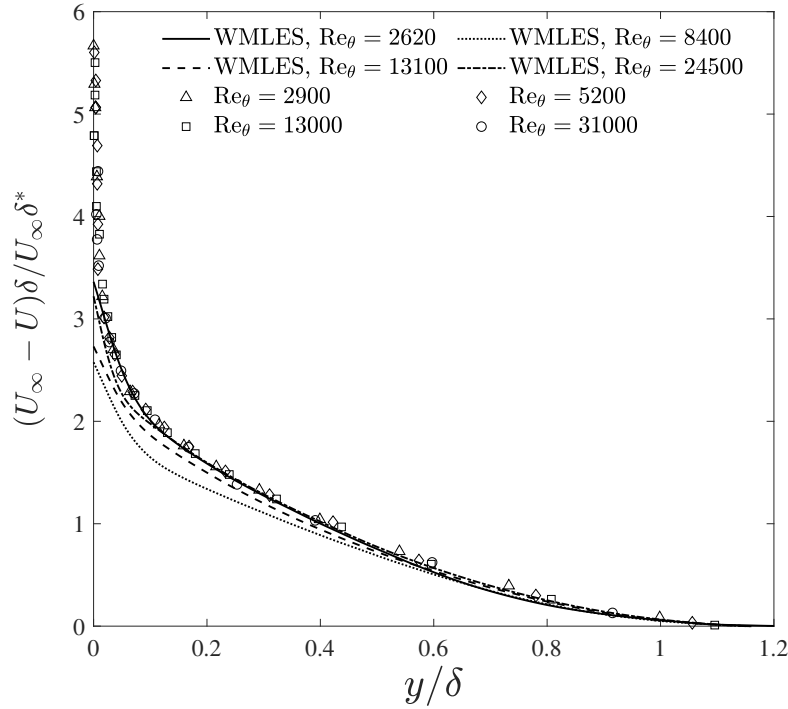


Figure 6.8: Mean velocity profiles in deficit coordinates for wall-modeled turbulent boundary layers. experiments: symbols (Degraaff and Eaton, 2000).

collapsed across the outer region of the boundary layer. Self-similarity is observed between the experimental and numerical profiles in the outer region. However, the mean defect profile is under-predicted close to the wall for test problem 3 at $Re_\theta = 8400$. A plausible reason is the inaccurate estimation of the displacement thickness δ^* using a coarse grid near the wall. The mean velocities at the very first nodes near the wall show higher deviations from the experimental data in contrast to the mean velocities at $Re_\theta = 13\,100$ and $Re_\theta = 24\,500$, which significantly affect the estimation of an accurate mean velocity deficit, i.e., $(U_\infty - U)\delta/U_\infty\delta^*$. The mean velocity U was evaluated earlier in Fig. 6.7, and no over-prediction was observed. The role of δ and δ^* becomes less significant when moving towards the outer region since $U_\infty - U$ approaches zero. This issue is also observed at $Re_\theta = 13\,100$ and $Re_\theta = 24\,500$. However, using denser control volumes inside the boundary layer at test problems 4 and 5 improves the estimation of δ and δ^* .

The WMLES is incapable of calculating the skin-friction coefficient C_f given the von Karman integral momentum equation, i.e. $C_f/2 = d\theta/dx$. Obtaining θ based on the mean velocity profile obtained from the LES domain results in inaccurate values due to the low grid resolution near the wall. Instead, the wall-modeling circumvents this by directly applying the wall shear stress from a resolved wall layer. In this regard, the skin-friction coefficient for the test problems is presented in Fig. 6.9 as a function of the Reynolds number based on momentum thickness. Experimental data are also presented at different Reynolds numbers for comparison. There are different correlations to empirically estimate the skin-friction coefficient (Nagib et al., 2007). The Cole-Fernholz relation which is a best-fit to the logarithmic

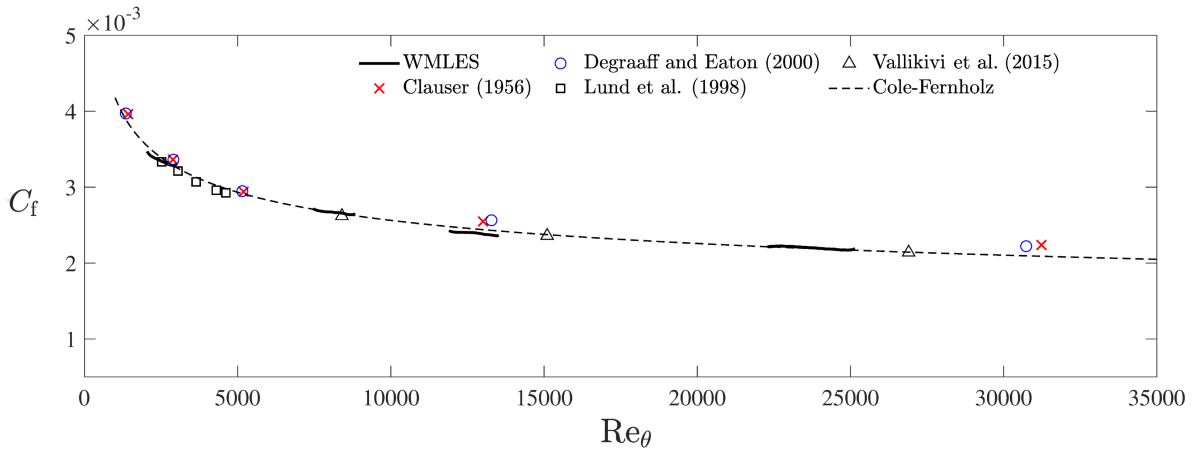


Figure 6.9: The skin-friction coefficient as a function of Reynolds number based on momentum thickness for high-Reynolds number turbulent boundary layers using wall-modeling.

law is employed in this study,

$$C_f = 2[1/\kappa \ln(\text{Re}_\theta) + C]^{-2}, \quad (6.2)$$

where $\kappa = 0.384$ and $C = 4.127$. The results for the WMLES turbulent boundary layers are shown using solid lines over discrete ranges of Reynolds numbers. All profiles are in good agreement with the Cole-Fernholz correlation and the experimental data. Recall that the skin-friction coefficient is representative of the wall shear stress τ_w in the wall layer, which demonstrates the ability of wall-modeling to predict τ_w as a boundary condition for the LES.

6.5 Study of a High-Reynolds Number Wall-modeled Turbulent Boundary Layer at $\text{Re}_\theta = 24\,500$

The performance of wall-modeling is better at a higher Reynolds number as discussed earlier in the simulation of turbulent channel flows. Hence, the TBL at $\text{Re}_\theta = 24\,500$ is further studied in this section. Approximately 50 grid points are used inside the boundary layer to resolve the essential flow structures ($n_y/\delta = 40$). The density of grid points in the wall-parallel planes are $n_x/\delta = n_z/\delta \approx 25$, which is comparable to that of Park and Moin (2014) and Kawai and Larsson (2012). Fig. 6.10 presents the mean velocity profiles in inner coordinates and outer coordinates. The experimental data of Vallikivi et al. (2015) at $\text{Re}_\theta = 26\,900$ and Degraaff and Eaton (2000) at $\text{Re}_\theta = 31\,000$ are included for comparison. Experimental data of Souverein et al. (2010) at $\text{Re}_\theta = 50\,000$ and the numerical results of Park and Moin (2014) at $\text{Re}_\theta = 31\,000$ and Kawai and Larsson (2012) at $\text{Re}_\theta = 50\,000$ are also presented for comparison. The matching point is shown by a vertical dotted line which is located at the fifth cell in the LES domain. The wall-modeling velocity profile is also presented using a dotted-dashed line; the mean velocity in the wall layer is well predicted as shown in Fig. 6.10a. The over-prediction of velocities below the matching point is a generic problem in WMLES solutions due to the poor performance of the SGS model in the wall layer where a coarse grid is employed. Above the matching point, the profile matches the experimental data of Vallikivi et al. (2015), which extends to the freestream region. A better prediction is observed in contrast to two other numerical results. The WMLES profile displays a wake region with the same qualitative trends as the experimental data of Vallikivi et al. (2015). Although there is a discrepancy between the WMLES profiles and those of Degraaff and Eaton (2000) and Vallikivi et al. (2015), the experimental study of Souverein et al. (2010) suggests that the prediction of the velocity in the wake region by the WMLES is reliable.

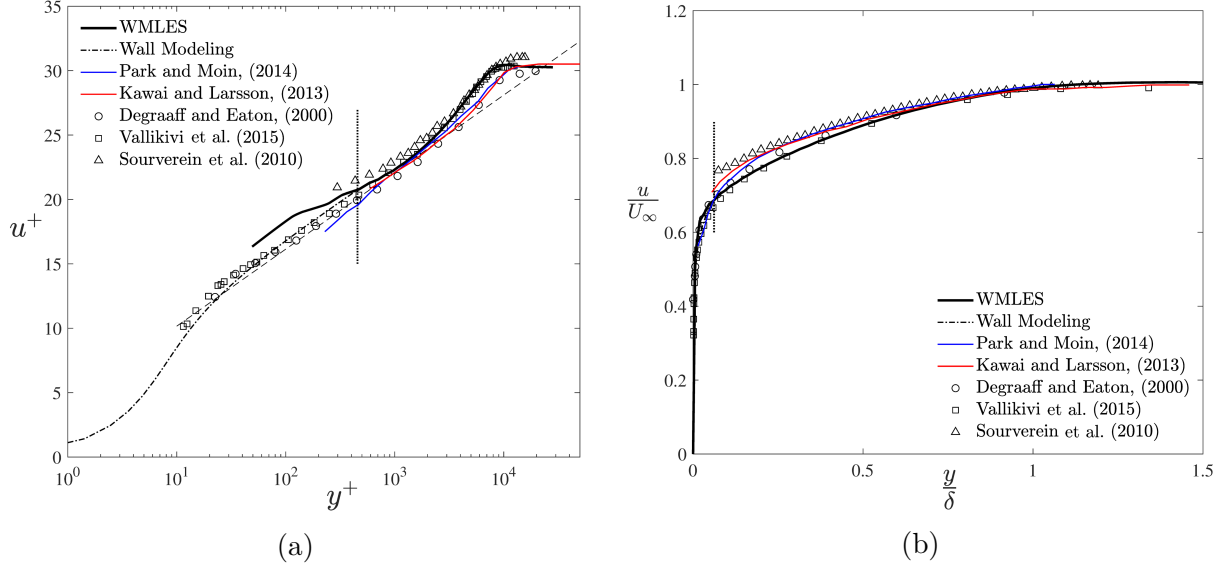


Figure 6.10: Mean velocity profiles in (a) inner coordinates and (b) outer coordinates for WMLES at $Re_\theta = 24\,500$, black solid line; log law ($\kappa = 0.384$, $B = 4.17$), dashed line; Park and Moin (2014) at $Re_\theta = 31\,000$, blue solid line; Kawai and Larsson (2013) at $Re_\theta = 50\,000$, red solid line; Degraaff and Eaton (2000) at $Re_\theta = 31\,000$, \circ ; Vallikivi et al. (2015) at $Re_\theta = 26\,900$, \square ; Souverein et al. (2010) at $Re_\theta = 50\,000$, \triangle .

Outer coordinates are implemented in Fig. 6.10b. The results collapse well in the outer region. The WMLES profile gives an under-prediction when moving towards the wall, but it matches the experimental data of Vallikivi et al. (2015).

The next set of profiles relates to the Reynolds shear stress and *rms* of velocity fluctuations in the high-Reynolds number wall-modeled TBL. The streamwise velocity fluctuation across the boundary layer is shown in Fig. 6.11a in outer coordinates. As expected, the WMLES profile shows a poor prediction in the near-wall region. Moving towards the outer edge of the boundary layer, a slight peak emerges in the range of $0.2 < y/\delta < 0.5$. This peak is different than the near-wall peak, which is invariant with Reynolds number and occurs at approximately $y^+ = 15$. The second outer peak appears in high Reynolds number TBLs and relates to outer phenomena (Marusic et al., 2010). Fig. 6.11b shows the inner and outer peaks of the fluctuating streamwise velocity in wall coordinates. Note that, given the wall-modeling using a coarse mesh near the wall, the inner peak is undetectable since the first cell is located far away from the traditional location for the inner peak, i.e. $y^+ = 15$.

The wall-normal velocity fluctuation is presented in Fig. 6.11c. A good prediction is observed for v'^+_{rms} , whereas an over-prediction is observed near the wall. Recall that the first cell near the wall in the WMLES is treated by a no-slip boundary condition even though

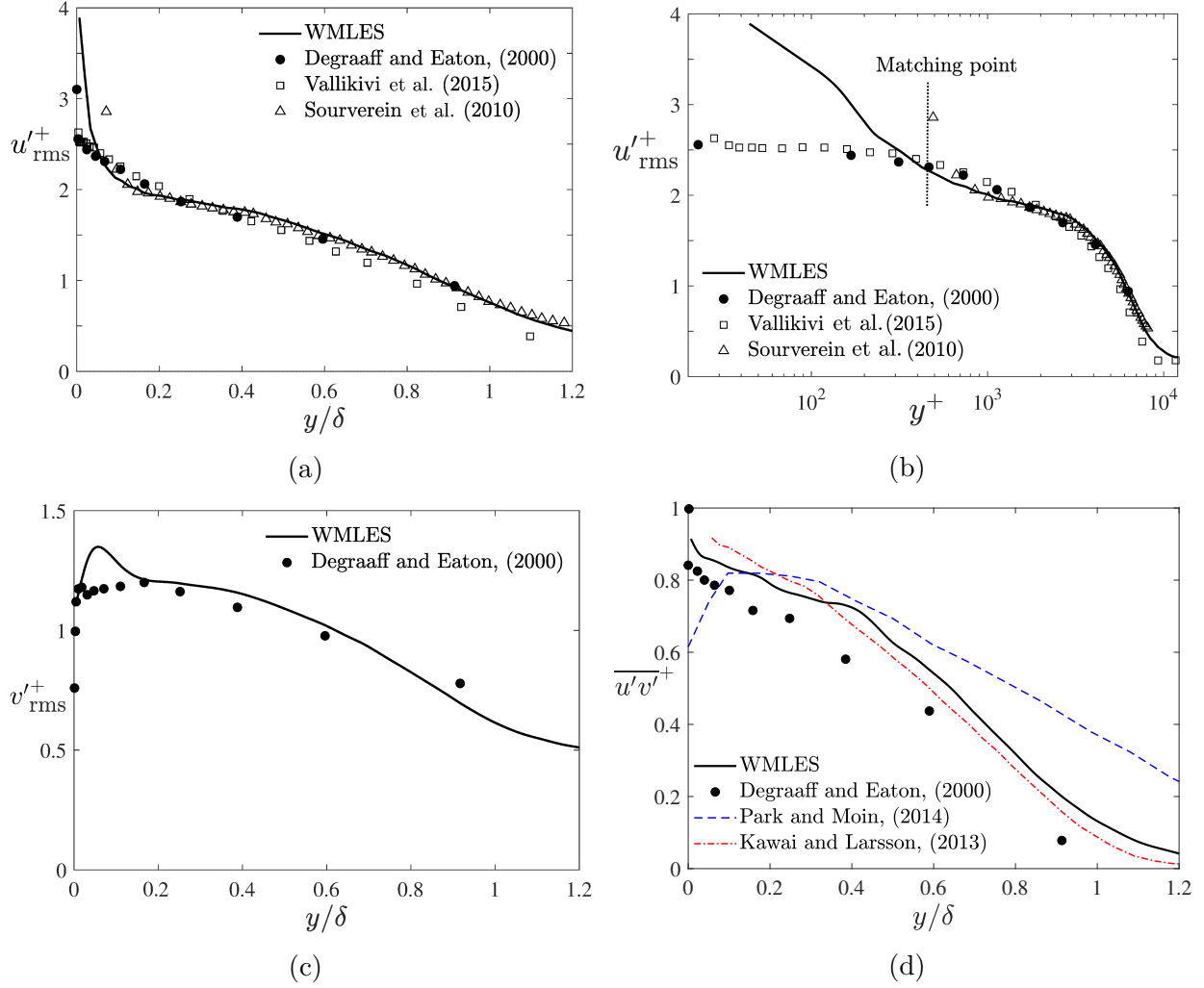


Figure 6.11: Velocity fluctuations and Reynolds shear stress in the wall-modeled TBL at $Re_\theta = 24\,500$: (a) streamwise velocity fluctuation in outer coordinates, (b) streamwise velocity fluctuation in inner coordinates, (c) wall-normal velocity fluctuation, and (d) Reynolds shear stress across the boundary layer. For details of experimental data (symbols) refer to Fig. 6.10.

it is outside the viscous sub-layer so that a linear velocity profile is incorrect. This leads to the over-prediction of v'_{rms}^+ observed in the range of $0 < y/\delta < 0.2$. However, the prediction improves for the logarithmic region. This issue is also manifest in the prediction of Reynolds shear stress $\overline{u'v'}^+$ in Fig. 6.11d. The WMLES over-predicts the Reynolds shear stress by 25% in the outer peak region near $y/\delta \approx 0.4$. A similar behavior was observed in the study of Kawai and Larsson (2013) and Park and Moin (2014) for wall-modeled TBLs at high-Reynolds numbers. The WMLES profile is closer to the experimental data near the wall. Some oscillations are observed in the region of $y/\delta < 0.6$, which relate to the low number of control volumes used inside the boundary layer. This issue improved in the numerical

study of Kawai and Larsson (2013), where they implemented denser grid points inside the boundary layer.

The total shear stress (τ) consists of the viscous shear stress ($\nu \frac{dU}{dy}$) and the Reynolds shear stress ($-\overline{u'v'}$). A plot of the three quantities is shown in Fig. 6.12 where they have been normalized using the wall shear stress τ_w . The total shear stress is approximately equal to the Reynolds shear stress over most of the boundary layer. The contribution of the viscous shear stress to the total shear stress is only significant for $y^+ < 200$. It is expected the turbulent and viscous stresses contribute equally to the total shear stress at $y^+ \approx 10$, where the maximum of turbulence kinetic energy production occurs (Rotta, 1962; Degraaff and Eaton, 2000). However, the grid refinement in the wall region is insufficient to resolve this crossing point. Some oscillations are observed in the total shear stress profile, which is attributed to using a low number of grid points to resolve the flow motions inside the boundary layer. Furthermore, the total shear stress should form a plateau near the wall, whereas both the experimental data and the WMLES profile show some variations. In general, the prediction for the shear stress is in good qualitative agreement with the experiment.

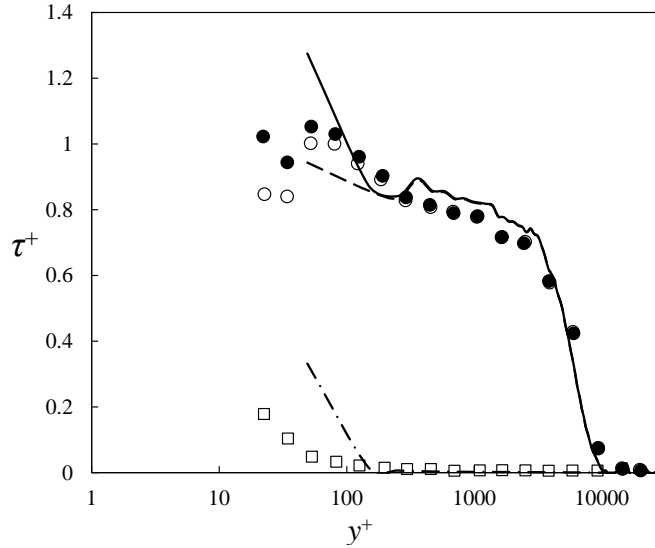


Figure 6.12: Total shear stress: solid line (experiment: ●), Reynolds shear stress: dashed line (experiment: ○), and viscous shear stress: dotted-dashed line (experiment: □) across the boundary layer compared to the experimental data of Degraaff and Eaton (2000).

The rate of energy production \mathcal{P} in the wall region is shown in Fig. 6.13, where it is normalized as $\mathcal{P}^+ = \mathcal{P}\nu/u_\tau^4$. Degraaff and Eaton (2000) stated that in the logarithmic region the production can be rewritten as follows assuming the total shear stress is approximately

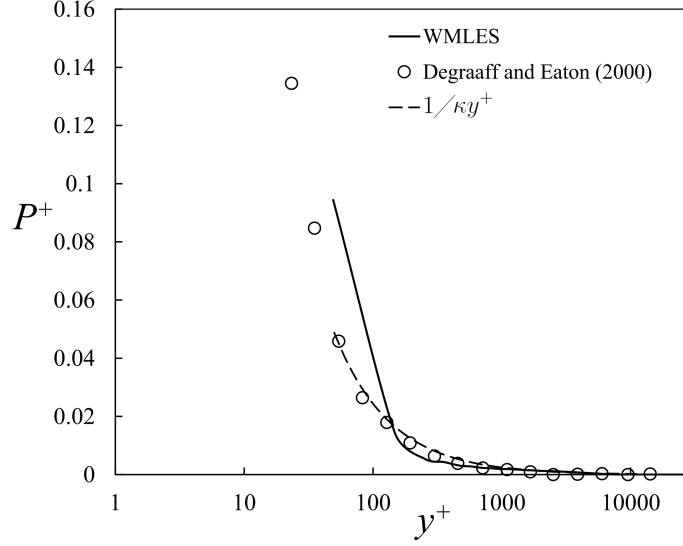


Figure 6.13: Turbulence kinetic energy production in the WMLES TBL at $Re_\theta = 24\,500$.

constant and equal to τ_w :

$$\begin{aligned}\mathcal{P} &= -\overline{u'v'} \left(\frac{dU}{dy} \right), \\ \mathcal{P}^+ &= \frac{\mathcal{P}\nu}{u_\tau^4} = -\overline{u'v'}^+ \left(\frac{dU^+}{dy^+} \right) = \frac{1}{\kappa y^+}.\end{aligned}\tag{6.3}$$

The line of $1/\kappa y^+$ is plotted using a dashed line and matches the experimental data of Degraaff and Eaton (2000) in the logarithmic region. The results of the WMLES and experimental data collapse well in the outer region. However, an over-prediction is observed for the first few control volumes near the wall as an inherent characteristic of wall-modeling. This deviation relates to the over-estimation of the Reynolds shear stress in the wall layer as shown earlier in Fig. 6.11d and the calculation of the mean velocity gradient on a coarse grid, which results in numerical errors in the discretization of dU/dy .

The final figures of this chapter consider the *rms* of velocity fluctuations and eddy viscosity inside the wall layer. The velocity fluctuations in Fig. 6.14a indicate similar behavior to the results of the turbulent channel flow presented in Fig. 4.13. The streamwise velocity fluctuation (u'_{rms}^+) is smaller than in the channel flow. Recall that the grid resolution in the x -direction used in the TBL is lower, which implies a smaller resolved velocity fluctuation. Both velocity fluctuations in the x - and z -directions (u'_{rms}^+ and w'_{rms}^+) evidence a rapid increase as they approach the matching point. Instead of using the TBLEs, which solve for the wall layer in the x - and z -directions, the wall-normal velocity is obtained using the continuity equation. Thus the wall-normal velocity fluctuation (v'_{rms}^+) indicates a different behavior.

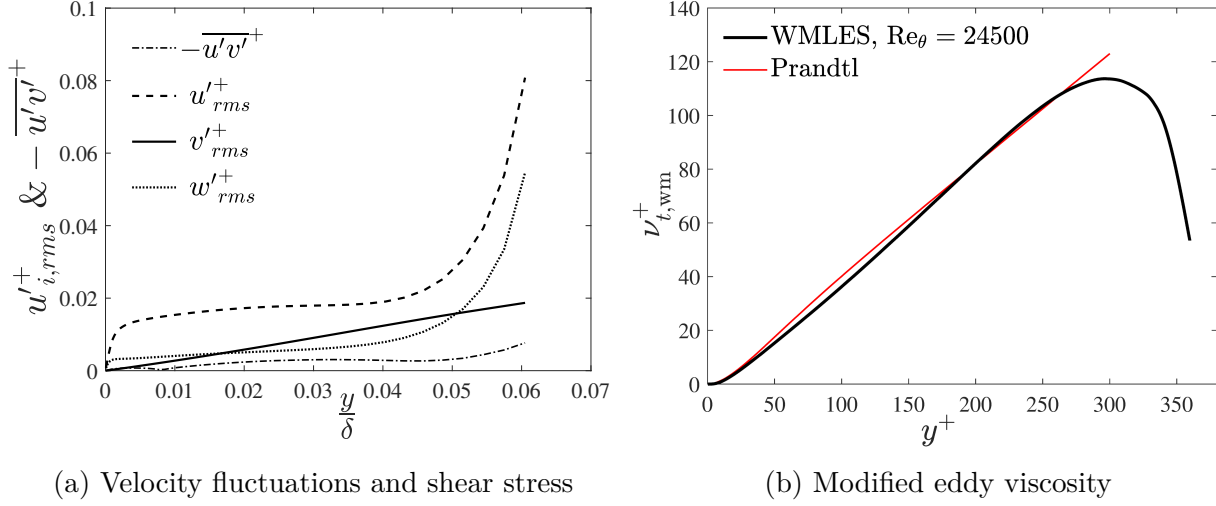


Figure 6.14: Flow characteristics across the wall layer in the WMLES TBL at $Re_\theta = 24\,500$.

This issue also affects the prediction of the Reynolds shear stress ($-\overline{u'v'}$) compared to the velocity fluctuations. Fig. 6.14b presents the modified eddy viscosity profile across the wall layer. Prandtl's mixing length hypothesis is employed to estimate the empirical eddy viscosity that is shown by a red line. A decrease is observed in the WMLES profile near the matching point as expected based on Eq. 3.25 since the Reynolds stresses (R_{ij}) increase, which is similar to the result of the wall-modeled channel flow shown in Fig. 4.14. This behavior is attributed to the dynamic non-equilibrium wall model accounting for the unresolved Reynolds stresses in the wall layer by reducing the eddy viscosity.

6.6 Conclusions

The recycling rescaling inflow generation method has been evaluated by the wall-resolved TBLs at moderate Reynolds number. Various flow characteristics including mean velocity profiles were studied and compared with experimental and numerical reference data. The mean streamwise velocity and *rms* of velocity fluctuations were shown across the boundary layer using different inner and outer coordinates. The results qualitatively matched experimental data in the viscous sub-layer, buffer region, and logarithmic region, although some discrepancies were observed. The variation of the skin-friction coefficient and shape factor as a function of momentum Reynolds number indicated acceptable performance at moderate Reynolds number. The turbulence kinetic energy production and viscous dissipation were compared with experiments and theoretical correlations, which confirmed the reliability of the WRLES. Furthermore, the rescaling inflow generation method was investigated based on

the variation of the power-law exponent over the simulation run-time. The results indicated the rescaling method is successful in generating realistic turbulence and a fully developed TBL, and the power-law exponent is consistent with the classical empirical correlation.

A grid refinement sensitivity of the wall-resolved TBL was studied prior to implementing the wall-modeling technique. It was found that two layers of grid points at the outlet boundary with a higher resolution minimize unphysical oscillations in the computational domain when a coarse mesh is implemented. This technique was used for the wall-modeled TBLs. The wall-modeled boundary layer was initially run at the same Reynolds number at the wall-resolved case. Next, test problems at higher Reynolds numbers with lower grid resolution indicated the performance of wall-modeling improves at high Reynolds numbers. To achieve self-similar profiles for the mean streamwise velocities, a modified scaling law was employed, and the velocity profiles collapse well over most regions. The prediction of the skin-friction coefficient improved at higher Reynolds numbers where the wall-modeling represented the flow dynamics near the wall. Further evaluations of the velocity fluctuations, Reynolds shear stress, and energy production were conducted on a wall-modeled TBL at $Re_\theta = 24500$. In general, the results of the WMLES turbulent boundary layers correctly predict the flow features in the outer region. However, as would be expected the LES predictions below the matching point are not accurate.

Chapter 7

Wall Stress Model with the Effects of Surface Roughness

7.1 Introduction to Roughness

Surface roughness has received sustained attention in many turbulent flows with engineering or geophysical applications. At first sight, roughness is a feature of the flow geometry which increases the drag force. However, it has some positive contributions in engineering problems such as delaying separation on an airfoil which reduces the drag force compared to a smooth surface (McMasters and Henderson, 1979). Although all surfaces have physical roughness in the real world, the effects of roughness can be neglected in some turbulent flows. To better understand surface roughness, a standard definition has been introduced to illustrate how roughness affects flow structures in the wall region.

Wall-bounded flows are characterized by two scaling parameters which are the kinematic viscosity ν and friction velocity u_τ (Raupach et al., 1991; Jimenez, 2004). The viscous length scale is obtained from these two parameters, i.e. $\delta_v = \nu/u_\tau$. Roughness affects the flow dynamics in the outer region when its length scale becomes comparable to the viscous length scale. Since the viscous length scale decreases with increasing Reynolds number, the effect of roughness is crucial in high Reynolds number flows. Given the equivalent roughness height k_s , a dimensionless roughness height is defined by

$$k_s^+ = \frac{k_s u_\tau}{\nu}, \quad (7.1)$$

which can be used to evaluate the effects of roughness elements on a flow. For insight into the methodology for estimating the equivalent roughness height, refer to the review of Jimenez (2004).

Recall that in the overlap region, the logarithmic law is defined as follows (Schlichting and Gersten, 2017):

$$\lim_{y^+ \rightarrow \infty} u^+(y^+) = \frac{1}{\kappa} \ln y^+ + C^+, \quad (7.2)$$

where C^+ is a constant of integration for smooth wall-bounded flows and a function of k_s^+ for rough surfaces. Hence, Eq. 7.2 can be written as

$$\begin{aligned} \lim_{y^+ \rightarrow \infty} u^+(y^+) &= \frac{1}{\kappa} \ln y^+ + C^+(k_s^+) \\ &= \frac{1}{\kappa} \ln \frac{y}{k_s} + C_r^+(k_s^+), \end{aligned} \quad (7.3)$$

where

$$C_r^+(k_s^+) = C^+(k_s^+) + \frac{1}{\kappa} \ln k_s^+. \quad (7.4)$$

Tani (1988) developed and evaluated Eq. 7.4 for different values of k_s^+ . He found that the function $C_r^+(k_s^+)$ is equal to the smooth wall value for $k_s^+ < 5$, and the drag is the same as over a smooth wall. As long as the roughness elements are below this limit, the flow is hydraulically smooth. In contrast, the limit of function $C_r^+(k_s^+)$ as k_s^+ approaches infinity is equal to 8.0. In such flows, the roughness elements fill up the entire wall layer, and the viscosity becomes less important. A flow with roughness elements $k_s^+ > 70$ is referred to as fully rough. Based on these limits, roughness is described by the following three regimes:

$$\begin{array}{ll} \text{hydraulically smooth:} & 0 \leq k_s^+ \leq 5, \quad C^+ \approx 5.0 \\ \text{transitionally rough:} & 5 < k_s^+ < 70, \quad C_r^+(k_s^+) \\ \text{fully rough:} & 70 \leq k_s^+, \quad C^+ \approx 8.0. \end{array}$$

Flow over rough surfaces was studied by Nikuradse (1950), who focused on the mean velocity shift ΔU^+ in the logarithmic profile. In general, the vertical shift in the mean velocity profile is expressed as a function of an effective roughness height, and the results obtained from experiments are used to estimate the hydrodynamic roughness length scale *a posteriori* (Anderson and Meneveau, 2011). In the numerical field of research, the effects of rough walls on the turbulent flow structures has been studied using DNS (Orlandi and Leonardi, 2008). However, the computational cost in resolving roughness elements becomes prohibitive at high Reynolds numbers. Reynolds-averaged models have been also modified to represent

the roughness effects on the mean flow field. In RANS methods, the turbulence models require sufficient knowledge about the surface properties (Alves Portela and Sandham, 2020). Large eddy simulation is a more feasible approach than DNS. Recall that LES introduces the effects of small-scale flow structures using an SGS model. Hence, expressing the effects of small-scale roughness comparable to the unfiltered flow dynamics is a challenge (Jimenez, 2004). This chapter presents a method to implement the WMLES approach in resolving high-Reynolds number turbulent flows while the effects of wall roughness are introduced via wall-modeling. The grid resolution used in the wall layer is higher compared to traditional RANS methods, which helps to resolve the roughness elements. First, the history of some roughness models is presented. Then, the methodology of introducing the effects of wall roughness is described and implemented in the simulation of rough wall channel flows. Finally, the results of WMLES turbulent channel flows including wall roughness are presented and discussed.

7.2 Background to Wall Roughness Modeling

Wall roughness models can be categorized into homogeneous and sparse element roughness. Homogeneous roughness replaces the stochastic roughness length scales with an equivalent height, which is known as the effective roughness. There are different methods to determine the equivalent height of roughness, which consider the spacing between roughness elements and their shape (Dirling, 1973). On the other hand, each element is usually resolved in the sparse element category, and the effects are introduced to the control volume. The effects of roughness are introduced via the turbulence model when a RANS approach is employed, whereas the roughness elements affect the momentum equation via an additional drag force when using DNS or LES (Schultz and Flack, 2007; Krumbein et al., 2017). According to the roughness categories, there are two generic methods to model wall roughness: 1) equivalent sand grain roughness, and 2) discrete element approach (Taylor et al., 1985). The following sections will elaborate on these methods.

7.2.1 Equivalent Sand Grain Roughness

In the equivalent sand grain approach, homogeneous roughness is considered with a uniform roughness length scale on the wall. Schlichting (1936) conducted a comprehensive set of experimental tests to correlate the effective roughness height (k_s) with the height and shape

of the roughness and its surface density. He proposed sparse and dense regimes for rough walls. In the sparse regime, in which the roughness elements occupy less than 15 percent of wall-parallel area, the effect of roughness increases with increasing the density of roughness elements. The dense regime indicated an opposite behavior since the roughness elements now shelter each other. Coleman et al. (1984) re-evaluated Schlichting's results, and the case studies with very sparse roughness were included to make a comprehensive reference for other studies.

Several turbulence models have been developed to allow the calculation of wall-bounded turbulent flows over rough walls. Rotta (1962) suggested including the effects of wall roughness by shifting the surface plane upwards by a distance Δy comparable to the equivalent roughness height. A non-zero velocity boundary condition in the direction opposite to the mean flow is introduced to the reference plane (at $y = 0$) to satisfy the no-slip boundary condition at the shifted plane. Despite achieving the desired effect on the law of the wall, the estimated shift is often higher than the height of the roughness element, which shows no direct physical connection to the flow. Cebeci and Chang (1978) were inspired by the shifting hypothesis in solving the boundary layer equation over a rough plate. They proposed that the shifting distance can be included in the mixing length model as follows:

$$\ell_m = 0.4(y + \Delta y)\mathcal{D} \quad , \quad \mathcal{D} = \left[1 - \exp\left(-\frac{y + \Delta y}{A}\right) \right], \quad (7.5)$$

where Δy is expressed as a function of equivalent sand grain roughness by

$$\Delta y = 0.9 \left(\frac{\nu}{u_\tau} \right) \left[\sqrt{k_s^+} - k_s^+ \exp\left(-\frac{k_s^+}{6}\right) \right]. \quad (7.6)$$

Eq. 7.5 is expected to be valid over a wide range of k_s^+ , but it may lose accuracy over a complete spectrum of flow problems with similar geometries since the proposed model was studied only in a limited range of roughness geometries and pressure gradients.

Later, Krogstad (1991) proposed a new modification to the van Driest damping function \mathcal{D} to adjust the eddy viscosity near the wall. He believed that the main role of wall roughness is to increase turbulence near the roughness elements. Hence, turbulent shear stresses are calculated by relating the increase in turbulence to the wall roughness. The modified damping function is given by

$$F = 1 - \exp\left(-\frac{y^+}{A^+}\right) + \exp\left[-\frac{y^+}{A^+} \left(\frac{R^+}{k_s^+}\right)^{3/2}\right] \sqrt{1 + \exp\left(-\frac{R^+}{k_s^+}\right)}, \quad (7.7)$$

where $A^+ = 26$ and $R^+ = 70$. This model is limited to a range of roughness heights, and the results of very small or very large roughness values showed discrepancies between the proposed model and experiments.

Spalart (2000) developed an early and well-known turbulence model, i.e. the so-called one-equation Spalart-Allmaras model, to introduce the effects of surface roughness. The eddy viscosity obtained from the transport equation ($\tilde{\nu}$) is modified as follows:

$$\nu_t = f_{v1} \tilde{\nu} \quad , \quad f_{v1} = \frac{\chi^3}{\chi^3 + C_{v1}^3} \quad , \quad C_{v1} = 7.1, \quad (7.8)$$

where ν_t is the modified eddy viscosity which contains the effects of roughness. He used χ to include the wall roughness as follows:

$$\chi = \frac{\tilde{\nu}}{\nu} + C_{R1} \frac{k_s}{d} \quad , \quad C_{R1} = 0.5. \quad (7.9)$$

He also proposed an extension to the original model in which a non-zero boundary condition was assumed for the eddy viscosity at the wall to imitate the effects of roughness.

$$\frac{\partial \tilde{\nu}}{\partial n} = \frac{\tilde{\nu}}{d}, \quad (7.10)$$

where n is the direction normal to the wall, and d is defined by

$$\begin{aligned} d &= d_{\min} + d_o \\ d_{\min} &: \text{distance to the wall} \\ d_o &= k_s \exp(-8.5 \kappa) \approx 0.03 k_s. \end{aligned}$$

Aupoix and Spalart (2003) compared this modified Spalart-Allmaras model with experimental studies. They found that the results were in fair agreement with experiments when the roughness height is much smaller than the boundary layer thickness. Furthermore, the heat transfer is over-predicted by introducing the effect of roughness in the eddy viscosity model compared to the prediction of the skin friction.

Modeling the effects of roughness is not limited to one-equation turbulence models. Zhang et al. (1996) introduced the height of equivalent roughness to turbulence model functions (f_1 and f_2) in a low-Reynolds number $k - \varepsilon$ model. The model functions in the $k - \varepsilon$ model play a damping role for the eddy viscosity near the wall similar to van Driest's damping function. Hellsten and Laine (1997) modified the $k - \omega$ model by adding a roughness parameter to the turbulence frequency ω and achieved acceptable results for rough boundary layers and airfoils. Dutta et al. (2017) evaluated the performance of three turbulence models over rough

boundary layers with non-zero pressure gradients. The results indicated that most models are sufficiently accurate in mild pressure gradients, although some errors were observed close to the separation and reattachment regions due to the fundamental eddy viscosity assumption. Note that all models proposed in this section are employed in RANS turbulence models, which require solving additional transport equations to estimate the Reynolds stresses.

7.2.2 Discrete Element Method

The discrete element method introduces the effects of roughness elements on a flow as a form drag term to the momentum equation (Taylor et al., 1985). This additional term pertains to the blockage effects of roughness on the near-wall flow structures. The flow resistance of roughness includes the form and viscous drag. The form drag is exerted on roughness elements whereas viscous shear is exerted on the smooth area between the roughness elements. Hence, the wall shear stress can be expressed based on these two components as follows:

$$\tau_w = \mu \frac{\partial u}{\partial y} + \frac{F_D}{A_y} \quad , \quad F_D = \frac{1}{2} C_D \rho u^2 A_P, \quad (7.11)$$

where A_y is the wall-parallel surface area, A_P is the projected area of a single roughness element, and u is the local streamwise velocity. There are different methods to determine the magnitude of C_D (Taylor et al., 1985).

The discrete element method has been employed in different applications. Taylor et al. (1985) used the discrete element method on a Reynolds-averaged two-dimensional TBL. Reynolds stresses are modeled with a simple zero-equation Prandtl mixing length model and C_D is described as a function of the Reynolds number,

$$\begin{cases} \log C_D = -0.125 \log(\text{Re}_d) + 0.375 & , \quad \text{Re}_d < 6 \times 10^4 \\ C_D = 0.6 & , \quad \text{Re}_d \geq 6 \times 10^4. \end{cases} \quad (7.12)$$

Busse and Sandham (2012) proposed a parametric forcing approach in the simulation of a turbulent channel flow using DNS. Instead of resolving a rough surface, the momentum equation contains an additional term to consider the effects of roughness as follows:

$$\frac{\partial u_i}{\partial t} + \frac{\partial u_j u_i}{\partial x_j} = -\frac{\partial p}{\partial x_i} + \nu \frac{\partial^2 u_i}{\partial x_i^2} + f_i, \quad (7.13)$$

where f_i is the forcing term and defined as

$$f_i = -\alpha_i F_i(y, h_i) u_i |u_i|. \quad (7.14)$$

The parameter α_i is the roughness factor which indicates the sparseness of roughness elements, and F_i is the roughness shape function that adjusts the strength of the forcing term at a specific distance from the wall. The parameter h_i is the height of a particular roughness element. The form of $(-u_i |u_i|)$ ensures that the roughness always resists the flow. Eq. 7.14 indicates that the wall roughness is determined through the α_i and $F_i(y, h_i)$ parameters. The results suggest that the value of α_i in the x -direction has the most significant effect whereas α_y and α_z only have a weak drag effect. They assigned a Gaussian profile to the shape function as follows:

$$F_i(y, h_i) = \exp\left(-\frac{y^2}{h_i^2}\right), \quad (7.15)$$

where y is the distance from the wall. Although this model represents reliable results in fully rough and transitional rough regimes, it is strongly dependent on specifying an appropriate shape function and a correct roughness factor for a particular flow problem.

The parametric forcing approach only considers a form drag of roughness whereas some areas between the roughness elements experience relatively slow flows (Forooghi et al., 2018). At these locations, the quadratic term of the form drag in Eq. 7.14 is not the only dominant force, and a linear forcing term can be introduced to account for the viscous drag. Hence, the last term on right-hand side of Eq. 7.13 becomes

$$f_i = f_{L,i} + f_{Q,i} = -A(y)u_i - B(y)u_i |u_i|. \quad (7.16)$$

There is a clear analogy between this model and the classical Darcy-Brinckmann-Forchheimer equation for flows in porous media where linear (Darcy) and quadratic (Forchheimer) terms are used to represent, respectively, viscous and inertial resistance to the flow (Vafai and Kim, 1995). Therefore, $A(y)$ is accounted for in the context of porous media while $B(y)$ represents the form drag of a bluff body as a roughness element. Kuwata and Kawaguchi (2019) re-evaluated the parametric forcing approach of Forooghi et al. (2018) by spatially averaging the drag force in the wall-parallel planes. Their forcing term is very similar to the previous study, but it is implemented in the simulation of turbulent rough walls using a Lattice-Boltzmann approach. The proposed model is only valid in turbulent flows over sparse roughness elements.

Krumbein et al. (2017) assessed the performance of a discrete element method in a hybrid

RANS/LES model. This model was developed based on the concept of VLES of Speziale (1998). The forcing term in their model is defined as follows:

$$f_i = -\frac{1}{2}\tilde{u}_j\tilde{u}_j\frac{\tilde{u}_i}{\sqrt{\tilde{u}_k\tilde{u}_k}}\frac{D(y)}{L}, \quad (7.17)$$

where $\frac{1}{2}\tilde{u}_j\tilde{u}_j$ is the dynamic pressure, L is the maximum height of the roughness, and $D(y)$ is a drag function very similar to the shape function in Eq. 7.15. The drag function D is specified based on a complementary DNS by spatially averaging data sets in the streamwise and spanwise directions and estimating the drag force associated with the RANS equation in the streamwise direction. Later, Krumbein et al. (2019) proposed another rough wall model based on the discrete element method, in which both viscous drag and form drag are considered similar to Eq. 7.16. Using the volume-averaged Navier-Stokes (VANS) method developed by Whitaker (1996), they modeled the effect of roughness as an equivalent porosity. However, both models require the results of DNS in advance to *a priori* determine the coefficient in the forcing term correlation or the drag function.

7.3 Roughness in Wall-modeling

With the advent of wall-modeling methodology, the effects of roughness have been studied in the context of estimating the wall shear stress. In an early work, Mason (1994) proposed a wall function based on the logarithmic law and using the Monin-Obokhov similarity theory boundary conditions to model drag in a flow. The flow information at the first grid point above the roughness is used to estimate the wall shear stress. Anderson and Meneveau (2011) modified this model by introducing a forcing term, which includes the wall shear stress, to the momentum equation. They argued that only the roughness elements larger than the filter scale are resolved. Hence, the unresolved roughness elements were modeled and introduced as a wall shear stress to the first cell near the wall. The wall shear stress is linearly adjusted to the instantaneous local velocity as follows:

$$\tau_w(x, z) = \frac{1}{\rho} \left[\frac{\kappa U(x, z)}{\log\left(\frac{y_m - d}{k_s}\right)} \right]^2 \frac{u_i(y_m)}{U(x, z)}, \quad (7.18)$$

where $U(x, z) = \sqrt{u^2 + w^2}$, y_m is the height of the first node, d is the resolvable height of roughness, and u_i is the local instantaneous velocity. The value of the von Karman constant

should be adjusted for different flow geometries. This model was tested in LES of high-Reynolds number flows over various rough surfaces and results were promising. In addition to the wall stress models, there are other methods in modeling the wall layer where the effects of roughness are included, which will be discussed in the following sections.

7.3.1 Virtual Wall Model

A new wall model (the virtual wall model) to be coupled with LES was proposed by Chung and Pullin (2009). A slip boundary condition is assumed at a raised virtual wall by integrating the effects of flow motions across the wall layer. The streamwise momentum equation at the first control volume near the wall is filtered in a wall-parallel layer where the width of the filter is larger than the viscous length scale. The streamwise momentum equation is shown as follows:

$$\frac{\partial \tilde{u}}{\partial t} + \frac{\partial \tilde{u}\tilde{u}}{\partial x} + \frac{\partial \tilde{u}\tilde{v}}{\partial y} + \frac{\partial \tilde{u}\tilde{w}}{\partial z} = -\frac{\partial \tilde{p}}{\partial x} + \nu \frac{\partial^2 \tilde{u}}{\partial y^2}. \quad (7.19)$$

After averaging over the wall-parallel layer and integrating $\frac{\partial \tilde{u}\tilde{v}}{\partial y}$ and $\nu \frac{\partial^2 \tilde{u}}{\partial y^2}$ in the wall-normal direction, Eq. 7.19 becomes:

$$\frac{\partial \langle \tilde{u} \rangle}{\partial t} + \frac{\partial \langle \tilde{u}\tilde{u} \rangle}{\partial x} + \frac{\partial \langle \tilde{u}\tilde{w} \rangle}{\partial z} = -\frac{1}{h_{\text{wm}}} \tilde{u}\tilde{v} \Big|_{h_{\text{wm}}} - \frac{\partial \tilde{p}}{\partial x} \Big|_{h_{\text{wm}}} + \frac{\nu}{h_{\text{wm}}} \left(\frac{\partial \tilde{u}}{\partial y} \Big|_{h_{\text{wm}}} - \frac{\partial \tilde{u}}{\partial y} \Big|_0 \right), \quad (7.20)$$

where h_{wm} is the height of the wall layer, and $\langle \cdot \rangle$ indicates a spatially averaged parameter in a wall-adjacent layer. Saito et al. (2012) improved this model by modifying the temporal term to include the effects of surface roughness. The unsteady term in Eq. 7.20 is resolved within a general form of inner scaling, and increased momentum deficit due to roughness is accounted for as follows:

$$\tilde{u} = u_\tau \left(F(y^+) - \Delta U^+ \right), \quad (7.21)$$

where ΔU^+ is the roughness function or shifted velocity profile downward, and $F(y^+)$ is a generic term considered for both rough and smooth walls. The roughness function is formulated based on the roughness geometry and universal correlation proposed by Colebrook (1939) as

$$\Delta U^+ = \frac{1}{\kappa} \ln \left(1 + 0.26 k_s^+ \right). \quad (7.22)$$

He studied the performance of this model in transitionally rough and fully rough pipe flows and compared the results with the Moody diagram. Favorable agreement with empirical correlations was observed.

7.3.2 Immersed Boundary Method

Orlandi and Leonardi (2008) resolved the geometry of roughness elements by refining the mesh near the wall together with an efficient immersed boundary method (IBM) using DNS and LES. They conducted several simulations with different kinds of roughness shapes to create a database for the parameterization of the roughness function. They proposed that the modifications of the flow structures in the wall region are best represented by the wall-normal velocity distribution. Hence, they proposed a roughness function based on the wall-normal fluctuations $\tilde{u}_2^+|_w$ as follows:

$$\Delta U^+ = B \frac{\tilde{u}_2^+|_w}{\kappa} \quad (7.23)$$

with $B = 5.5$ and $\kappa = 0.41$. Note $|_w$ indicates the value at an imaginary plane that contains the crests of the roughness elements. This correlation is useful in both numerical and experimental studies to evaluate the friction velocity over rough surfaces. Piomelli and Yuan (2013) proposed an LES approach to resolve the roughness elements using IBM based on the volume-of-fluid method. The desired equivalent roughness in their study was generated by introducing a sufficient number of cubes at random heights that fluctuate around a specific height k_s (Scotti, 2010). The fraction of volume not occupied by the roughness element is used to estimate the velocity at each cell near the wall. They implemented this methodology to visualize hairpin packets in the near-wall region and turbulent structures in the outer layer.

7.3.3 Other Models

Yang et al. (2015) introduced an integral WMLES to study high-Reynolds number TBLs, which includes the effects of wall roughness. The momentum equation in the wall layer using the RANS equations has a form drag term as follows:

$$f_x = -C_D a_{Lx} |U| \langle \tilde{u} \rangle, \quad f_z = -C_D a_{Lz} |U| \langle \tilde{w} \rangle, \quad (7.24)$$

where C_D is the drag coefficient, $|U| = \sqrt{\langle \tilde{u} \rangle^2 + \langle \tilde{w} \rangle^2}$ is the velocity magnitude, and a_{Lx} and a_{Lz} are the roughness area density. $\langle \cdot \rangle$ indicates the parameter is spatially filtered and temporally averaged over an appropriate time period. Furthermore, the effect of roughness is considered in the estimation of the wall shear stress

$$\tau_w = (\nu + \nu_t) \frac{\partial \langle \tilde{u} \rangle}{\partial y} \Big|_{y=0} + \int_0^{h_{wm}} C_D a_{Lx} |U| \langle \tilde{u} \rangle dy. \quad (7.25)$$

This model, which is a form of discrete element method, was evaluated in different flow geometries, and promising results for flows over rough surfaces were observed.

Alves Portela and Sandham (2020) presented an approach that resolves the inner layer using DNS and the outer layer using URANS. They blended the DNS and URANS equations by combining the Reynolds stresses to make a model-free NSE. A blending factor is introduced to the new momentum equation, and it varies gradually when switching from DNS to URANS. Moreover, a parametric forcing approach developed by Busse and Sandham (2012) discussed in Section 7.2.2 is implemented in the DNS domain to resolve wall roughness elements. A mismatch is observed between the DNS and RANS stresses at the interface and requires special considerations. However, the computational cost of the proposed method is reduced significantly.

7.4 Methodology for Introducing Surface Roughness to Dynamic Non-equilibrium Wall Stress Model

There are different methods for including the effects of wall roughness in calculating the flow structures in the near-wall region. The discrete element method represents a reliable approach for resolving the flow dynamics in the wall layer. However, use of the wall-modeling implies that the near wall flow is modeled and introduced to the outer layer as a wall shear stress in a time-averaged framework. Hence, resolving the roughness element, which the discrete element method relies on, is incompatible with the notion of wall modeling, i.e. reducing the computational cost and expediting the simulation process. In this study, a modified mixing length $\ell_m = \kappa y \mathcal{F}$ is employed to model the effects of the roughness elements. The correction proposed by Krogstad (1991) to the van Driest damping function as shown in Eq. 7.7 is implemented in the dynamic eddy viscosity in Eq. 3.25 to modify the eddy viscosity as follows:

$$\nu_{t,\text{wm}} = (\kappa y \mathcal{F})^2 |S| + \frac{\overline{R}_{ij} \overline{S}_{ij}}{2 \overline{S}_{ij} \overline{S}_{ij}}, \quad (7.26)$$

$$\mathcal{F} = 1 - \exp\left(-\frac{y^+}{A^+}\right) + \exp\left[-\frac{y^+}{A^+} \left(\frac{R^+}{k_s^+}\right)^{3/2}\right] \sqrt{1 + \exp\left(-\frac{R^+}{k_s^+}\right)},$$

with $A^+ = 26$ and $R^+ = 70$. The value of R^+ represents the lower limit for fully rough regimes as discussed earlier in Section 7.1.

Using Eq. 7.26 to model the effects of wall roughness requires additional considerations. First, it is essential to locate the matching point sufficiently higher than the equivalent roughness height (Saito et al., 2012; Yang et al., 2015; Alves Portela and Sandham, 2020). There is an analogy between this constraint and the mismatch treatment discussed in Section 4.3, where the efficiency of the SGS model declined when using a coarse mesh near the wall, and the location of the matching point was moved to higher grid points in the LES domain to mitigate this deficiency. The proposed damping function (\mathcal{F}) for two different roughness heights is shown in Fig. 7.1. The original damping function, i.e. $\mathcal{D} = 1 - \exp(-y^+/A^+)$, is also presented for comparison. For both rough cases, the \mathcal{F} profile approaches one (red line) and the effect of the damping function becomes negligible when y^+ is 50% larger than the k_s^+ value. Therefore, in the study of turbulent channel flows with different roughness heights, the matching point is located at least 50% farther than the roughness height.

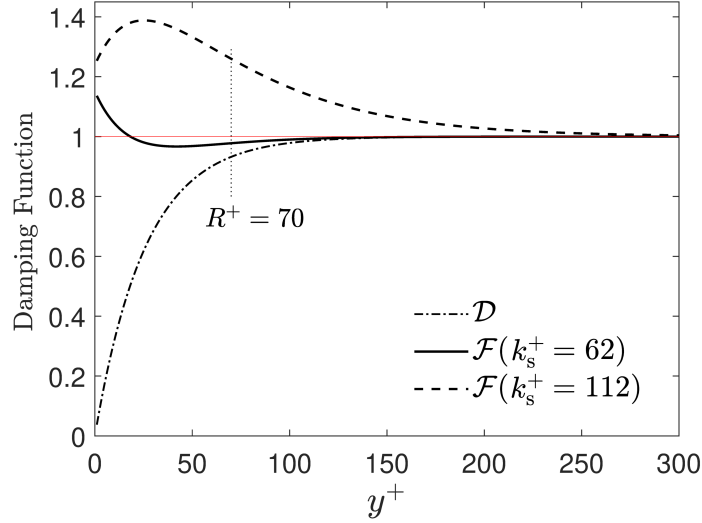


Figure 7.1: Modified damping functions in Eqs. 7.5 and 7.26 for wall roughness with $R^+ = 70$.

The next consideration pertains to the estimation of the wall shear stress. For the smooth case studies, the wall shear stress is directly calculated from the mean velocity gradient at the wall, i.e. $\tau_w = \mu dU/dy$. However, applying the modified mixing length results in lower velocity gradients near the wall below the roughness height. Consequently, a lower wall shear stress is predicted using the slope of the mean velocity profile whereas a higher value is expected for flow over the rough wall.

The time-averaged x -momentum equation is a more convenient way to estimate the wall

shear stress (Burattini et al., 2008),

$$\frac{1}{\rho} \frac{dP}{dx} = \nu \frac{d^2 U}{dy^2} - \frac{d}{dy} \overline{u'v'}, \quad (7.27)$$

which can be rewritten as

$$\frac{dP}{dx} = \frac{d\tau}{dy}, \quad \tau = \mu \frac{dU}{dy} - \rho \overline{u'v'}, \quad (7.28)$$

where τ is the total shear stress. This method relates the wall shear stress to the pressure gradient, and it has been successfully implemented in several experimental and numerical studies of turbulent channel flows (Krogstad et al., 2005; Busse and Sandham, 2012; Forooghi et al., 2018; Krumbein et al., 2019). However, the main drawback is that it does not apply to flows with zero pressure gradient.

In this study, the wall shear stress is predicted by extrapolation from two points inside the wall layer as shown in Fig. 7.2. The total shear stress is calculated using Eq. 7.28 and the mean velocity profile. The eddy viscosity is obtained from Eq. 7.26, and Boussinesq's hypothesis is implemented to estimate the Reynolds shear stress as follows:

$$-\rho \overline{u'v'} = \nu_{t,wm} \frac{dU}{dy}. \quad (7.29)$$

By a linear extrapolation, the wall shear stress is obtained as

$$\frac{\tau_2 - \tau_w}{\tau_2 - \tau_1} = \frac{y_2 - 0}{y_2 - y_1}. \quad (7.30)$$

Hypothetically, points “1” and “2” should be located below the matching point and above the roughness height to achieve a reliable result. This correlation can be simplified for channel flows with similar rough surfaces on both walls. In such channel flows, the total shear stress becomes zero at the center of the channel ($\tau_2 = 0$), and one can locate point 2 at the center of the channel ($y_2 = \delta$). Hence, Eq. 7.30 can be expressed as

$$\tau_w = \frac{\tau_1}{1 - y_1/\delta}. \quad (7.31)$$

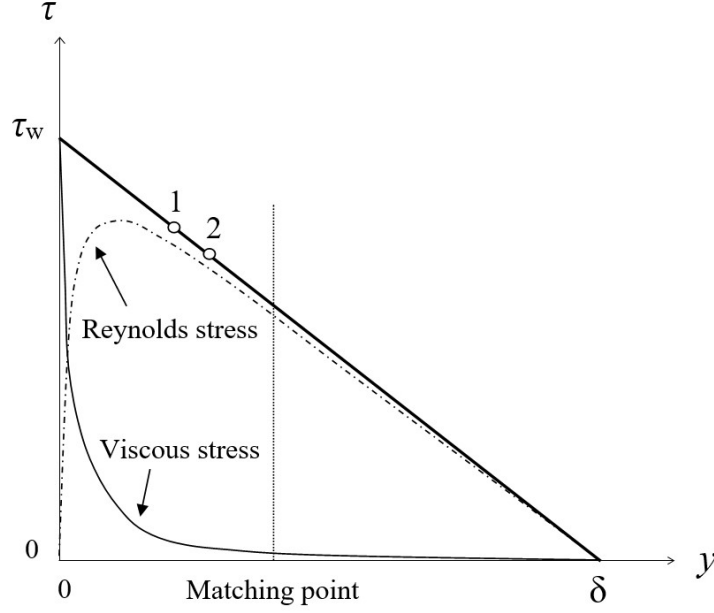


Figure 7.2: Schematic of total shear stress in wall-bounded turbulent flows used to estimate the wall shear stress by a linear extrapolation.

7.5 Numerical Method

Two flow geometries are implemented to evaluate the proposed wall model. First, a turbulent channel flow with rough surfaces on both walls, i.e. top and bottom walls, is studied. Then, the effective roughness is applied only to the bottom wall, and the top wall is assumed to be smooth. These test cases are employed due to the available experimental data sets to validate the performance of the wall model. The computational domain to resolve the rough channel flow for all test cases is $2\pi\delta \times 2\delta \times \frac{4}{3}\pi\delta$ in the streamwise, wall-normal, and spanwise directions, respectively. A uniform grid distribution is applied in all directions with the grid resolution presented in Table 7.1 for each channel flow. The fifth node in the LES domain is used for the location of the matching point. Initial velocity conditions to begin the simulation are analogous to what was described in Section 4.1. The grid resolution for the wall layer is the same in the wall-parallel planes, and it has a non-uniform grid distribution in the wall-normal direction with 30 grid points. The Courant number is $CFL = 0.3$ and 15 in the LES domain and wall layer, respectively, and no-slip boundary conditions are applied at the walls while periodic boundary conditions are used in the streamwise and spanwise directions. The time averaging and temporal filtering schemes use $T_W = 0.1$ and $T_F = 1.0$ to provide a responsive wall layer. In the symmetric rough channels, A2 and B2, two rough walls are considered, whereas for the asymmetric cases C1 and D1, a rough wall at the bottom and a smooth wall at the top are implemented.

Table 7.1: Specifications of wall-modeled turbulent channel flows with rough walls at different Reynolds numbers.

Case	Re_{τ_r}	$n_x \times n_y \times n_z$	$\Delta x^+, \Delta y^+, \Delta z^+$	k_s^+	h_{wm}^+
A2	615	$48 \times 32 \times 48$	78, 38, 52	62	163
B2	2080	$80 \times 64 \times 64$	157, 62, 130	62	272
C1	640	$48 \times 32 \times 48$	70, 33, 46	62	146
D1	1160	$64 \times 48 \times 48$	94, 40, 83	112	174

7.6 Wall-modeled Turbulent Flow in a Symmetric Rough Channel

The test cases with roughness on the top and bottom walls are evaluated in this section (A2 and B2). The symmetric channel flows are pressure-driven, so that a constant pressure gradient is introduced in the source term of the momentum equation. For test case A2, the dimensionless equivalent roughness height is $k_s^+ = 62$, and the Reynolds number based on the friction velocity of the rough surface is $\text{Re}_{\tau_r} = 615$. The mean flow field is obtained by recording the flow statistics over $T^+ = 19900$ with an average time step of $\delta t^+ = 0.972$ (the definition of the dimensionless simulation run-time T^+ and mean time step δt^+ were discussed earlier in Section 4.1). An additional simulation with the same computational domain is also run in a smooth channel to study the mean velocity shift ΔU^+ .

Fig. 7.3 shows the mean velocity profile of the test case A2 in wall coordinates and outer coordinates. The experimental results of Krogstad et al. (2005) are also presented, in which smooth and rough channel flows were conducted at a similar Reynolds number and roughness height. They initially performed measurements using a hot wire anemometer over a smooth channel flow, then non-staggered square rods were placed on both walls to achieve the desired roughness height. A visual comparison between the wall-modeled rough channel flow and experimental study of Krogstad et al. (2005) in Fig. 7.3a indicates a good prediction of the mean velocity profile in the outer region for the rough case, while the mean velocity in the near-wall region is over-predicted. This deviation is inherent in the wall-modeling, and it was discussed earlier in the simulation of wall-modeled channel flows in Chapter 4. The downward mean velocity shift in the logarithmic region is $\Delta U^+ = 7.8$, which is shown with a dashed line. Nikuradse (1950) suggested a value of $\Delta U^+ = 8.5$ for a fully rough pipe flow whereas Schlichting (1936) used $\Delta U^+ = 8.0$ for a fully rough boundary layer. The experimental study of Krogstad et al. (2005) also provides $\Delta U^+ = 8.7$ for the rough channel flow. Using Colebrook’s correlation as shown in Eq. 7.22 gives $\Delta U^+ = 7.4$ for the corresponding roughness

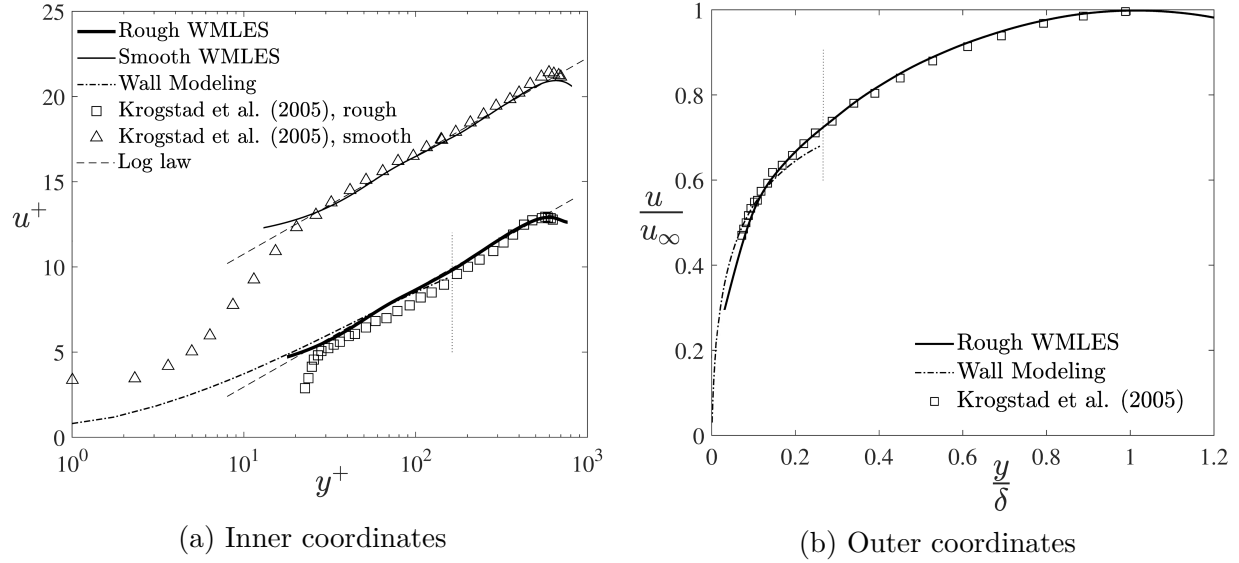


Figure 7.3: Mean velocity profile of the wall-modeled channel flow with roughness on both walls at $Re_{\tau_r} = 615$ with $k_s^+ = 62$; smooth WMLES at $Re_{\tau_r} = 655$, dashed line; Krogstad et al. (2005) at $Re_{\tau_r} = 600$ with $k_s^+ = 63$, \square ; Krogstad et al. (2005) at $Re_{\tau_s} = 670$, \triangle ; log law for the smooth test case, $\kappa = 0.4$ and $B = 5.0$; the location of the matching point is shown with a dotted line.

height. Fig. 7.3b shows the mean velocity profile in outer coordinates, and no significant discrepancy is observed between the WMLES profile and experiments.

The *rms* of the velocity fluctuations and Reynolds shear stress profiles across the channel are shown in Fig. 7.4 and compared to the experimental data of Krogstad et al. (2005). The velocity fluctuations are well predicted, although a slight deviation is observed at the center of the channel. The accuracy of the predictions decreases in the near-wall region due to the inconsistency between the SGS requirements and grid resolution. The Reynolds shear stress ($\overline{u'v'^+}$) matches the experimental profile in most regions, with a deviation observed in the wall region. The profiles of v'^+_{rms} and $\overline{u'v'^+}$ indicate a gradual decrease in magnitude when moving towards the wall. This feature relates to the wall-normal velocity, which experiences the no-penetration boundary condition at the wall directly.

The next set of results in this section were obtained from a turbulent channel flow at a higher Reynolds number of $Re_{\tau_r} = 2080$ with $k_s^+ = 62$. The mean velocity profiles of case B2 are presented in Fig. 7.5. The results are compared with the velocity distribution of the standard $k - \varepsilon$ turbulence model modified by Suga et al. (2006) using an analytical wall function. A small difference is observed between the WMLES profile and $k - \varepsilon$ model. The mean velocity profile is shifted upward which can be due to under-estimating the friction velocity over a rough surface. For the smooth case, the mean velocity profile is in good

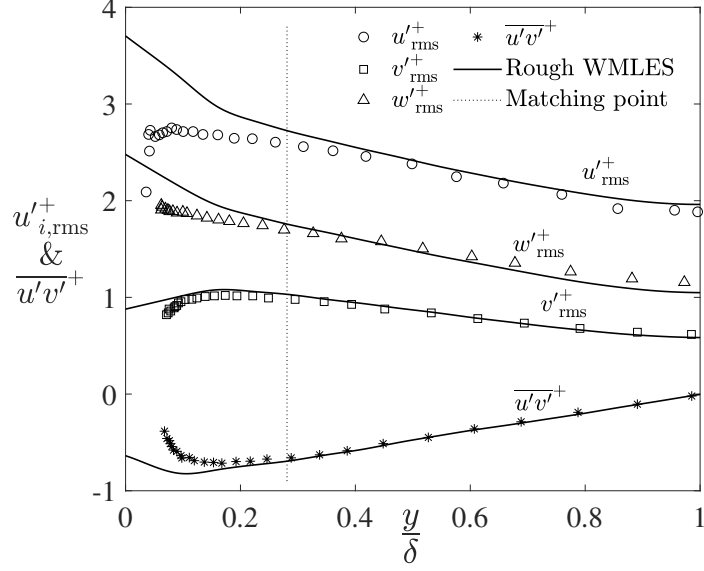


Figure 7.4: Velocity fluctuations and Reynolds shear stress in a channel flow at $Re_{\tau_r} = 615$ with $k_s^+ = 62$. Symbols: experiments by Krogstad et al. (2005), solid lines: WMLES. The profiles of w'_{rms}^+ and u'_{rms}^+ are shifted up by 0.5 and 1.0 for clarity, respectively.

agreement with the DNS results of Hoyas and Jiménez (2006) at $Re_{\tau} = 2000$. The mean velocity is shifted downward by $\Delta U^+ = 6.6$ which is somewhat lower (11%) than the value obtained from Colebrook's correlation, i.e. $\Delta U^+ = 7.4$. A part of this discrepancy relates to

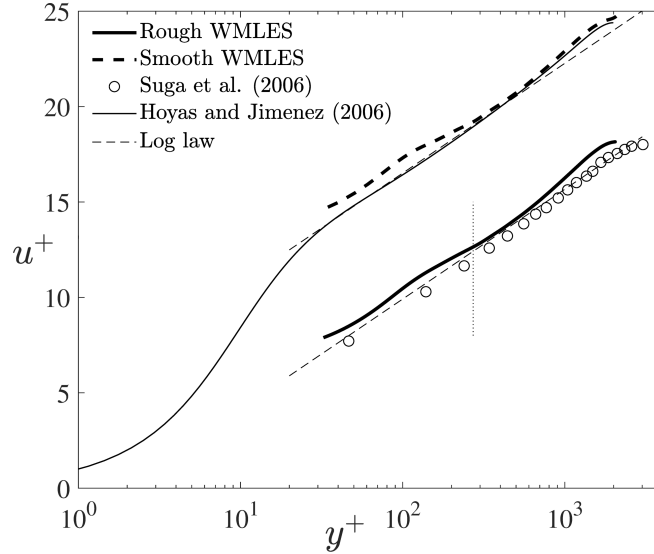


Figure 7.5: Mean velocity profile of the rough channel flow at $Re_{\tau_r} = 2080$ with $k_s^+ = 62$; smooth WMLES at $Re_{\tau_s} = 1970$, dashed line; Suga et al. (2006) at $Re_{\tau_r} = 2580$ with $k_s^+ = 63$, \circ ; Hoyas and Jiménez (2006) at $Re_{\tau_s} = 2000$ with smooth walls, thin solid line; matching point, dotted line.

the under-estimation of the friction velocity u_{τ_r} for the rough wall.

7.7 Wall-modeled Turbulent Flow in Asymmetric Rough Channel

Cases C1 and D1 represent asymmetric channel flows with roughness on the bottom and a smooth wall at the top of the computational domain. The wall-modeling is applied to both boundaries to estimate the wall shear stress. Fig. 7.6 shows the mean velocity distribution for both cases in wall coordinates. The experimental results of Burattini et al. (2008) are also shown with symbols. Measurements were performed over a channel flow with roughness on one wall, where the height of transverse square rods is 10% of the channel half-height, using a hot wire anemometer. Case C1 predicts the mean flow field of the asymmetric channel flow at $Re_{\tau_r} = 640$ with $k_s^+ = 62$ whereas case D1 is the asymmetric channel flow at $Re_{\tau_r} = 1160$ with $k_s^+ = 112$. For each test case, an additional simulation with smooth walls is calculated using the same flow domain and pressure gradient (as a pressure-driven flow problem) to obtain the mean velocity shift in the logarithmic region. A slight over-prediction of the mean velocity profiles is observed over the rough wall. The mean velocity shift is found to be $\Delta U^+ = 8.4$ for case C1 and $\Delta U^+ = 9.8$ for case D1, which is shown with a dashed line for each case. The corresponding values obtained from Colebrook's correlation (Eq. 7.22) are 7.4 and 8.8, respectively. Although the rough WMLES profile closely follows the experimental profile in Fig. 7.6a, a higher value is found for the shifted mean velocity ΔU^+ compared to case A2. It can be concluded that not only does the effective roughness height affect the mean velocity shift, but also the presence of roughness over one wall or both walls. The ratio of the friction velocity for the rough wall to that for the smooth wall is shown in Table 7.2. Burattini et al. (2008) obtained $u_{\tau_r}/u_{\tau_s} = 1.44$ for an experimental rough channel flow at $Re_{\tau_r} = 640$ and 1.48 for a rough channel flow at $Re_{\tau_r} = 1160$. There is no significant difference between the ratios obtained from experiments and corresponding values for cases C1 and D1.

The mean velocity profiles of cases C1 and D1 in outer coordinates are shown in Fig. 7.7 while the profiles are displaced towards the smooth wall by the rough wall. Note that the mean velocity distribution is over-predicted in the outer layer, although the profiles are in good agreement with the experimental results of Burattini et al. (2008). The location of the maximum streamwise mean velocity across the channel is $y_u/\delta = 1.24$ and 1.28 for cases C1 and D1, respectively. These values are 6.0% in the case C1 and 3.8% in the case D1 off the experimental values reported within the experimental study of Burattini et al. (2008).

Table 7.2: Summary results for symmetric and asymmetric rough channel flows using the wall-modeling.

Case	$\text{Re}_{\tau_r} = \delta u_{\tau_r} / \nu$	$\text{Re}_{\tau_s} = \delta u_{\tau_s} / \nu$	k_s^+	ΔU^+	u_{τ_r} / u_{τ_s}	y_u / δ	T^+	δt^+
A2	615	655	62	7.8	-	1.0	19 900	0.97
B2	2080	1970	62	6.6	-	1.0	42 200	2.14
C1	640	420	62	8.4	1.47	1.24	36 200	1.81
D1	1160	760	112	9.8	1.53	1.28	47 000	2.35

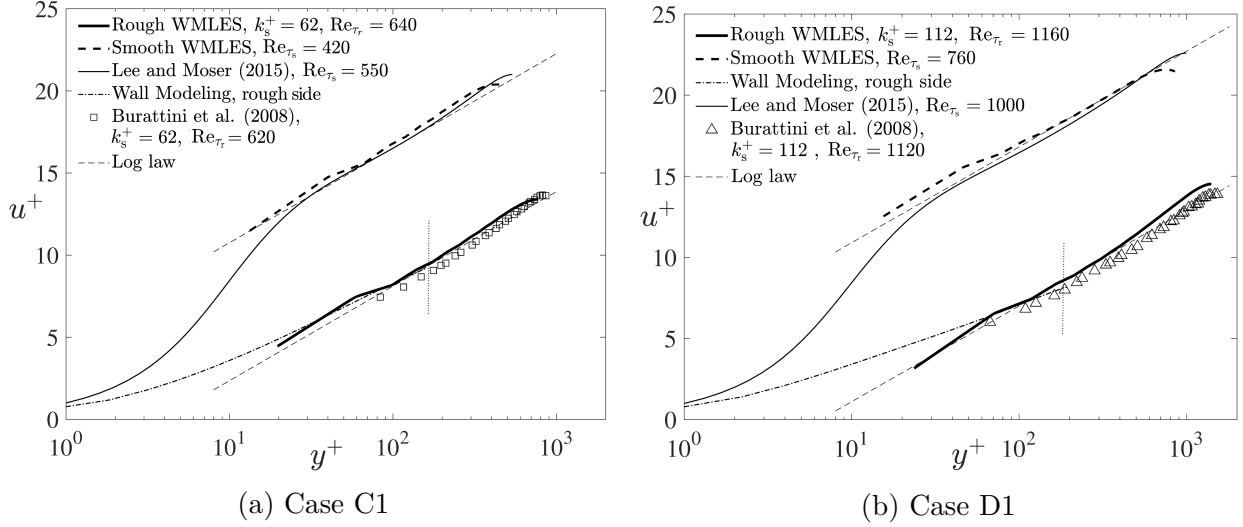


Figure 7.6: Mean velocity profile of asymmetric channel flows for (a) case C1 at $\text{Re}_{\tau_r} = 640$ with $k_s^+ = 62$, and (b) case D1 at $\text{Re}_{\tau_r} = 1160$ with $k_s^+ = 112$; the location of the matching point is shown with a dotted line.

Recall that the grid resolution implemented in the wall-modeled simulations is much lower than used the DNS references to fully resolve the flow structures (Lee and Moser, 2015). The profile for case D1 at $\text{Re}_{\tau_r} = 1160$ indicates a better prediction in contrast to case C1 at $\text{Re}_{\tau_r} = 640$. This reconfirms that the performance of the wall-modeling improves at higher Reynolds numbers.

The velocity fluctuations and shear stress for cases C1 and D1 are given in Fig. 7.8. The profiles of w_{rms}^+ and u_{rms}^+ are shifted one-half unit and one unit upward for clarity, respectively. The symbols are experimental values of the corresponding channel flow collected by Burattini et al. (2008). In general, all profiles indicate good agreement between the wall-modeled numerical studies and experiments. The maximum velocity fluctuations and Reynolds shear stresses are observed near the rough wall, while the minimum values occur near y_u , but do not coincide with it. The streamwise velocity fluctuation, u_{rms}^+ , shows an

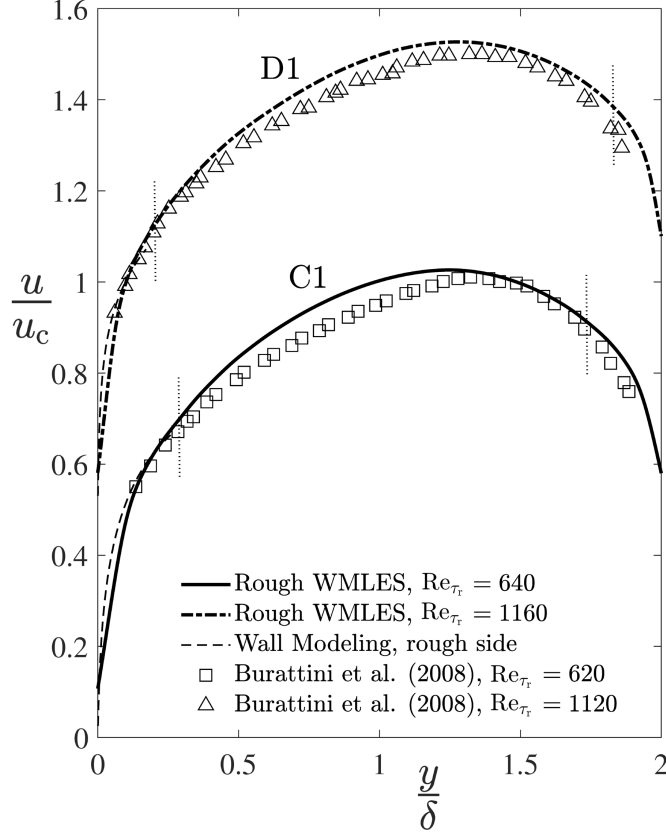


Figure 7.7: Distribution of mean velocity profile in asymmetric rough channel at $Re_{\tau_r} = 640$ with $k_s^+ = 62$ for case C1 and $Re_{\tau_r} = 1160$ with $k_s^+ = 112$ for case D1. The profiles for case D1 are shifted a half unit upwards. The location of the matching point is shown with a dotted line.

under-prediction in the range $0.3 < y/\delta < 1.3$ for both cases, which coincides with the over-predicted mean velocities in the same region as shown in Fig. 7.7. This implies that the grid spacing is too coarse to capture the short wavelength's fluctuations. However, this issue is less at the higher Reynolds number due to the nature of wall-modeling as discussed earlier in Section 2.1.

To further investigate the performance of the proposed wall-model, the turbulent production and turbulence kinetic energy are considered in the following section. The turbulent production is defined as follows (Pope, 2000):

$$\mathcal{P} = -\overline{u'v'} \frac{\partial U}{\partial y}. \quad (7.32)$$

The rate of turbulence production across the channel is shown in Figs. 7.9a and 7.9b. The production for both cases is in good agreement with the experimental values. The maximum

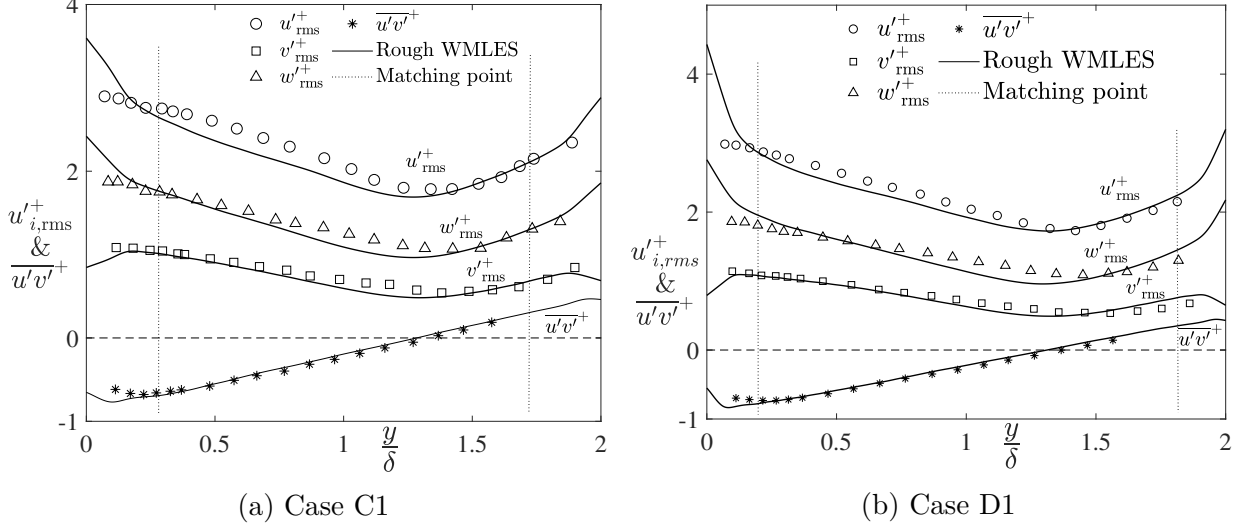


Figure 7.8: Velocity fluctuations and Reynolds shear stress in channel flows for (a) case C1 at $Re_{\tau_r} = 640$ with $k_s^+ = 62$ and (b) case D1 at $Re_{\tau_r} = 1160$ with $k_s^+ = 112$. Symbols: experiments by Burattini et al. (2008), solid lines: WMLES. The profiles of w'_{rms} and u'_{rms} are shifted upward by 0.5 and 1.0, respectively.

rates occur near the rough wall where a slight under-prediction is also observed, which again improved for the higher Reynolds number test case (D1).

The turbulence kinetic energy profiles for cases C1 and D1 are shown in Fig. 7.10. The profiles are normalized by the square of the friction velocity over the rough wall, $k/u_{\tau_r}^2$. Both profiles demonstrate a maximum value near the rough wall while they are displaced towards

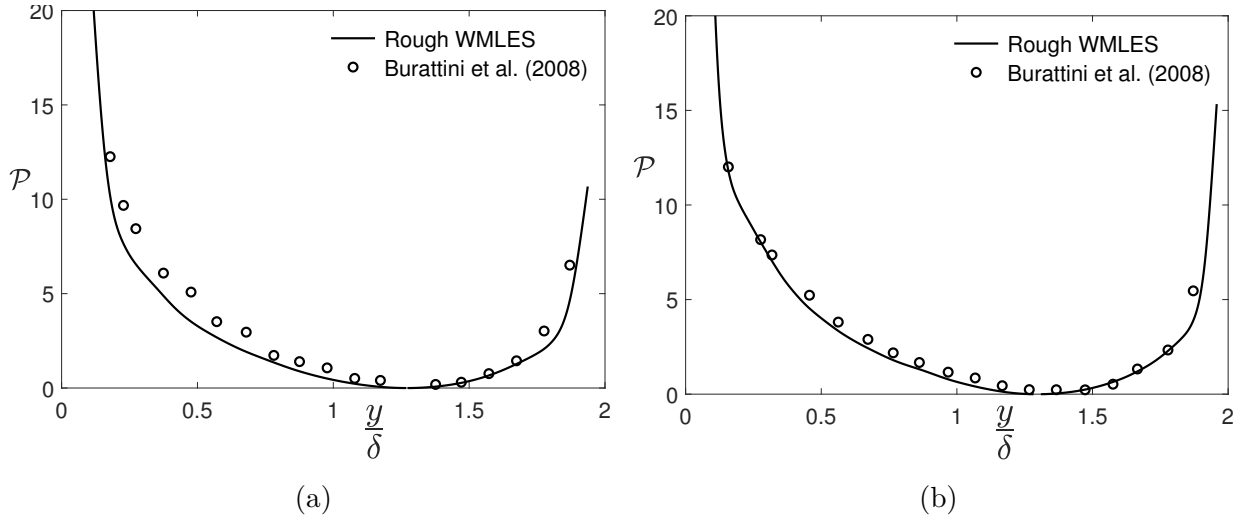


Figure 7.9: The rate of production \mathcal{P} normalized by $\delta/u_{\tau_r}^3$ for (a) case C1 at $Re_{\tau_r} = 640$ with $k_s^+ = 62$, and (b) case D1 at $Re_{\tau_r} = 1160$ with $k_s^+ = 112$.

the smooth wall. The k profiles match each other over most of the channel, although the maximum turbulence kinetic energy has different values for test cases C1 and D1 depending on the Reynolds number. The minimum of k is located close to y_u . This implies that there are some flow structures at y_u which contain a portion of the total energy in the flow although no local production occurs as was shown in Fig. 7.9.

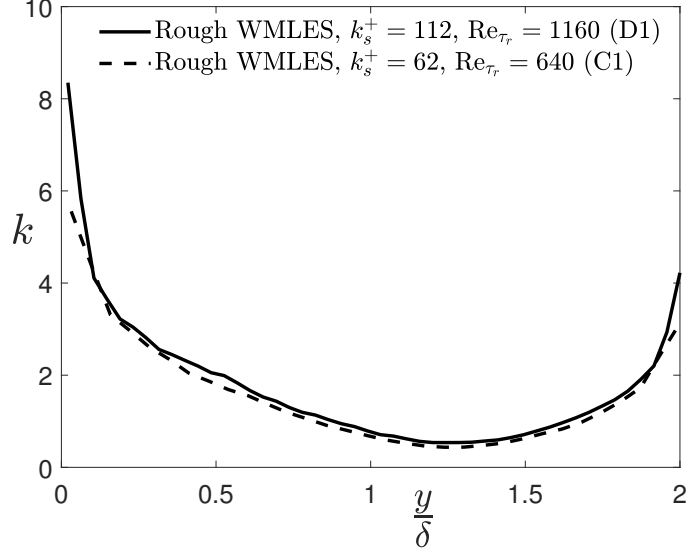


Figure 7.10: Turbulence kinetic energy in asymmetric rough channel flows for test cases C1 and D1.

7.8 Conclusions

The dynamic wall stress model was modified to introduce the effects of wall roughness on the prediction of the wall shear stress. A modified mixing length was implemented for the eddy viscosity parameter in wall-modeling. Four test cases were investigated to validate the performance of the proposed wall model in high-Reynolds number turbulent channel flows. For the first two test cases, a symmetric rough channel was employed to study the flow at $Re_{\tau} = 615$ and 2080. For two other cases an asymmetric channel flow with roughness on the bottom boundary and a smooth wall on the top boundary was simulated at $Re_{\tau} = 640$ and 1160. The solution of the mean flow field was used to study the mean velocity profile using the inner and outer coordinates, the *rms* of velocity fluctuations, and the turbulence kinetic energy. It was shown that the mean velocity profiles are in good agreement with experiments, and the mean velocity shift for different Reynolds numbers and roughness heights was well predicted. The location of the matching point for the wall layer should be selected according

to the roughness height and the performance of the SGS model. For the asymmetric test cases, the maximum velocity and minimum velocity fluctuations were displaced by approximately 25% of the half channel height towards the smooth walls. The turbulence production matched the experimental results, and self-similarity was observed in the prediction of turbulence kinetic energy profiles. A slight under-prediction was observed in the velocity fluctuations and over-prediction in the mean velocity profiles. In general, the proposed dynamic wall model shows promise for the simulation of high-Reynolds number channel flows with transitionally to fully rough regimes using low grid resolution.

Chapter 8

Conclusions, Contributions, and Recommendations

8.1 Conclusions

The challenges associated with the prediction of wall-bounded turbulent flows were addressed in this study. The length scale of the flow dynamics in the near-wall region becomes comparable to the viscous length scale, which requires a much higher grid resolution. Wall-modeling is a technique to circumvent the associated computational cost by introducing the time-averaged effects of the flow dynamics in the wall layer to the outer region as a boundary condition. Wall-modeling was implemented in this research to study high-Reynolds number wall-bounded flows with a significantly lower computational cost. A coarse mesh was implemented to resolve the near-wall region in the LES domain, which reduced the computational cost. To quantify this issue, the computational memory size required for a wall-modeled channel flow was one order of magnitude lower than the memory size for a wall-resolved channel flow at a moderate Reynolds number. For the specific flow considered, the reduction of CPU-hours of computation was even greater due to the performance of CPU cores in performing large computational tasks. However, the significance of wall-modeling was in high Reynolds numbers, and the advantages were problem and hardware specific. The coarse mesh was inconsistent with the requirements of an SGS model. This resulted in an unreliable prediction of the flow characteristics below the matching point by the LES. Fully developed channel flows were tested using the WMLES over a wide range of Reynolds numbers. The results showed that the performance of wall-modeling improved at higher Reynolds numbers.

The next step of this research considered the simulation of ZPGTBLs. Beginning the simulation of TBLs from the leading edge presents another challenge. When the focus is on the prediction of the flow characteristics in the turbulence regime, resolving the flow field from the leading edge is unnecessary. This issue was addressed by adopting a recycling rescaling inflow generation method to introduce realistic turbulence at the inlet of the flow domain. In the outer region, self-similarity was observed in the mean velocity profile of TBLs at moderate to high Reynolds numbers. The numerical results were compared with experimental studies. The mean velocity profiles collapsed well across the boundary layer using a modified scaling law. Furthermore, a promising prediction was observed for the skin-friction coefficient using wall-modeling. Over a wide range of Reynolds numbers, the wall-modeling represented a reliable method to estimate the skin-friction coefficient, based on comparisons to experiments and empirical correlations. Comparing different flow characteristics, such as the mean velocity profile and velocity fluctuations, indicated that the grid resolution inside the boundary layer and above the matching point should be consistent with the length scale of the energy-containing flow structures.

The flow structures above a rough wall are affected by the shape and height of the roughness elements. The effects of roughness become more significant at higher Reynolds numbers since the viscous length scale decreases with increasing Reynolds number. However, resolving the roughness elements in a high-Reynolds number flow is accompanied at a high computational cost. This research included the effects of roughness in wall-modeling. The eddy viscosity was modified for roughness by adding a correction to the damping function. The rough wall model was studied for symmetric and asymmetric rough channel flows over a range of Reynolds numbers. The results were compared with experimental measurements of the mean velocity profile and velocity fluctuations. Good agreement was obtained between the WMLES and experiments, and the roughness shift in the mean velocity was verified with experimental data.

8.2 Major Contributions

The first objective of this research focused on the performance of wall-modeling in predicting the flow characteristics in the wall layer. The time averaging and temporal filtering schemes implemented in the wall-modeling made the wall layer more responsive to the flow structures in the outer layer. It appeared that use of a time period smaller than the convective time scale for averaging the wall layer resulted in a more responsive wall layer, which reduced

the mismatch of the mean velocity profile. Filtering the input from the LES domain to the wall layer improved the results by removing fluctuations at high frequencies, which could lead to an under-prediction or over-prediction of skin friction. A time scale comparable to the turbulent diffusion time scale for filtering the input from the LES domain improved the prediction of wall shear stress. The present study showed that the role of temporal filtering is more crucial when the matching point is located at the first node near the wall. However, using a higher location for the matching point mitigated the log-layer mismatch. The wall-modeling also indicated the potential for the prediction of the mean velocity profile in the wall layer instead of using the result obtained from the LES.

The simulation of TBLs presented the challenge of defining proper boundary conditions to stabilize the numerical solution and avoid unphysical instabilities. Using a rescaling method to generate realistic turbulence at the inlet boundary created a strategy to reduce the size of a computational domain. This promised faster simulations in the study of high-Reynolds number boundary layers with a lower computational cost. Analysis of the grid resolution revealed that additional layers of grid points are required near the outflow boundary to prevent unphysical oscillations for a wall-modeled TBL. In the inner region, replacing a well-refined mesh with a coarse one occurred at the cost of losing accurate predictions of the mean flow field, which is essential for the recycling rescaling inflow generation method. In contrast, the results of wall-modeling showed potential for a better prediction of the mean velocity profile inside the wall layer. It was also shown that the logarithmic law might need a lower value for the von Karman coefficient at higher Reynolds numbers.

Wall roughness is a common characteristic of wall-bounded turbulent flows. Since the focus of this research was on the prediction of high-Reynolds number flows using a wall stress model, the effects of roughness were included in the context of wall-modeling. The main outcome of a wall stress model is the wall shear stress. However, the wall shear stress cannot be calculated using the mean velocity gradient at the wall. Instead, a linear extrapolation of the total shear stress in the wall layer and above the roughness height was used to estimate the wall shear stress at the wall. The results showed that the proposed dynamic non-equilibrium wall model is able to capture the flow dynamics in a rough channel flow at high Reynolds numbers.

8.3 Future Work

The proposed wall-model, which includes the effects of surface roughness, was tested on turbulent channel flows at high Reynolds numbers. Although promising results were obtained, limited Reynolds numbers and roughness heights were studied. It would be of interest to apply the proposed wall model to a rough TBL (Schultz and Flack, 2007; Squire et al., 2016). Note that the simulation of TBLs is accompanied by challenges at the inlet boundary. The conventional rescaling methods are dependent on estimating the friction velocities on smooth flat plate boundary layers. Hence, the rescaling inflow generation requires some modifications as studied by Cardillo et al. (2013) and Yang and Meneveau (2016). Then, the wall model can be implemented in the simulation of high-Reynolds number boundary layers for a wide range of roughness heights. The roughness elements are replaced with an equivalent sand-grain roughness or k -roughness in the proposed wall model. However, a distribution of multiscale roughness heights is observed in many flows such as the formation of turbulent boundary layers over fractal-like rough surfaces in geophysics (Anderson and Meneveau, 2011). The proposed wall model has the potential to be developed into an innovative model that resolves dynamic wall roughness.

Boundary treatment is the main challenge in the simulation of TBLs. The boundary conditions at the top of a computational domain were briefly discussed in this research. Defining proper boundary conditions at the top depends on the flow conditions. For compressible flows, a non-reflective sponge layer has been developed to absorb turbulent fluctuations and any reflections from the top boundary (Mani, 2012). Non-physical oscillations at the top boundary also have the potential to contaminate the entire computational domain in an incompressible flow. The height of the flow domain can increase to avoid the penetration of unphysical oscillations at the top into the freestream region, which on the other hand, results in a higher computational cost. This issue indicates the need for more exploration of top boundary conditions to balance the risk of a contaminated flow domain against the corresponding high computational costs. This study focused on the computationally efficient simulation of ZPGTBLs; however, non-zero pressure gradient TBLs are of interest to a wide range of researchers. TBLs with adverse and favourable pressure gradients are accompanied by a variable freestream velocity, thus they require a different top boundary treatment (Na, 1996; Lee et al., 2010). In the simulation of non-zero pressure gradient TBLs, the challenges in boundary conditions are not restricted to the top boundary. The recycling rescaling method should be adapted to a non-zero pressure gradient condition (Araya et al., 2011). Hence, it is required to develop a strategy to integrate the recycling rescaling method with

the wall layer modeling in the simulation of more complex high-Reynolds number TBLs.

The WMLES employs a coarse grid and is unable to resolve unfiltered small-scale flow structures in the wall region. However, hairpin vortices are important flow structures in wall-bounded turbulence, and they have been investigated in several recent studies (Perret and Kerhervé, 2019). The transition of energy-containing vortical flow structures in the wall layer to the logarithmic law region and above can be investigated in terms of the grid resolution used in WMLES. The turbulent energy is produced in small-scale motions near the wall and transported towards large-scale motions at the edge of the boundary layer. This creates a strong relationship between the velocity fluctuations close to the wall and turbulent/non-turbulent interface (TNTI) large-scale motions. Investigation of the interface morphology and velocity fluctuations near the interface including their correlation with large-scale motions can advance our knowledge of TBLs. An amplitude modulation analysis revealed that the large-scale motions in the outer layer affect the near-wall small-scale flow dynamics (Mathis et al., 2009). The amplitude modulation was also employed in an experimental study to estimate the instantaneous wall shear stress (Mathis et al., 2013). The amplitude modulation indicates the potential for developing an innovative wall model that predicts the wall shear stress without resolving or modeling the flow dynamics in the wall layer. Aligned with the amplitude modulation, the POD analysis is a powerful tool to extract the signature of energetic large-scale motions in the outer layer and at the TNTI.

Wall-modeling has been used in the simulation of turbulent boundary layers and channel flows. However, there is a strong desire to circumvent resolving the wall layer and focus on large-scale eddies far from the wall in more complex geometries, such as the wake region of a bluff body or the recirculation region of a backward facing step flow. Another wall-bounded flow that has the potential to employ wall-modeling is the plane turbulent wall jet. The driving potential is the jet exit momentum, and the inner layer resembles a boundary layer that interacts with a free shear flow in the outer region. The jet spread in the inner layer contributes momentum to the wall layer in addition to the inputs for the top boundary of the wall layer. The proposed dynamic non-equilibrium wall-model, which considers the convection and pressure gradient, would need to incorporate the jet momentum in resolving the wall layer.

Appendix A

Subgrid Scale Models

A.1 Smagorinsky Model

The SGS stress tensor, also known as the *residual stress* tensor, can be decomposed into *anisotropic* and *isotropic* components as follows:

$$\tau_{ij}^* = \tau_{ij}^r + \frac{2}{3} \delta_{ij} k, \quad (\text{A.1})$$

where τ_{ij}^r is the anisotropic residual stress, and k is the kinetic energy of the residual motions. Smagorinsky (1963) described the anisotropic residual stress by an analogy to the eddy viscosity model and the mixing length hypothesis as follows:

$$\tau_{ij}^r = -2 \nu_r \tilde{S}_{ij}, \quad (\text{A.2})$$

where

$$\begin{aligned} \nu_r &= \ell_s^2 |\tilde{S}| \\ &= (C_s \Delta)^2 |\tilde{S}|, \end{aligned} \quad (\text{A.3})$$

where ℓ_s is the Smagorinsky length scale, C_s is the Smagorinsky coefficient, and Δ is the filter width. $|\tilde{S}|$ is the characteristic rate of strain, and it is estimated by

$$\begin{aligned} |\tilde{S}| &= \sqrt{2 \tilde{S}_{ij} \tilde{S}_{ij}}, \\ \tilde{S}_{ij} &= \frac{1}{2} (\tilde{u}_{i,j} + \tilde{u}_{j,i}). \end{aligned} \quad (\text{A.4})$$

The only unknown parameter in the estimation of the residual stresses is the Smagorinsky coefficient (C_S). Note that the LES approach is specifically developed for large-scale turbulent structures. Applying the filter width to the inertial subrange, $C_S = 0.17$ is implemented in the simulation of homogeneous isotropic turbulence (Pope, 2000). However, there are limitations in the application of this value. For turbulent flows with the filter width in the dissipative range, the estimated value for the Smagorinsky coefficient decreases to $C_S = 0.13$. In opposite, when the filter width is very large, the Smagorinsky length ℓ_s tends towards the mixing length. In laminar flows, the appropriate value for the Smagorinsky coefficient is $C_S = 0$ since the residual stresses are zero. Hence, it is difficult to specify a generic empirical value for the Smagorinsky coefficient applicable to all flow geometries.

A.2 Dynamic Smagorinsky Model

The Smagorinsky model was unable to adjust C_S at different flow regimes, which led to the development of a dynamic model. The dynamic model locally adapts C_S based on the physics of the flow. Germano et al. (1991) proposed a method that dynamically computes C_S based on an algebraic identity between two different grid resolutions, i.e. a resolved grid level and a test-grid level. The grid spacing in the test-grid level is usually twice larger than that of the resolved grid level. The anisotropic part of the residual stresses is now described at two grid levels as follows:

$$\tau_{ij}^* - \frac{1}{3}\delta_{ij}\tau_{kk} = -2C_S\tilde{\Delta}^2\widetilde{|\hat{S}|\hat{S}_{ij}}, \quad (\text{A.5})$$

$$T_{ij}^* - \frac{1}{3}\delta_{ij}T_{kk} = -2C_S\tilde{\Delta}^2\widetilde{|\hat{S}|\hat{S}_{ij}}, \quad (\text{A.6})$$

where T_{ij}^* is the residual stress at the test-grid level, and $\tilde{\cdot}$ indicates the filtered parameter at the test grid-level. The Germano identity is defined based on the differences between Eq. A.5 and Eq. A.6 as follows:

$$\begin{aligned} \mathcal{L}_{ij} &= T_{ij}^* - \tau_{ij}^* = C_S M_{ij}, \\ M_{ij} &= -2(\tilde{\Delta}^2\widetilde{|\hat{S}|\hat{S}_{ij}} - \tilde{\Delta}^2\widetilde{|\hat{S}|\hat{S}_{ij}}). \end{aligned} \quad (\text{A.7})$$

By multiplying two sides of Eq. A.7 by \tilde{S}_{ij} , the Smagorinsky coefficient is described as

$$C_S = \frac{1}{2} \frac{\mathcal{L}_{ij}\tilde{S}_{ij}}{M_{ij}\tilde{S}_{ij}}. \quad (\text{A.8})$$

This dynamic model not only does exhibit an appropriate asymptotic behavior near the solid surfaces but accounts for the backscatter as well since C_S can take negative magnitudes. One drawback for the proposed method is the unclear physical meaning of Eq. A.8 when the denominator vanishes or becomes so small as to lead to an unstable coefficient C_S . Later, Lilly (1992) modified this model by applying a least squares approach and minimizing the errors. The square of error can be estimated by

$$Q = (\mathcal{L}_{ij} - 2C_S M_{ij})^2, \quad (\text{A.9})$$

and setting $\partial Q / \partial C_S = 0$ results in a modified correlation for the Smagorinsky coefficient,

$$C_S = \frac{1}{2} \frac{\mathcal{L}_{ij} M_{ij}}{M_{ij} M_{ij}}. \quad (\text{A.10})$$

In contrast to Eq. A.8, the denominator of Eq. A.10 vanishes only when each of the five independent components of M_{ij} becomes zero. However, the dynamic models are associated with a few drawbacks like the risk of numerical instability due to excessive backscatter or assuming equilibrium between production and dissipation of the SGS turbulence kinetic energy.

A.3 Dynamic Nonlinear Subgrid Scale Model

Wang and Bergstrom (2005) proposed a dynamic nonlinear model (DNM) based on an explicit nonlinear tensorial polynomial constitutive relation. The DNM is based on analogies with non-Newtonian fluids for closing the Reynolds stress model in the RANS turbulence modeling. There are eleven independent tensorial elements pertaining to the products of the rotation rate. However, only four components are implemented in the DNM to avoid the high computational cost and complexity of the algorithm. The DNM also improves the unrealistic effects of the SGS dissipation due to the restriction on the model coefficient to be positive. The dynamic nonlinear subgrid scale model estimates the residual stresses based on both the symmetric (strain rate) and asymmetric (rotation rate) parts of the filtered velocity gradient as follows:

$$\tau_{ij}^* = -C_S \beta_{ij} - C_W \gamma_{ij} - C_N \eta_{ij}, \quad (\text{A.11})$$

and the residual stress tensor at the test-grid level is

$$T_{ij}^* = -C_S \alpha_{ij} - C_W \lambda_{ij} - C_N \zeta_{ij}. \quad (\text{A.12})$$

The new tensor notations are defined as

$$\begin{aligned}
\beta_{ij} &= \widetilde{\Delta^2 |S| S_{ij}}, \\
\gamma_{ij} &= 4\widetilde{\Delta^2}(\widetilde{S}_{ik}\widetilde{\Omega}_{kj} - \widetilde{\Omega}_{ik}\widetilde{S}_{kj}), \\
\eta_{ij} &= 4\widetilde{\Delta^2}(\widetilde{S}_{ik}\widetilde{S}_{kj} - \frac{1}{3}\widetilde{S}_{mn}\widetilde{S}_{nm}\delta_{ij}), \\
\alpha_{ij} &= \widetilde{\widetilde{\Delta^2}|\widehat{S}|\widehat{S}_{ij}}, \\
\lambda_{ij} &= 4\widetilde{\widetilde{\Delta^2}}(\widetilde{\widetilde{S}}_{ik}\widetilde{\widetilde{\Omega}}_{kj} - \widetilde{\widetilde{\Omega}}_{ik}\widetilde{\widetilde{S}}_{kj}), \\
\zeta_{ij} &= 4\widetilde{\widetilde{\Delta^2}}(\widetilde{\widetilde{S}}_{ik}\widetilde{\widetilde{S}}_{kj} - \frac{1}{3}\widetilde{\widetilde{S}}_{mn}\widetilde{\widetilde{S}}_{nm}\delta_{ij}).
\end{aligned} \tag{A.13}$$

where Ω_{ij} represent the rotation rate with the correlation of $\Omega_{ij} = \frac{1}{2}(u_{i,j} - u_{j,i})$. Substituting Eqs. A.11 and A.12 into the Germano identity equation ($\mathcal{L}_{ij} = T_{ij}^* - \tau_{ij}^*$) and using the least squares approach developed by Lilly (1992), the coefficients C_S , C_W , and C_N are determined by solving the following matrix:

$$\begin{bmatrix} M_{ij}M_{ij} & M_{ij}W_{ij} & M_{ij}N_{ij} \\ W_{ij}M_{ij} & W_{ij}W_{ij} & W_{ij}N_{ij} \\ N_{ij}M_{ij} & N_{ij}W_{ij} & N_{ij}N_{ij} \end{bmatrix} \cdot \begin{bmatrix} C_S \\ C_W \\ C_N \end{bmatrix} = \begin{bmatrix} \mathcal{L}_{ij}M_{ij} \\ \mathcal{L}_{ij}W_{ij} \\ \mathcal{L}_{ij}N_{ij} \end{bmatrix}, \tag{A.14}$$

where $W_{ij} = \lambda_{ij} - \gamma_{ij}$ and $N_{ij} = \zeta_{ij} - \eta_{ij}$.

References

- Abe, H., H. Kawamura, S. Toh, and T. Itano (2007). Effects of the streamwise computational domain size on DNS of a turbulent channel flow at high Reynolds number. In *Advances in Turbulence XI - Proceedings of the 11th EUROMECH European Turbulence Conference*, Porto, Portugal, 25-28 Jun, pp. 233–235.
- Alves Portela, F. and N. D. Sandham (2020). A DNS/URANS approach for simulating rough-wall turbulent flows. *International Journal of Heat and Fluid Flow* 85, 1–6.
- Amano, R. S. (1984). Development of a turbulence near-wall model and its application to separated and reattached flows. *Numerical Heat Transfer, Part B: Fundamentals* 7(1), 59–75.
- Anderson, W. and C. Meneveau (2011). Dynamic roughness model for large-eddy simulation of turbulent flow over multiscale, fractal-like rough surfaces. *Journal of Fluid Mechanics* 679, 288–314.
- Araya, G., L. Castillo, C. Meneveau, and K. Jansen (2011). A dynamic multi-scale approach for turbulent inflow boundary conditions in spatially developing flows. *Journal of Fluid Mechanics* 670, 581–605.
- Aupoix, B. and P. R. Spalart (2003). Extensions of the Spalart – Allmaras turbulence model to account for wall roughness. *International Journal of Heat and Fluid Flow* 24, 454–462.
- Bae, H. J., A. Lozano-Durán, S. T. Bose, and P. Moin (2018). Dynamic slip wall model for large-eddy simulation. *Journal of Fluid Mechanics* 859, 400–432.
- Bagwell, T., R. Adrian, R. Moser, and J. Kim (1993). Improved approximation of wall shear stress boundary conditions for large eddy simulation. In *Near-wall turbulent flows; Proceedings of the International Conference, Tempe AZ, Netherlands, 15-17 Mar*, pp. 265–275.
- Balaras, E. and C. Benocci (1994). Subgrid scale models in finite difference simulations of complex wall bounded flows. In *AGARD, Application of Direct and Large Eddy Simulation to Transition and Turbulence (see N95-21061 06-34); International Organization*.
- Balaras, E., C. Benocci, and U. Piomelli (1996). Two-layer approximate boundary conditions for large-eddy simulations. *AIAA Journal* 34(6), 1111–1119.

- Batten, P., U. Goldberg, and S. Chakravarthy (2004). Interfacing statistical turbulence closures with large-eddy simulation. *AIAA Journal* 42(3), 485–492.
- Bazdidi-Tehrani, F., M. Kiamansouri, and M. Jadidi (2016). Inflow turbulence generation techniques for large eddy simulation of flow and dispersion around a model building in a turbulent atmospheric boundary layer. *Journal of Building Performance Simulation* 9(6), 680–698.
- Béchara, W., C. Bailly, P. Lafon, and S. M. Candel (1994). Stochastic approach to noise modeling for free turbulent flows. *AIAA Journal* 32(3), 455–463.
- Bohr, E. (2005). *Inflow generation technique for large eddy simulation of turbulent boundary*. PhD Thesis, Rensselaer Polytechnic Institute NY, US.
- Bose, S. T. and P. Moin (2014). A dynamic slip boundary condition for wall-modeled large-eddy simulation. *Physics of Fluids* 26(1), 015104.
- Bose, S. T. and G. I. Park (2018). Wall-modeled large-eddy simulation for complex turbulent flows. *Annual Review of Fluid Mechanics* 50, 535–561.
- Burattini, P., S. Leonardi, P. Orlandi, and R. A. Antonia (2008). Comparison between experiments and direct numerical simulations in a channel flow with roughness on one wall. *Journal of Fluid Mechanics* 600, 403–426.
- Busse, A. and N. D. Sandham (2012). Parametric forcing approach to rough-wall turbulent channel flow. *Journal of Fluid Mechanics* 712, 169–202.
- Cabot, W. (1995). Large-eddy simulations with wall models. Technical report, Center for Turbulence Research, Stanford CA, US.
- Cabot, W. H. and P. Moin (2000). Approximate wall boundary conditions in the large-eddy simulation of high Reynolds number flow. *Flow, Turbulence and Combustion* 63, 269–291.
- Cardillo, J., Y. Chen, G. Araya, J. Newman, K. Jansen, and L. Castillo (2013). DNS of a turbulent boundary layer with surface roughness. *Journal of Fluid Mechanics* 729, 603–637.
- Cebeci, T. and K. C. Chang (1978). Calculation of incompressible rough-wall boundary-layer flows. *AIAA Journal* 16(7), 740–746.
- Chaouat, B. (2017). The state of the art of hybrid RANS/LES modeling for the simulation of turbulent flows. *Flow, Turbulence and Combustion* 99(2), 279–327.
- Chapman, D. R. (1979). Computational aerodynamics development and outlook. *AIAA Journal* 17(12), 1293–1313.
- Chen, S., Z. Xia, S. Pei, J. Wang, Y. Yang, Z. Xiao, and Y. Shi (2012). Reynolds-stress-constrained large-eddy simulation of wall-bounded turbulent flows. *Journal of Fluid Mechanics* 703, 1–28.

- Chung, D. and D. I. Pullin (2009). Large-eddy simulation and wall modelling of turbulent channel flow. *Journal of Fluid Mechanics* 631, 281–309.
- Clauser, F. H. (1956). The turbulent boundary layer. *Advanced Applied Mechanics* 4, 1–51.
- Colebrook, C. F. (1939). Turbulent flow in pipes with particular reference to the transition region between the smooth- and rough-pipe laws. *Journal of the Institution of Civil Engineers* 11(4), 133–156.
- Coleman, H. W., B. K. Hodge, and R. P. Taylor (1984). A re-evaluation of Schlichting’s surface roughness experiment. *Journal of Fluids Engineering* 106(1), 60–65.
- Craft, T. J., S. E. Gant, H. Iacovides, and B. E. Launder (2004). A new wall function strategy for complex turbulent flows. *Numerical Heat Transfer, Part B: Fundamentals* 45(4), 301–318.
- Deardorff, J. W. (1970). A numerical study of three dimensional turbulent channel flow at large Reynolds numbers. *Journal of Fluid Mechanics* 41, 453–480.
- Degraaff, D. B. and J. K. Eaton (2000). Reynolds-number scaling of the flat-plate turbulent boundary layer. *Journal of Fluid Mechanics* 422, 319–346.
- Dhamankar, N. S., G. A. Blaisdell, and A. S. Lyrintzis (2018). Overview of turbulent inflow boundary conditions for large-eddy simulations. *AIAA Journal* 56(4), 1317–1334.
- Dirling, J. R. (1973). A method for computing roughwall heat transfer rates on reentry nosetips. In *AIAA 8th Thermodynamics Conference, Palm Springs CA, US, 16-18 Jul*, Number 73, pp. 1–9.
- Druault, P., S. Lardeau, J. P. Bonnet, F. Coiffet, J. Delville, E. Lamballais, J. F. Largeau, and L. Perret (2004). Generation of three-dimensional turbulent inlet conditions for large-eddy simulation. *AIAA Journal* 42(3), 447–456.
- Duprat, C., G. Balarac, O. Métais, P. M. Congedo, and O. Brugière (2011). A wall-layer model for large-eddy simulations of turbulent flows with/out pressure gradient. *Physics of Fluids* 23(1), 015101.
- Dutta, R., J. Nicolle, A. M. Giroux, and U. Piomelli (2017). Evaluation of turbulence models in rough- wall boundary layers for hydroelectric applications. *International Journal of Fluid Machinery and Systems* 10(3), 227–239.
- Fasel, H. F., U. Rist, and U. Konzelmann (1990). Numerical investigation of the three-dimensional development in boundary-layer transition. *AIAA Journal* 28(1), 29–37.
- Ferrante, A. and S. E. Elghobashi (2004). A robust method for generating inflow conditions for direct simulations of spatially-developing turbulent boundary layers. *Journal of Computational Physics* 198(1), 372–387.

- Forooghi, P., B. Frohnapfel, F. Magagnato, and A. Busse (2018). A modified parametric forcing approach for modelling of roughness. *International Journal of Heat and Fluid Flow* 71, 200–209.
- Frère, A., C. C. de Wiart, K. Hillewaert, P. Chatelain, and G. Winckelmans (2017). Application of wall-models to discontinuous Galerkin LES. *Physics of Fluids* 29(8), 085111.
- Germano, M., U. Piomelli, P. Moin, and W. H. Cabot (1991). A dynamic subgrid-scale eddy viscosity model. *Physics of Fluids A* 3(7), 1760–1765.
- Heinz, S. (2020). A review of hybrid RANS-LES methods for turbulent flows: Concepts and applications. *Progress in Aerospace Sciences* 114, 100597.
- Hellsten, A. and S. Laine (1997). Extension of the k-omega-SST turbulence model for flows over rough surfaces. In *22nd Atmospheric Flight Mechanics Conference*, New Orleans LA, US, 11-13 Aug, pp. 252–260.
- Hosseinzade, H. and D. J. Bergstrom (2021). Time-averaging and temporal-filtering in wall-modeled large eddy simulation. *Physics of Fluids* 33(3), 035108.
- Hoyas, S. and J. Jiménez (2006). Scaling of the velocity fluctuations in turbulent channels up to $Re = 2003$. *Physics of Fluids* 18, 011702.
- Iacovides, H. and B. E. Launder (1984). PSL—An economical approach to the numerical analysis of near-wall, elliptic flow. *Journal of Fluids Engineering* 106(2), 241–242.
- Inoue, M. and D. I. Pullin (2011). Large-eddy simulation of the zero-pressure-gradient turbulent boundary layer up to $Re = O(10^{12})$. *Journal of Fluid Mechanics* 686, 507–533.
- Jarrin, N., S. Benhamadouche, D. Laurence, and R. Prosser (2006). A synthetic-eddy-method for generating inflow conditions for large-eddy simulations. *International Journal of Heat and Fluid Flow* 27(4), 585–593.
- Jewkes, J. W., Y. M. Chung, and P. W. Carpenter (2011). Modification to a turbulent inflow generation method for boundary-layer flows. *AIAA Journal* 49(1), 247–250.
- Jimenez, J. (2004). Turbulent flows over rough walls. *Annual Review of Fluid Mechanics* 36(1991), 173–196.
- Johnson, D. A. and L. S. King (1985). A mathematically simple turbulence closure model for attached and separated turbulent boundary layers. *AIAA Journal* 23(11), 1684–1692.
- Kataoka, H. (2008). Numerical simulations of a wind-induced vibrating square cylinder within turbulent boundary layer. *Journal of Wind Engineering and Industrial Aerodynamics* 96(10-11), 1985–1997.
- Kawai, S. and J. Larsson (2012). Wall-modeling in large eddy simulation: Length scales, grid resolution, and accuracy. *Physics of Fluids* 24, 015105.

- Kawai, S. and J. Larsson (2013). Dynamic non-equilibrium wall-modeling for large eddy simulation at high Reynolds numbers. *Physics of Fluids* 25, 015105.
- Keating, A., U. Piomelli, E. Balaras, and H. J. Kaltenbach (2004). A priori and a posteriori tests of inflow conditions for large-eddy simulation. *Physics of Fluids* 16(12), 4696–4712.
- Kim, J. and P. Moin (1985). Application of a fractional-step method to incompressible Navier-Stokes equations. *Journal of Computational Physics* 59(2), 308–323.
- Klein, M., A. Sadiki, and J. Janicka (2003). A digital filter based generation of inflow data for spatially developing direct numerical or large eddy simulations. *Journal of Computational Physics* 186(2), 652–665.
- Krogstad, P. A. (1991). Modification of the van Driest damping function to include the effects of surface roughness. *AIAA Journal* 29, 888–894.
- Krogstad, P. A., H. I. Andersson, O. M. Bakken, and A. Ashrafian (2005). An experimental and numerical study of channel flow with rough walls. *Journal of Fluid Mechanics* 530, 327–352.
- Krumbein, B., P. Forooghi, S. Jakirlic, F. Magagnato, and B. Frohnepfel (2017). VLES modeling of flow over walls with variably-shaped roughness by reference to complementary DNS. *Flow, Turbulence and Combustion* 99, 685–703.
- Krumbein, B., S. Jakirlic, and C. Tropea (2019). A unified modeling approach for flow over porous and rough walls in scale-resolving simulation method. In *11th International Symposium on Turbulence and Shear Flow Phenomena (TSFP11)*, Southampton, UK, 30 Jul - 2 Aug, pp. 1–6.
- Kuwata, Y. and Y. Kawaguchi (2019). Direct numerical simulation of turbulence over resolved and modeled rough walls with irregularly distributed roughness. *International Journal of Heat and Fluid Flow* 77, 1–18.
- Larsson, J., S. Kawai, J. Bodart, and I. Bermejo-Moreno (2016). Large eddy simulation with modeled wall-stress: recent progress and future directions. *Mechanical Engineering Reviews* 3(15-00418), 1–23.
- Launder, B. E. and D. B. Spalding (1974). The numerical computation of turbulent flows. *Computer Methods in Applied Mechanics and Engineering* 3(2), 269–289.
- Le, H. (1995). *Direct numerical simulation of turbulent flow over a backward-facing step*. PhD Thesis, Stanford University, US.
- Le, H., P. Moin, and J. Kim (1997). Direct numerical simulation of turbulent flow over a backward-facing step. *Journal of Fluid Mechanics* 330, 349–374.
- Lee, J., M. Cho, and H. Choi (2013). Large eddy simulations of turbulent channel and boundary layer flows at high Reynolds number with mean wall shear stress boundary condition. *Physics of Fluids* 25(11), 110808.

- Lee, J., J. H. Lee, J. H. Lee, and H. J. Sung (2010). Coherent structures in turbulent boundary layers with adverse pressure gradients. *Journal of Turbulence* 11, 1–20.
- Lee, M. and R. D. Moser (2015). Direct numerical simulation of turbulent channel flow up to $Re = 5200$. *Journal of Fluid Mechanics* 774, 395–415.
- Lee, S., S. K. Lele, and P. Moin (1992). Simulation of spatially evolving turbulence and the applicability of Taylor’s hypothesis in compressible flow. *Physics of Fluids A* 4(7), 1521–1530.
- Leonard, A. (1975). Energy cascade in large-eddy simulations of turbulent fluid flows. *Advances in Geophysics* 18, 237–248.
- Li, N., E. Balaras, and U. Piomelli (2000). Inflow conditions for large-eddy simulations of mixing layers. *Physics of Fluids* 12(4), 935–938.
- Lilly, D. K. (1992). A proposed modification of the Germano subgrid-scale closure method. *Physics of Fluids A: Fluid Dynamics* 4(3), 633–635.
- Liu, K. and R. H. Pletcher (2006). Inflow conditions for the large eddy simulation of turbulent boundary layers: A dynamic recycling procedure. *Journal of Computational Physics* 219(1), 1–6.
- Lowery, P. S. (1987). *Numerical simulation of a spatially-developing, forced, plane mixing layer*. PhD Thesis, Stanford University, US.
- Lozano-Durán, A. and J. Jiménez (2014). Effect of the computational domain on direct simulations of turbulent channels up to $Re = 4200$. *Physics of Fluids* 26, 011702.
- Lund, T. S., X. Wu, and K. D. Squires (1998). Generation of turbulent inflow data for spatially-developing boundary layer simulations. *Journal of Computational Physics* 140, 233–258.
- Mani, A. (2012). Analysis and optimization of numerical sponge layers as a nonreflective boundary treatment. *Journal of Computational Physics* 231(2), 704–716.
- Marusic, I., B. J. McKeon, P. A. Monkewitz, H. M. Nagib, A. J. Smits, and K. R. Sreenivasan (2010). Wall-bounded turbulent flows at high Reynolds numbers: Recent advances and key issues. *Physics of Fluids* 22(6), 1–24.
- Mason, P. J. (1994). Large-eddy simulation: A critical review of the technique. *Quarterly Journal of the Royal Meteorological Society* 120(515), 1–26.
- Mathis, R., N. Hutchins, and I. Marusic (2009). Large-scale amplitude modulation of the small-scale structures in turbulent boundary layers. *Journal of Fluid Mechanics* 628, 311–337.
- Mathis, R., I. Marusic, S. I. Chernyshenko, and N. Hutchins (2013). Estimating wall-shear-stress fluctuations given an outer region input. *Journal of Fluid Mechanics* 715, 163–180.

- McMasters, J. H. and M. Henderson (1979). Low-speed single-element airfoil synthesis. *Technical Soaring* 6(2), 1–21.
- Meneveau, C., T. S. Lund, and W. H. Cabot (1996). A Lagrangian dynamic subgrid-scale model of turbulence. *Journal of Fluid Mechanics* 319, 353–385.
- Menter, F. R. and Y. Egorov (2005). A scale-adaptive simulation model using two-equation models. In *43rd AIAA Aerospace Sciences Meeting and Exhibit*, Reno NV, US, 10-13 Jan, pp. 271–283.
- Moin, P. and J. Kim (1982). Numerical investigation of turbulent channel flow. *Journal of Fluid Mechanics* 118, 341–377.
- Morgan, B., J. Larsson, S. Kawai, and S. K. Lele (2011). Improving low-frequency characteristics of recycling/rescaling inflow turbulence generation. *AIAA Journal* 49(3), 582–597.
- Moser, R. D., J. Kim, and N. N. Mansour (1999). Direct numerical simulation of turbulent channel flow up to $Re = 590$. *Journal of Fluid Mechanics* 11, 943–945.
- Munters, W., C. Meneveau, and J. Meyers (2016). Shifted periodic boundary conditions for simulations of wall-bounded turbulent flows. *Physics of Fluids* 28(2), 025112.
- Na, Y. (1996). *Direct numerical simulation of turbulent boundary layers with adverse pressure gradient and separation*. PhD Thesis, Stanford University, US.
- Nagib, H. M. and K. A. Chauhan (2008). Variations of von Kármán coefficient in canonical flows. *Physics of Fluids* 20(10), 101518.
- Nagib, H. M., K. A. Chauhan, and P. A. Monkewitz (2007). Approach to an asymptotic state for zero pressure gradient turbulent boundary layers. *Philosophical Transactions of the Royal Society A: Mathematical, Physical and Engineering Sciences* 365(1852), 755–770.
- Nakayama, A., H. Noda, and K. Maeda (2004). Similarity of instantaneous and filtered velocity fields in the near wall region of zero-pressure gradient boundary layer. *Fluid Dynamics Research* 35(4), 299–321.
- Neto, A. S., D. Grand, O. Métais, and M. Lesieur (1993). A numerical investigation of the coherent vortices in turbulence behind a backward-facing step. *Journal of Fluid Mechanics* 256, 1–25.
- Nicoud, F., J. S. Baggett, P. Moin, and W. Cabot (2001). Large eddy simulation wall-modelling based on suboptimal control theory and linear stochastic estimation. *Physics of Fluids* 13(10), 2968–2984.
- Nikitin, N. V., F. Nicoud, B. Wasistho, K. D. Squires, and P. R. Spalart (2000). An approach to wall modeling in large-eddy simulations. *Physics of Fluids* 12(7), 1629–1632.
- Nikuradse, J. (1950). Laws of flow in rough pipes. Technical report, NACA-TM-1292.

- Orlandi, P. and S. Leonardi (2008). Direct numerical simulation of three-dimensional turbulent rough channels: Parameterization and flow physics. *Journal of Fluid Mechanics* 606, 399–415.
- Österlund, J. M. (1999). *Experimental studies of zero pressure-gradient turbulent boundary layer flow*. PhD Thesis, Royal Institute of Technology, Sweden.
- Park, G. I. and P. Moin (2014). An improved dynamic non-equilibrium wall-model for large eddy simulation. *Physics of Fluids* 26, 015108.
- Pauley, L. L., P. Moin, and W. C. Reynolds (1990). The structure of two-dimensional separation. *Journal of Fluid Mechanics* 220, 397–411.
- Perret, L. and F. Kerhervé (2019). Identification of very large scale structures in the boundary layer over large roughness elements. *Experiments in Fluids* 60(97), 1–16.
- Piomelli, U. and E. Balaras (2002). Wall layer models for large eddy simulations. *Annual Review of Fluid Mechanics* 34, 349–374.
- Piomelli, U., J. Ferziger, P. Moin, and J. Kim (1989). New approximate boundary conditions for large eddy simulations of wall-bounded flows. *Physics of Fluids A* 1(6), 1061–1068.
- Piomelli, U. and J. Yuan (2013). Numerical simulations of spatially developing, accelerating boundary layers. *Physics of Fluids* 25(10), 101304.
- Pope, S. B. (2000). *Turbulent Flows*. Cambridge: Cambridge University Press.
- Prandtl, L. (1925). Bemerkungen über die entstehung der turbulenz. *Journal of Applied Mathematics and Mechanics* 1(6), 431–436.
- Rai, M. M. and P. Moin (1993). Direct numerical simulation of transition and turbulence in a spatially evolving boundary layer. *Journal of Computational Physics* 109(2), 169–192.
- Raupach, M. R., R. A. Antonia, and S. Rajagopalan (1991). Rough-wall turbulent boundary layers. *Applied Mechanics Reviews* 44(1), 1–25.
- Reynolds, O. (1883). An experimental investigation of the circumstances which determine whether the motion of water shall be direct or sinuous, and of the law of resistance in parallel channels. In *Proceedings of the Royal Society of London*, Volume 35, London, UK, 01 Jan, pp. 84–99.
- Rotta, J. C. (1962). Turbulent boundary layers in incompressible flow. *Progress in Aerospace Sciences* 2(1), 1–95.
- Sabau, A. S. and P. E. Raad (1999). Oscillations in high-order finite difference solutions of stiff problems on non-uniform grids. *International Journal for Numerical Methods in Fluids* 30(8), 939–956.
- Saito, N., D. I. Pullin, and M. Inoue (2012). Large eddy simulation of smooth-wall, transitional and fully rough-wall channel flow. *Physics of Fluids* 24(7), 075103.

- Sayadi, T., C. W. Hamman, and P. Moin (2013). Direct numerical simulation of complete H-type and K-type transitions with implications for the dynamics of turbulent boundary layers. *Journal of Fluid Mechanics* 724, 480–509.
- Schlatter, P., Q. Li, G. Brethouwer, A. V. Johansson, and D. S. Henningson (2010). Simulations of spatially evolving turbulent boundary layers up to $Re = 4300$. *International Journal of Heat and Fluid Flow* 31(3), 251–261.
- Schlatter, P., R. Örlü, Q. Li, G. Brethouwer, H. M. Fransson, V. A. Johansson, H. P. Alfredsson, and S. D. Henningson (2009). Turbulent boundary layers up to $Re = 2500$ studied through simulation and experiment. *Physics of Fluids* 21(5), 051702.
- Schlichting, H. (1936). Experimentelle Untersuchungen zum Rauigkeitsproblem. *Ingenieur-Archiv* 7(1), 1–34.
- Schlichting, H. and K. Gersten (2017). *Boundary-Layer Theory* (Ninth ed.). Berlin Heidelberg: Springer-Verlag.
- Schlüter, J. U., H. Pitsch, and P. Moin (2004). Large eddy simulation inflow conditions for coupling with Reynolds-averaged flow solvers. *AIAA Journal* 42(3), 478–484.
- Schultz, M. P. and K. A. Flack (2007). The rough-wall turbulent boundary layer from the hydraulically smooth to the fully rough regime. *Journal of Fluid Mechanics* 580, 381–405.
- Schumann, U. (1975). Subgrid scale model for finite difference simulations of turbulent flows in plane channels and annuli. *Journal of Computational Physics* 18(4), 376–404.
- Scotti, A. (2010). Direct numerical simulation of turbulent channel flows with boundary roughened with virtual sandpaper. *Physics of Fluids* 18(3), 031701.
- Shur, M. L., P. R. Spalart, M. K. Strelets, and A. K. Travin (2008). A hybrid RANS-LES approach with delayed-DES and wall-modelled LES capabilities. *International Journal of Heat and Fluid Flow* 29(6), 1638–1649.
- Smagorinsky, J. (1963). General circulation experiments with the primitive equations: I. The basic experiment. *Monthly Weather Review* 91(3), 99–164.
- Souverein, L. J., P. Dupont, J. F. Debiève, J. P. Dussauge, B. W. Van Oudheusden, and F. Scarano (2010). Effect of interaction strength on unsteadiness in turbulent shock-wave-induced separations. *AIAA Journal* 48(7), 1480–1493.
- Spalart, P. R. (1988). Direct simulation of a turbulent boundary layer up to $Re = 1410$. *Journal of Fluid Mechanics* 187, 61–98.
- Spalart, P. R. (2000). Trends in turbulence treatments. In *AIAA, Fluids 2000 Conference and Exhibit*, Denver, CO, 19–22 Jun, pp. 2000–2306.
- Spalart, P. R. and A. Leonard (1987). Direct numerical simulation of equilibrium turbulent boundary layers. In *International Symposium on Turbulent Shear Flows - Turbulent Shear Flows 5*, Ithaca NY, US, 7–9 Aug, pp. 234–252.

- Spalding, D. B. (1961). A single formula for the “law of the wall”. *Journal of Applied Mechanics* 28(3), 455.
- Speziale, C. G. (1998). Turbulence modeling for time-dependent RANS and VLES: A review. *AIAA Journal* 36(2), 173–184.
- Squire, D. T., C. Morrill-Winter, N. Hutchins, M. P. Schultz, J. C. Klewicki, and I. Marusic (2016). Comparison of turbulent boundary layers over smooth and rough surfaces up to high Reynolds numbers. *Journal of Fluid Mechanics* 795, 210–240.
- Stüben, K. and U. Trottenberg (1982). *Multigrid methods: Fundamental Algorithms, Model Problem, Analysis and Applications*. Berlin, Heidelberg: Springer Berlin Heidelberg.
- Suga, K., T. J. Craft, and H. Iacovides (2006). An analytical wall-function for turbulent flows and heat transfer over rough walls. *International Journal of Heat and Fluid Flow* 27(5), 852–866.
- Suga, K., T. Sakamoto, and Y. Kuwata (2019). Algebraic non-equilibrium wall-stress modeling for large eddy simulation based on analytical integration of the thin boundary-layer equation. *Physics of Fluids* 31(7), 075109.
- Sussman, M., A. S. Almgren, J. B. Bell, P. Colella, L. H. Howell, and M. L. Welcome (1999). An adaptive level set approach for incompressible two-phase flows. *Journal of Computational Physics* 148(1), 81–124.
- Tabor, G. R. and M. H. Baba-Ahmadi (2010). Inlet conditions for large eddy simulation: A review. *Computers & Fluids* 39(4), 553–567.
- Tani, I. (1988). Drag reduction by riblet viewed as roughness problem. *Proceedings of the Japan Academy. Series B. Physical and Biological Sciences* 64(2), 21–24.
- Taylor, R. P., B. K. Hodge, and H. W. Coleman (1985). Prediction of turbulent skin friction for two-dimensional, rib-type surface roughness using a discrete element approach. *Journal of Fluids Engineering* 107, 251–257.
- Tunstall, R., D. Laurence, R. Prosser, and A. Skillen (2017). Towards a generalised dual-mesh hybrid LES/RANS framework with improved consistency. *Computers and Fluids* 157, 73–83.
- Urbin, G. and D. Knight (2001). Large-eddy simulation of a supersonic boundary layer using an unstructured grid. *AIAA Journal* 39(7), 1288–1295.
- Vafai, K. and S. J. Kim (1995). On the limitations of the Brinkman-Forchheimer-extended Darcy equation. *International Journal of Heat and Fluid Flow* 16(1), 11–15.
- Vallikivi, M., M. Hultmark, and A. J. Smits (2015). Turbulent boundary layer statistics at very high Reynolds number. *Journal of Fluid Mechanics* 779, 371–389.
- Wang, B. C. and D. J. Bergstrom (2005). A dynamic nonlinear subgrid-scale stress model. *Physics of Fluids* 17(035109), 1–15.

- Wang, M. and P. Moin (2002). Dynamic wall modeling for large-eddy simulation of complex turbulent flows. *Physics of Fluids* 14(7), 2043–2051.
- Whitaker, S. (1996). The Forchheimer equation: A theoretical development. *Transport in Porous Media* 25(1), 27–61.
- White, F. M. (2003). *Fluid Mechanics* (5th ed.). Boston: McGraw-Hill.
- White, F. M. (2006). *Viscous Fluid Flow* (3rd ed.). New York: McGraw-Hill.
- Wu, X. (2017). Inflow turbulence generation methods. *Annual Review of Fluid Mechanics* 49, 23–49.
- Wu, X. and P. Moin (2009). Direct numerical simulation of turbulence in a nominally zero-pressure-gradient flat-plate boundary layer. *Journal of Fluid Mechanics* 630, 5–41.
- Wu, X., K. D. Squires, and T. S. Lund (1995). Large eddy simulation of a spatially-developing boundary layer. In *Proceedings of the ACM/IEEE Supercomputing Conference*, Volume 2, New York NY, US, 4-8 Dec, pp. 1838–1857. IEEE.
- Xiao, H. and P. Jenny (2012). A consistent dual-mesh framework for hybrid LES/RANS modeling. *Journal of Computational Physics* 231(4), 1848–1865.
- Xiao, H., J.-X. Wang, and P. Jenny (2017). An implicitly consistent formulation of a dual-mesh hybrid LES/RANS method. *Communications in Computational Physics* 21(2), 570–599.
- Xu, H. H. and X. I. Yang (2021). Treatment of unphysical numerical oscillations via local grid refinement. *Center for Turbulence Research, Annual Research Briefs* 33(7), 077104.
- Yang, X. I. and C. Meneveau (2016). Recycling inflow method for simulations of spatially evolving turbulent boundary layers over rough surfaces. *Journal of Turbulence* 17(1), 75–93.
- Yang, X. I., G. I. Park, and P. Moin (2017). Log-layer mismatch and modeling of the fluctuating wall stress in wall-modeled large-eddy simulations. *Physical Review Fluids* 2(10), 1–13.
- Yang, X. I. A., J. Sadique, R. Mittal, and C. Meneveau (2015). Integral wall model for large eddy simulations of wall-bounded turbulent flows. *Physics of Fluids* 27(2), 025112.
- Yin, J. (2008). *Large Eddy Simulation of Mixed Convection in a Vertical Slot and Geometrical Statistics of Wall-bounded Thermal flow*. PhD Thesis, University of Saskatchewan, Canada.
- Zagarola, M., C. Incorporated, and A. Smits (1998). A new mean velocity scaling for turbulent boundary layers. In *Proceedings of FEDSM’98*, Washington, DC, US, 21-25 Jun, pp. 4950.
- Zhang, H., M. Faghri, and F. M. White (1996). A new low-Reynolds-number k-epsilon model for turbulent flow over smooth and rough surfaces. *Journal of Fluids Engineering, Transactions of the ASME* 118(2), 255–259.